Ministry of Higher Education
and Scientific Research

University of Babylon

College of Science

Department of Chemistry

Surface-modified ferric oxide nanoparticles and their applications for the removal fluorescein dye and antifungal activity

A Thesis

Submitted to the Council of the College of Science, University of Babylon in Partial Fulfillment of the Requirements for the Degree of Master of Science in Chemistry

By

Hussein Sayer Obaid Marwin

B.Sc. Babylon University 2019

Supervisor by

Asst. prof. Dr. Ahmed Fawzi Halbus

2023 A.D **1444 A.H**

جمهورية العراق

وزارة التعليم العالي والبحث العلمي

جامعة بابل – كلية العلوم

قسم الكيمياء

سطح - جسيمات أوكسيد الحديد النانوية المعدلة وتطبيقاتها لإزالة صبغة الفلورسين والنشاط المضاد للفطريات

رساله مقدمة

الى مجلس كلية العلوم / جامعة بابل

كجزء من متطلبات نيل درجة الماجستير في العلوم/ الكيمياء

من قبل

حسين ساير عبيد مروان

بكالوريوس علوم الكيمياء – جامعة بابل 2019

بإشراف

أ.م.د. احمد فوزي حلبوص المعموري

1444 هـ 2023 م

بسم الله الرحمن الرحيم

اللَّهُ لَا إِلَٰهَ إِلَّا هُوَ الْحَيُّ الْقَيُّومُ لَا تَأْخُذُهُ سِنَةٌ وَلَا نَوْمٌ لَّهُ مَا
فِي السَّمَاوَاتِ وَمَا فِي الْأَرْضِ مَن ذَا الَّذِي يَشْفَعُ عِندَهُ إِلَّا
بِإِذْنِهِ يَعْلَمُ مَا بَيْنَ أَيْدِيهِمْ وَمَا خَلْفَهُمْ وَلَا يُحِيطُونَ بِشَيْءٍ
مِّنْ عِلْمِهِ إِلَّا بِمَا شَاءَ وَسِعَ كُرْسِيُّهُ السَّمَاوَاتِ وَالْأَرْضَ
وَلَا يَئُودُهُ حِفْظُهُمَا وَهُوَ الْعَلِيُّ الْعَظِيمُ ۞

صدق الله العلي العظيم

الآية (٢٥٥) من سورة البقرة

Acknowledgment

In the Name of “**Allah**”, the Most Beneficent, the Most Merciful. All praise be to Allah, Lord of the Worlds, and the prayers, peace and blessings be upon the most noble of Prophets and Messengers, our Prophet Muhammad and AL-Muhammad.

First and foremost, Unlimited thanks to “**Allah**” the almighty, who learned us unless we know and who helped us from the beginning till this day. I am totally sure that this work would have never become truth, without his guidance.

I would like to present my sincere thanks and gratitude to my supervisor ***Asst. Prof. Dr.*** **Ahmed Fawzi Halbus** for proposing the research subject and for their continuou supervision, encouragement, farsighted interest, valuable advices and skillful guidance while directing research work.

It gives me a great pleasure to express a special appreciation to ***Asst. Prof. Dr.*** **Zahraa H. Athab**, I am extremely thankful to her enormous help me, encouragement and for his useful helpful, guidance and advices.

I owe a deep feeling and gratitude to my family to my **father**, **mother** and **brothers** for their continuous support. I thank them from the bottom of my heart. All thanks to my brother and friend **Hossam Adel,** for his continuous support to me. Finally, my thanks go to my colleague **Hussein Turki**.

Hussein 2023

الخلاصة

في هذا العمل تم دراسة عوامل وآليات الامتزاز ونشاط التحفيز الضوئي لجسيمات الحديد النانوية وجيسمات الحديد النانوية المغلفة ببولي (الصوديوم ٤- ستايرين سولفونات ملح الصوديوم) PSS (وبولي الاليلامين هيدروكلورايد) PAH والاتي تم تحضيرهما باستخدام تقنية الطبقات المتعددة. تم تصنيع جسيمات اوكسيد الحديد النانوية باستخدام طريقة الترسيب عند درجتي حرارة ٢٠٠ درجة مئوية و ٥٠٠ درجة مئوية. تمت دراسة نشاط جسيمات اوكسيد الحديد النانوية وجسيمات اوكسيد الحديد النانوية المعدلة بالتغليف تجاه صبغة الفلورسين FSS باستخدام التكسير الضوئي تحت الاشعة فوق البنفسجية و مقارنتها بالنتائج التي تم الحصول عليها في الظروف المظلمة وذلك لتقييم تأثير أنواع الأكسجين التفاعلية ROS. وضحت جسيمات اوكسيد الحديد النانوية وجسيمات اوكسيد الحديد النانوية المعدلة امتزازا ونشاط تكسير ضوئي ممتازا لصبغة الفلورسين FSS. وجد ان ايزوثيرم الامتزاز (لانكماير) وحركية التفاعل من الدرجة الثانية الكاذبة مطابقة مع خصائص الامتزاز لجسيمات اوكسيد الحديد النانوية. اظهرت جسيمات الحديد النانوية المغلفة مع بولمر PSS ذات الشحنة السالبة امتزازا ونشاط تكسير ضوئي اقل بكثير عند مقارنته بجسيمات اوكسيد الحديد النانوية المغلفة ببولمر PAH ذات الشحنة الموجبة وجسيمات اوكسيد الحديد النانوية الغير مغلفة. من هذا نستنتج أن تأثير تغليف السطح لجسيمات اوكسيد الحديد النانوية أقوى بكثير من تاثير أنواع الأكسجين التفاعلية ROS بسبب التشعيع بضوء الأشعة فوق البنفسجية. يشير هذا إلى أن ارتباط الجسيمات النانوية بصبغة الفلورسين FSS أكثر اهمية لامتزازها وعمل التكسير الضوئي من توليد (ROS). يمكن تفسير ذلك من خلال ضعف التصاق جسيمات اوكسيد الحديد النانوية المغلفة ببولمر PSS مع صبغة الفلورسين بسبب التنافر الكهروستاتيكي . في المقابل أدى التجاذب الكهروستاتيكي بصبغه الفلورسين FSS في حالة جسيمات الحديد النانوية الغير مغلفة وجسيمات اوكسيد الحديد النانوية المغلفة مع PAH ذات الشحنة الموجبة الى تحسين الامتزاز والتكسير الضوئي. بالإضافة الى ذألك، تم اكتشاف أن جسيمات اوكسيد الحديد النانوية الحرة الغير مغلفة والمغلفة مع PAH تمتلك انتقائية امتزاز عالية تجاه صبغة الفلورسين الانيونية وامتزاز قليل او معدوم تجاه الصبغات الكتيونية مثل صبغة الكرستال البنفسجي مما يجعل من السهل فصل الصبغتين عن المحاليل المائية الحاوية على مزيج الصبغتين.

و تعرض البيانات ايضًا أن جسيمات اوكسيد الحديد النانوية الحرة والمعدلة على السطح لها قابلية جيدة لإعادة التدوير مما يدل على أنها ستكون مادة اقتصادية وصديقة للبيئة وذات كفاءة كبيرة في معالجة المياه. تهدف هذه الدراسة ايضًا إلى تقيم فعالية جسيمات اوكسيد الحديد النانوية الحرة والمغلفة ببولي (الاليلامين

هيدروكلورايد) وبولي (الصوديوم ٤-ستايرين سولفونات ملح الصوديوم) كعوامل مضادة للفطريات. تمت دراسة التأثير المضاد للفطريات لجسيمات اوكسيد الحديد النانوية المغلفة مع PSS و PAH ضد فطر (الترايكودرما). تم التحقيق في تأثير تغليف سطح جسيمات اوكسيد الحديد النانوية ببولمر PAH بطريقة متعددة الطبقات عن طريق قياس نمو مستعمرات الفطريات مع الوقت. قدم جسيمات اوكسيد الحديد النانوية المغلفة ببولمر PAH نشاطًا مضادًا للفطريات ملحوظا مقارنة بعينة الفطر لجسيمات اوكسيد الحديد النانوية الغير مغلفة وجسيمات اوكسيد الحديد النانوية المغلفة ببولمر PSS تحت نفس الظروف والفترة الزمنية. يمكن تفسير ذلك من خلال الالتصاق الضعيف لجسيمات اوكسيد الحديد النانوية المغلفة ببولمر PSS مع فطر (ترايكودرما) بسبب التنافر الكهروستاتيكي. في المقابل أدى التجاذب الكهروستاتيكي بفطر (الترايكودرما) في حالة جسيمات اوكسيد الحديد النانوية المغلفة ببولمر PAH واوكسيد الحديد النانوي الحر الى تعزيز النشاط المضاد للفطريات. هذه النتائج قد تؤدي إلى تطور علاجات مضادة للفطريات أكثر كفاءة بجرعات أقل لمكافحة الفطريات مع فوائد اقتصادية وبيئية كبيرة.

Table of Contents

List of Tables

List of Figures

Directory of Abbreviations

Symbol	Description
NPs	nanoparticles
BET	Brauner Emeet Teller
C	Concentration
MRI	magnetic resonance imaging
cm	Centimeter
IONPs	Iron oxide nanoparticles
CVD	Chemical vapour deposition
°C	Centigrade
Eq	Equation
T%	Tassla
Abs	Absorbance
g	Gram
LBL	layer-by-layer
PAA	Poly(acrylic acid
K	Kelvin
k_{app}	The apparent first order rate constant
m	Meter
M	Molar
PDE	photodegradation efficiency
C mg L^{-1}	Concentration Par Milligram Liter
min	Minute
mL	Milliliter
mW	Milliwatt
nm	Nanometer
CV	crystal violet
R^2	Correlation coefficient
SEM	Scanning electron microscopy

Uv-vis	Ultra violet-visible
W	Watt
DLS	dynamic light scattering
λ	Wavelength
PSS	poly(sodium 4-styrenesulfonate) sodium salt
PAH	Poly allylamine hydrochloride
ROS	reactive oxygen species
FSS	fluorescein sodium salt
FTIR	Fourier Transform Infrared
EDX	Energy dispersive X-ray
h	hour
TEM	Transmission Electron Microscopy
BET	Brauner Emeet Teller
XRD	X-ray diffraction
PDADMAC	poly(diallyldimethyl ammonium chloride
D.W	Distal water

Summary

In this work, the factors and mechanisms of the adsorption and photocatalytic activity of iron oxide nanoparticles (Fe_2O_3NPs) coated with poly(sodium 4-styrenesulfonate) sodium salt (PSS), and poly(allylamine hydrochloride) (PAH) polyelectrolytes were explored using the layer by-layer technique. Fe_2O_3NPs was synthesized using the precipitation method at two calcination temperatures 200 °C and 500 °C. The activity of bare and surface modified Fe_2O_3NPs was studied toward fluorescein sodium salt (FSS) dye upon illumination with UV light compared with that under dark conditions to assess the effect of the oxidative stress because of the reactive oxygen species (ROS). The bare and surface modified Fe_2O_3NPs display excellent adsorption and photocatalytic activity for FSS dye. The Langmuir isotherm and the pseudo-second order kinetic model fit well with the adsorption properties of the Fe_2O_3NPs. The nanoparticles of the anionic surface (Fe_2O_3NPs/PSS) showed much lower adsorption and photocatalytic activity than the ones with a cationic surface functionality (Fe_2O_3NPs/PSS/PAH and bare Fe_2O_3NPs). The impact of the Fe_2O_3NPs surface coating was discovered to be much stronger than the ROS impact because of irradiation with UV light. This indicates that the nanoparticles attachment to the FSS dye is much more important for their adsorption and photocatalytic action than the ROS generation alone. This could be explained by the poor adhesion of Fe_2O_3NPs/PSS to the FSS dye due to electrostatic repulsion. In contrast, the particle−FSS dye electrostatic adhesion in the case of cationic Fe_2O_3NPs/PSS/PAH and bare Fe_2O_3NPs led to enhanced adsorption and photocatalytic action. Additionally, it was discovered that the Fe_2O_3NPs/PSS/PAH and bare Fe_2O_3NPs were extremely selective for anionic FSS over cationic crystal violet (CV) dye, making it simple to separate the two dyes from aqueous solutions of dye mixtures. The data also displays that bare and surface modified Fe_2O_3NPs have good recyclability, showing that they would be an economical material with significant potential in water treatment. This study also aims to assess the efficacy of

PSS and PAH-modified Fe_2O_3NPs as antifungal agents. The antifungal action of the PAH-functionalized Fe_2O_3NPs against *Trichoderma* fungus was studied. The effect of these PAH-surface functionalized Fe_2O_3NPs was investigated by measuring the growth of the fungus colonies versus time. The PAH-functionalized Fe_2O_3NPs presented significant antifungal activity, compared to the untreated fungus sample, bare Fe_2O_3NPs and Fe_2O_3NPs/PSS at the same conditions and period of time. This could be explained by the poor adhesion of Fe_2O_3NPs/PSS to the *Trichoderma* fungus due to electrostatic repulsion. In contrast, the particle−*Trichoderma* fungus electrostatic adhesion in the case of cationic Fe_2O_3NPs/PSS/PAH and bare Fe_2O_3NPs led to enhanced antifungal activity. These findings might result in the development of more efficient antifungal treatments at lower doses of active agents for fungus control with potentially substantial economic and environmental benefits.

1. General Introduction

1.1Nanotechnology

Nanotechnology has applications in every area of human life and it is a cutting-edge, state-of-the-art technology. Numerous techniques have been developed to produce nanoparticles as a result of scientists' focus on this subject [1–7]. People's daily lives have been impacted by the necessity to find new solutions to the issues that environmental technology is currently facing [8–12]. Nanotechnology is the science of physics that studies materials at nanoscale dimensions; the prefix nano is a Greek term that signifies dwarf. Nanotechnology is the study of nanoscale material synthesis, characterization, and applications. Nanomaterial are substances with a nanostructure, at least one dimension (1-100 nm in length, width, or thickness), Unique chemical and physical properties that make them superior to bulk substances [13]. Following notions presented by Richard Feynman in 1959, The late Norio Taniguchi used nanotechnology for the first time in 1974 [14]. Nanomaterial composition and real properties, such as their melting point, color, charge limit, and attractivity, can differ from those of mass materials with a comparable configuration [15]. Fortunately, a revolution in nanotechnology is taking place thanks to the time and effort being put forth by researchers from all over the world. These researchers are developing materials and devices with unique electronic, mechanical, optical, or magnetic properties that are not found in naturally occurring materials at the nanometer length scale. Interestingly, although having the same composition in both cases, attributes of materials at the nanoscale length scale are discovered to differ from those at the micrometer length scale [15]. A water problem is being caused by the industry's current production of a lot of different forms of wastewater that contain dangerous chemicals [16–21]. Due to urbanization and industrialization, the world's ground water has become a severe issue. The wastewater must be treated before being released into the environment in order to avoid water pollution [1, 22–26]. Numerous model organisms have experienced genotoxic and mutagenic effects as a result of dye exposure [1, 27–29]. To remove dyes from wastewater, a variety of techniques are used, including filtration, precipitation, adsorption, photodegradation, and chemical degradation [1, 30–34]. The dye compounds are classified as irritants and have adverse effects on humans, including respiratory distress, lacrimation, skin irritation, and carcinogenic consequences. The majority of synthetic dyes provide significant health risks to living systems by altering the chemical and physical properties of soil, the aquatic environment, and the flora and fauna. This causes the natural environment to collapse [9, 35–40].

Finding a new solution to the problems that are now being encountered in the field of environmental technology has had an effect on people's daily lives [9, 10]. Due to their unique properties such as thermal, catalytic, mechanical, optical, and magnetic, scientific research on metal nanoparticles has become enticing [41–45]. These distinctive characteristics are the fallout of a high surface area to volume ratio, and high surface energy contrived through nanoparticles. Metal nanoparticles are widely used in a variety of fields, including optics, electronics, material science, and the biological and medical sciences [9, 46, 47]. It is anticipated that developments in neuronal nanotechnology will have a substantial impact on the creation of novel therapeutical strategies. a wide range of applications in the biomedical field have been made possible by the ability to produce nanoparticles that are in the same size range as proteins. These particles can stimulate, react with, and affect target cells and tissues to ensure the desired physiological reactions while reducing undesirable outcomes [48] .

Table 1-1 Description of different nanostructures materials.

Nanostructure	Size	Material
Clusters and quantum dots	Radius, 1-10 nm	Metals, magnetic materials, semi-conductors, and insulators
Nanowires	Diameter, 1-10 nm	Metals, semiconductor Oxides, sulfides, nitrides, Carbon

Moreover nanotechnology has achieved the status as one of the critical research endeavors of the early 21st century, as scientists harness the unique properties of atomic and molecular assemblages built at the nanometer scale. Researchers can rationally design and use nanoparticles for drug delivery as image contrast agents, and for diagnostic purposes thanks to our capacity to modify the physical, chemical, and biological properties of these particles [49]. Nanotechnology provides significant potential advantages in a variety of fields. Through the development of new solutions to resolving environmental issues, nanomaterials have the potential to enhance the environment. A new technology called nanotechnology has been hailed as having the potential to overcome the chemical and physical limits of materials comprised of microparticles [50].

1.2 Nanoparticles

The production of nanoscale nanotechnology that can be generated via many ways, such as physical or chemical approaches, has drawn significant interest in many areas of research during the past two decades [51]. The fastest-growing area of nanotechnology is (NPs). These materials are outstanding and indispensable in many fields of human endeavors because of their unique size-dependent characteristics [52].

The crucial factor is the development of novel important physical, chemical, and biological properties in nanoscale built materials, such as nanoparticles, nanotubes, nanowires, ultrathin films, and nanocomposites. For a variety of biological applications, nanoparticles with a high surface to volume ratio can be functionalized with various ligands, coatings, and other helpful tools [53]. Ever since its discovery in the early 1970s, the chemical, physical, and mechanical properties of (NPs) have sparked substantial research. Due to its many potential applications across a wide range of fields, nano science has emerged as one of modern science and technology's most exciting and promising subjects [54]. In the nanoscale, nanoparticles are anano-objects with three dimensions. Because of the proportion of atoms in their height, nanomaterials have a high surface area to volume ratio. In order to interact with free atoms, molecules, and ions, additional active atoms must be accessible [55,56].

In order to increase the Fe_2O_3NPs' acceptance in related environmental issues, it is necessary to investigate other additional properties of the material, such as antibacterial activity and safety.

To assure material safety when exposed to the environment, the in vitro antibacterial activity and cytotoxicity of synthetic Fe_2O_3NPs are also investigated in this submission [9]. Nanoparticle research has become attractive due to its distinctive qualities, such as its ability to be thermal, catalytic, mechanical, optical, and magnetic [41–45]. These unique properties are a result of nanoparticles' high surface area to volume ratio and high surface energy. Nanoparticles are commonly used in a range of areas, such as electronics, material science, optics, and the biological and medical sciences as shown in (Figure 1.1) [9, 46, 47].

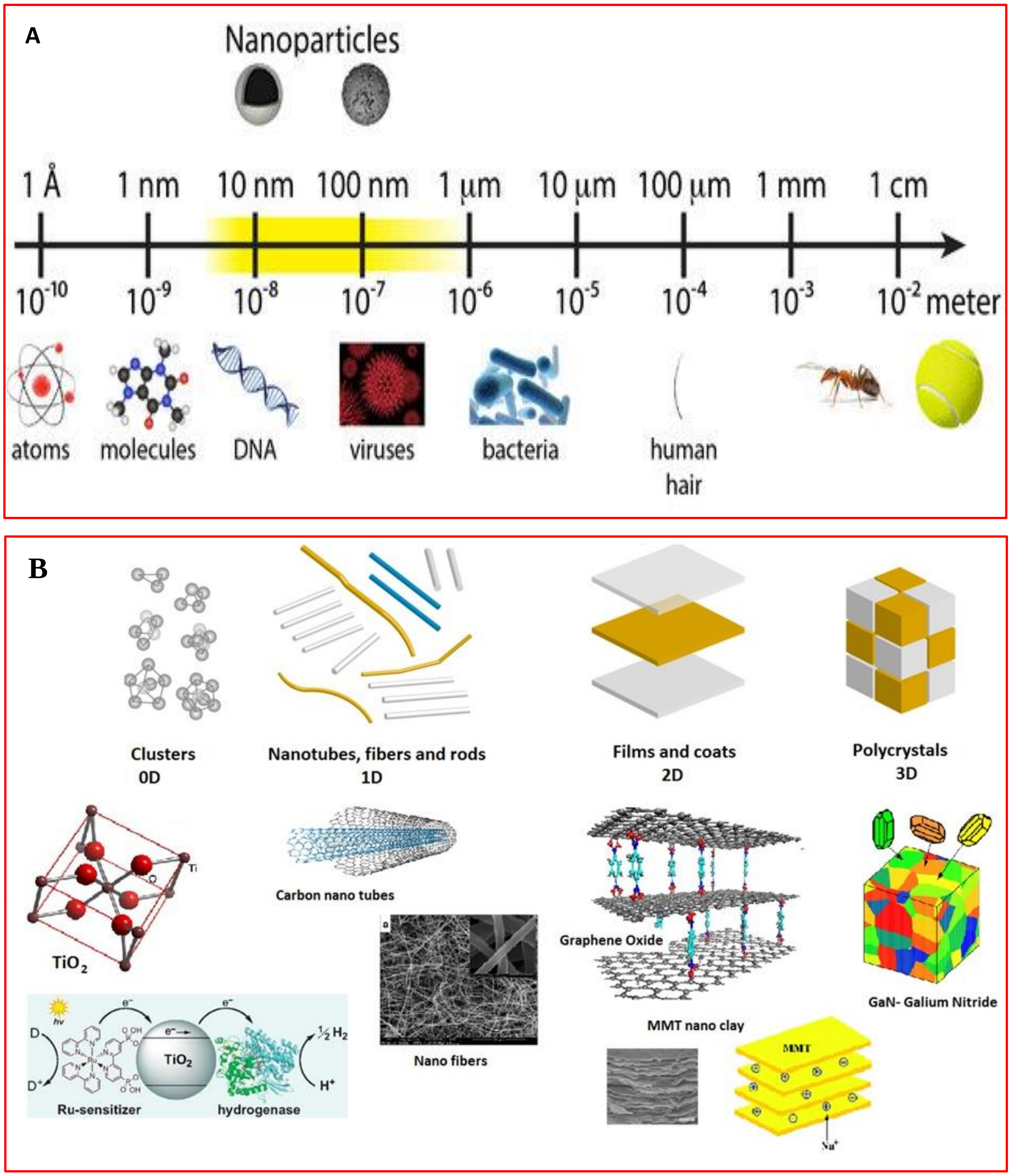

Figure 1.1 A,B. Dimensions of nanomaterials[57]

1.3 Iron Oxide NPs (Fe_2O_3NPs)

Iron oxide nanoparticle fabrication is being developed widely for both its vital applications in a variety of disciplines as well as its fundamental scientific interest. The development of iron oxide-based nanomaterial with distinctive features and functionality is currently being researched in great detail due to their magnetic properties, small size, and high surface area [58, 59]. There are several research, industrial, and medical applications for iron oxide nanoparticles [60, 61]. The surface modification of iron oxide nanoparticles utilizing various functionalization techniques is an important step in connection with the kind of application [62]. Iron oxide nanoparticles are getting more and more interest in the field of drug delivery and magnetic resonance imaging (MRI) because of their unique superparamagnetic properties, flexibility, low-cytotoxicity, and biocompatibility [59, 63–65]. Iron oxide nanoparticle production is being developed extensively for both its vital applications in a variety of disciplines as well as its fundamental scientific interest. Due to their magnetic properties, high surface area, and small size, the usage of iron oxide-based nanomaterial with unique properties and functionality is now being explored extensively [58, 59]. Iron oxide-based magnetic nanoparticles are used in a number of scientific, industrial, and medicinal fields [60, 61]. Nevertheless, an essential step in conjunction with such applications is the surface modification of Iron oxide nanoparticles using various functionalization techniques [62].
In nature, iron oxide is a mineral component that is widely distributed. It presents more of crystal forms in addition to different structural and magnetic properties [66]. . The close-packed planes of oxygen anions with iron cations in octahedral or tetrahedral interstitial sites can be used to describe the crystal structure of the three oxides [51].

Iron oxide nanoparticles have an iron oxide core and which is surrounded by a shell of ligands . Although more than ten iron oxides, hydroxides, and oxidohydroxides have been identified, the majority of IONPs include either magnetite (Fe_3O_4) or maghemite (-Fe_2O_3)

in their cores. Magnetic IONPs have attracted significant interest and have a wide range of technical, biological, and therapeutic uses because of the magnetism of these iron oxide modifications. However, zero-valent iron NPs as well as hematite (-Fe_2O_3) have been reported [67]. Generally speaking, iron oxides are pervasive, frequently utilized due to their low cost, and play a crucial part in numerous biological and geological processes. They are also widely used by people, such as hemoglobin, coatings, paints, and lasting pigments (such as those used in colored concrete and thermite) [68]. Magnetite (Fe_3O_4), maghemite (-Fe_2O_3), and hematite (-Fe_2O_3) are the three most prevalent types of iron oxides in nature. This evaluation will focus on these oxides because they are crucial in the realm of scientific technology .To ensure their reactivity and mobility, nanomaterials should typically be stable to prevent aggregation and have a low deposition rate as shown in (Figure 1.2) [50].

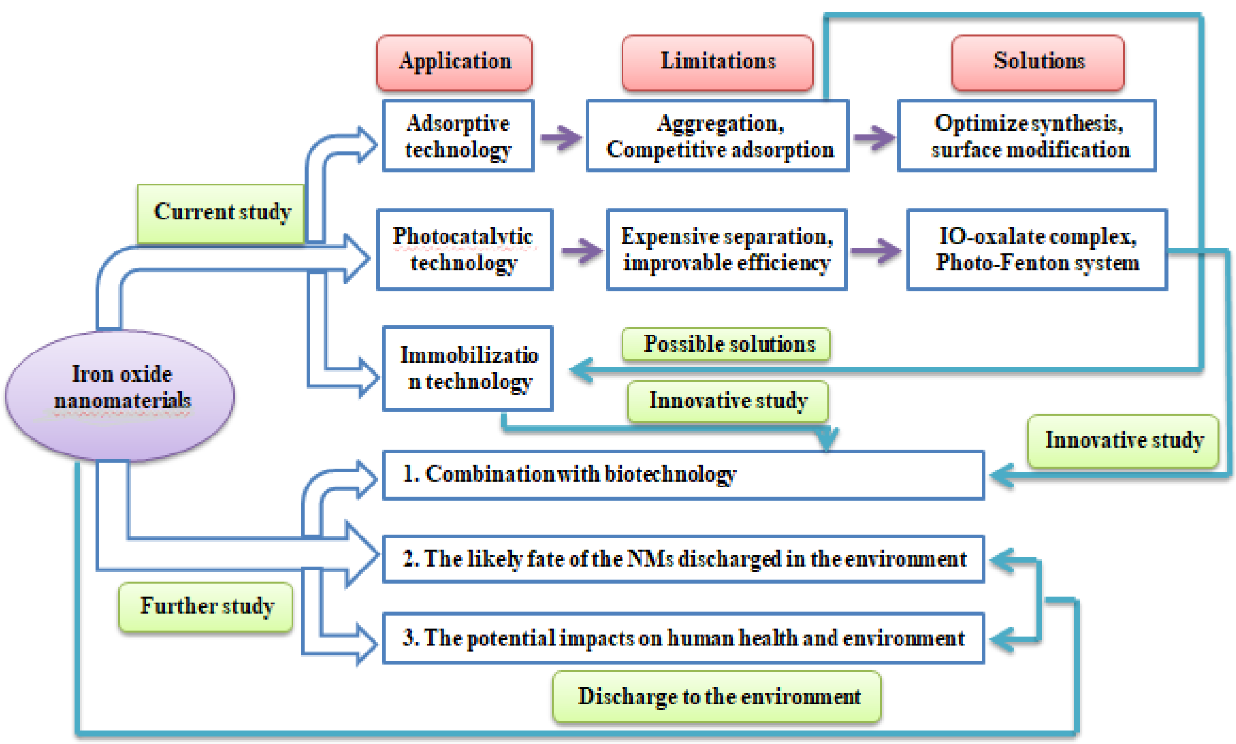

Figure 1.2 Overview of the review structure[69].

1.4 Preparation Methods of Iron Oxide NPs

Briefly, The following three techniques can be used to synthesized iron nanoparticles:as shown in (Figure 1.3)

1. Physical methods: these are complex processes suffer with of being unable to regulate nanometer-sized particle size [70].
2. Chemical preparation methods: these techniques are straightforward, manageable, and effective, allowing the size, composition, and even shape of the NPs to be controlled [62]. Through the coprecipitation of Fe^{2+} and Fe^{3+} with the addition of a base, iron oxides can be created [71]. The type of salt employed, the ratio of Fe^{2+} and Fe^{3+}, the pH, and the ionic strength all affect the size, shape, and composition of iron nanoparticles (NPs) produced chemically.
3. .Biological methods[72]

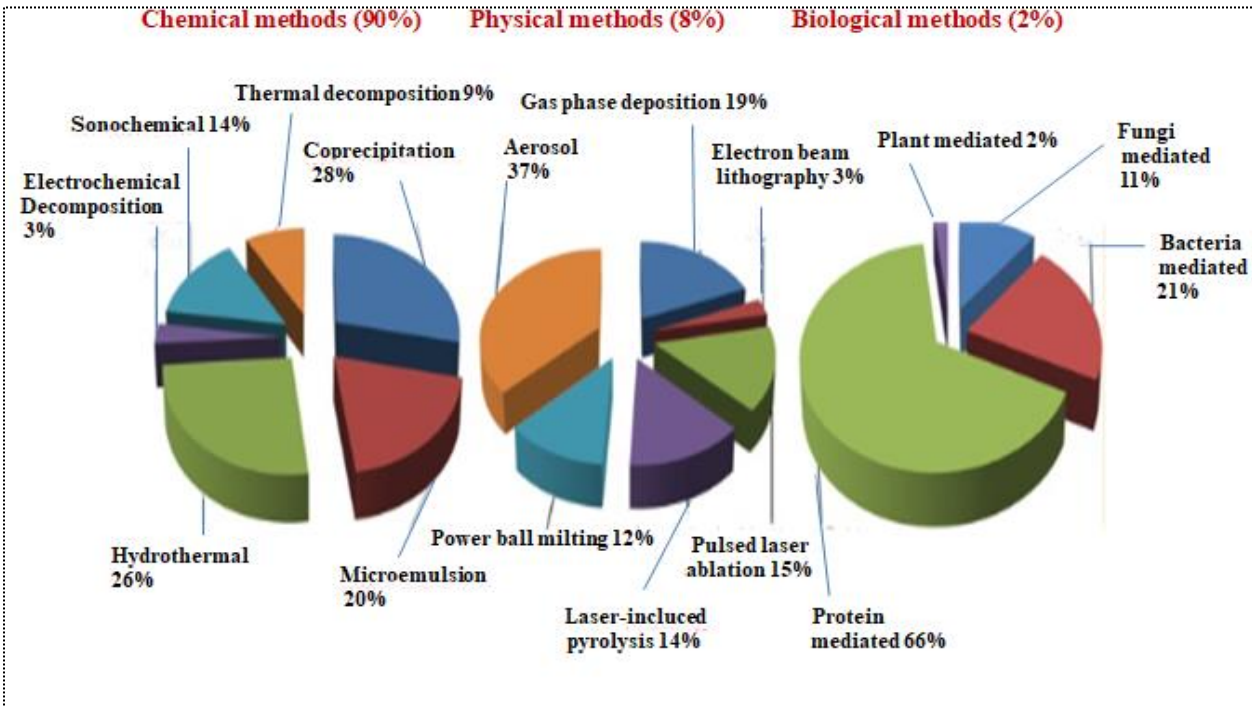

Figure 1.3 A comparison of the many methods used to create superparamagnetic iron oxide nanoparticles[62,71,72].

1.5 Applications of iron oxide NPs

For the magnetic separation of biological products and cells as well as the magnetic guidance of particle systems for site-specific drug delivery, iron oxide NPs were initially used in biology and thereafter in medicine [73,74]. The biodistribution of the NPs is influenced by the magnetic particles' surface chemistry, size, and charge [75]. Due to their use in diagnostic and therapeutic modalities, magnetic carriers and particles have seen an increase in clinical uses over the past few decades. The use of magnetic NPs as a labeling material in the life sciences and numerous other important areas of science has generated considerable interest [76].

1.6 Chemical properties of iron oxide NPs

Iron nanoparticles are highly reactive with oxidizing substances, especially air [77]. Each NPs is covered with a tiny layer of material to prevent it from oxidizing completely and permanently. Different coating materials, like as gold and silica, are employed for this, although they impair the magnetic capabilities of the NPs.

Additionally, magnesium coating is utilized, however it has little impact on the magnetic characteristics of iron particles. Iron nanoparticles are mixed with microscopic magnesium particles in the material that was created, making it complicated. Iron carbide coating is the most practical way for creating virtually entirely magnetic iron particles that are shielded from oxidation; nevertheless, the resulting particles are larger (20-100 nm), polydisperse, and ferromagnetic, thus they are not ideal. Nevertheless, this is significant advancement [78].

1.7 Layer-by-layer Assembled Iron Oxide Based Polymeric Nano-composites

Polyelectrolyte multilayers adsorbed on Iron oxide nanoparticles are very significant for shielding against NPs degradation, modification of surface charge and for changing magnetization features of magnetic cores because of their interaction with polymers [79, 80]. The well-known layer-by-layer (LbL) technique, which allows for the nanoscale tailoring of the chemical and physical properties of multilayered materials, can be used to create polyelectrolyte multilayers on charged substrates [81, 82]. Additionally, the use of this technique causes a surface charge reversal [83, 84], which is determined by electrostatic interactions between the polyelectrolyte chains, solvent and substrate, which are highly influenced by factors including temperature, pH, ionic strength and species concentration [85–87], particularly in the situation of weak polyelectrolytes like Poly(allylamine hydrochloride) (PAH). Nevertheless, when the multilayer of polyelectrolyte simply involves electrostatic interactions, the rise in entropy caused by counter ion release to the bulk is the driving force for self-assembly [88, 89]. Furthermore, the type of polymers used in the LbL technique will affect the high cooperativity between polymer chains (and ultimately, the multilayer's structure). In addition, the following interactions must be considered: interactions between donors and acceptors, steric interactions, hydrogen bonds, hydration interactions, covalent bonds, cycles of adsorption and drying, stereocomplex formation, or specific recognition. The surface charge of the nanoparticle is altered by these interactions, which also affects the stability of colloidal suspensions in solutions [90]. In addition to this The layer-by-layer (LbL) adsorption technique provides a simple and affordable method for multilayer creation and enables the incorporation of a variety of materials into the film structures [91]. The LbL assembly method can therefore be thought of as a flexible bottom-up nanofabrication methodology. It has been effectively used the layer-by-layer (LbL) assembly method, which involves the successive adsorption of various molecules and nano objects [92]. In this method, various intermolecular forces are used to transfer and hold together various components at the surface of a solid support. By controlling the composition, morphology, thickness, and architecture at the molecular level, this method enables the design of both organic-only and organic-inorganic multilayers.

Any solid support surface, from smooth to rough, in any shape, such as flat slides, rods, or beads, and in any size, from macro to nanoscale, can be created to contain LbL nanocomposites. Additionally, the LbL strategy guarantees effective scale-up, financial viability, and automated facilities [93]. When it comes to magnetic nanomaterials, the LbL method can be used to combine different kinds of superparamagnetic iron oxide nanoparticles (IONP) with regular polyelectrolytes, creating nanocomposites with a synergistic combination of qualities from components [94]. In these kinds of nanocomposites, polyelectrolytes are crucial because they not only prevent nanocrystal agglomeration but also ensure the mechanical and chemical stability of the nanomaterial. Additionally, some polyelectrolytes have the ability to respond to temperature gradients or exhibit electrical conductivity, making films into intelligent materials as shown in (Figure 1.4) [95].

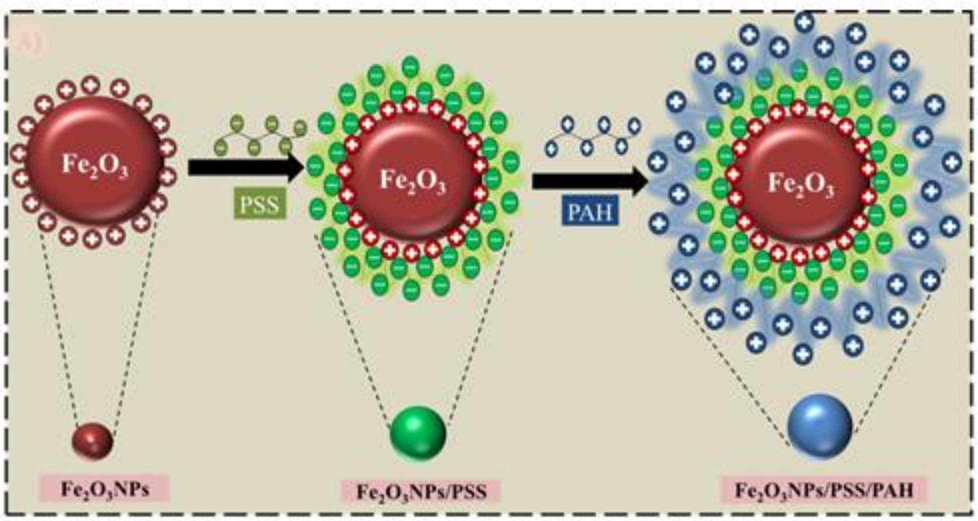

Figure 1.4 Schematic diagram showing the coating of bare Fe_2O_3NPs with two consecutive layers of anionic PSS and cationic PAH polyelectrolytes.

1.8 Polyelectrolyte

Ionic group-containing polymers are known as polyelectrolytes. The fundamental structure of a polyelectrolyte consists of a polymeric backbone and repeating units with functional groups that carry charges [96]. In polar solvents like water, these functional groups undergo partial or total dissociation to become positively or negatively charged. This property makes polyelectrolyte adopt similar properties of both electrolyte and polymer. For example, a polyelectrolyte solution can be both viscous and electrically conductive. Additionally, polyelectrolytes stretch out more due to the repulsion between the charges than neutral polymers do in solution, which results in coil conformation in neutral polymers. Due to the polymer molecules' increased requirement for space and resistance to the solvent stream, the expanded structure increases the solution's viscosity [96]. There are two types of polyelectrolytes: strong and weak. Polyelectrolytes have the ability to entirely or partially dissociate, just as strong and weak electrolytes. Strong polyelectrolytes are those that contain functional groups like sulfonic and quaternary ammine groups that extensively dissociate and are not pH-dependent.

Most of the time, these polyelectrolytes maintain a high surface charge, and this charge is difficult to change. Strong polyelectrolytes, such as poly(diallyldimethyl ammonium chloride, or PDADMAC), are those that contain quaternary amines as functional groups. It keeps its positive charge across a wide pH range. The sulfate group can entirely dissociate from poly(allylamine hydrochloride, or PAH), which is a potent anionic polyelectrolyte. Contrarily, weak polyelectrolytes, such as those with primary or secondary amine (Chitosan) and carboxylic group (Poly(acrylic acid), PAA), have functional groups that are pH dependent and partially dissociate. By adjusting the pH, counter-ion concentration, and ionic strength of the solution, it is possible to change the properties of weak polyelectrolytes, including the level of dissociation and polymer chain conformation.

For instance, the main amine in CS, a weak polyelectrolyte, accepts a proton only when the solution is acidic, causing it to become positively charged. Additionally, PAA is a weak polyelectrolyte that only becomes negatively charged in basic conditions when the carboxylic group loses a proton. Strong coulombic repulsion between charges on the polyelectrolyte backbone stretches and lengthens the polymer chains in a solution devoid of salt. The polymer blobs are surrounded by a large number of counter-ions, which keeps the solution's charge neutral. The electrostatic repulsion between the polyelectrolyte backbones will be reduced, though, if additional counter-ions are introduced to the solution, such as alkali metal salt. As a result, the polymer blob will shrink and become more compact [97]. When the polymer concentration is diluted and semidilutely entangled, the viscosity of the polyelectrolyte solution decreases.

However, when the concentration is higher than the critical concentration, it increases because of the local charge inversion, which results in chain expansion among the entanglements [98]. Natural polyelectrolytes, such as proteins and DNA, as well as naturally derived polyelectrolytes, like cellulose, chitosan (CS), alginin, and heparin, are typically weak, whereas synthetic polyelectrolytes, like those found in PAH, PAA, poly styrenesulfonate (PSS), PDADMAC, and others, contain both weak and strong polyelectrolytes. Solution polymerization can be used to create these polymers [99][100]. polymerization of emulsions [101]. , and precipitation polymerization[102] Polyelectrolytes can alternatively be classified as polyanion, polycation, and polyampholyte depending on the type of charges present on the polymer backbone at a neutral pH. Polycation are typically based on heteroatoms (charges on nitrogen, phosphorus, etc.), with ammonium, phosphonium, and orimidazolium group-containing polymers being particularly prevalent [103].

A few examples of cationic polyelectrolytes include PAH, CS, and PDADMAC. Due to their negatively charged carboxyl and sulfate groups, PAA and PSS are anionic. Proteins are an example of polyampholytes, which are polyelectrolytes with both positive and negative charges. Polybetaines are a unique kind of polyampholytes that carry both positive and negative terminals in each repeating unit. They are rather uncommon and typically small in nature. Instances of stability include thickening and binding of nanomaterials, whereas examples of destabilization include flocculation and oil recovery. The effects of polyelectrolyte on the colloidal stability of particles having a negative charge in an aqueous solution are shown in(Figure 1.5) [104].

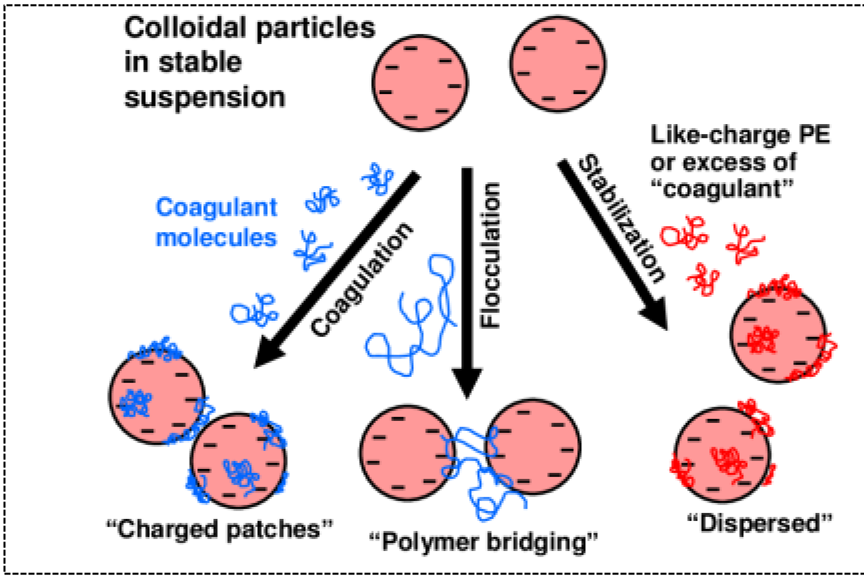

Figure 1.5 Schematic illustration of three ways in which the addition of a polyelectrolyte may affect the colloidal stability of negatively charged particles in an aqueous suspension [104].

1.8.1 Poly(sodium 4-styrenesulfonate) PSS

A cation exchange polyelectrolyte with an average molecular weight of 70000, poly(sodium-4-styrenesulfonate) (PSS), is utilized to create mechanically stable and repeatable coatings on a variety of materials. When grated onto graphene, PSS not only prevents grapheme takes from restacking via van der Waals forces, but it also significantly increases the hydrophilicity. PSS has potential for use in drug delivery and is noncytotoxic as shown in Figure 1.6(A) [105].

1.8. Poly(allylamine hydrochloride) PAH

A cationic polyelectrolyte called polyallylamine hydrochloride average (Mw) 15,000 is created by polymerizing allylamine. It can be used in in combination with an anionic polyelectrolyte, such as poly, to create an adsorbed film of negatively and positively charged polymers that is built up layer by layer. There are numerous biomedical uses for poly as shown in Figure 1.6(B) [106].

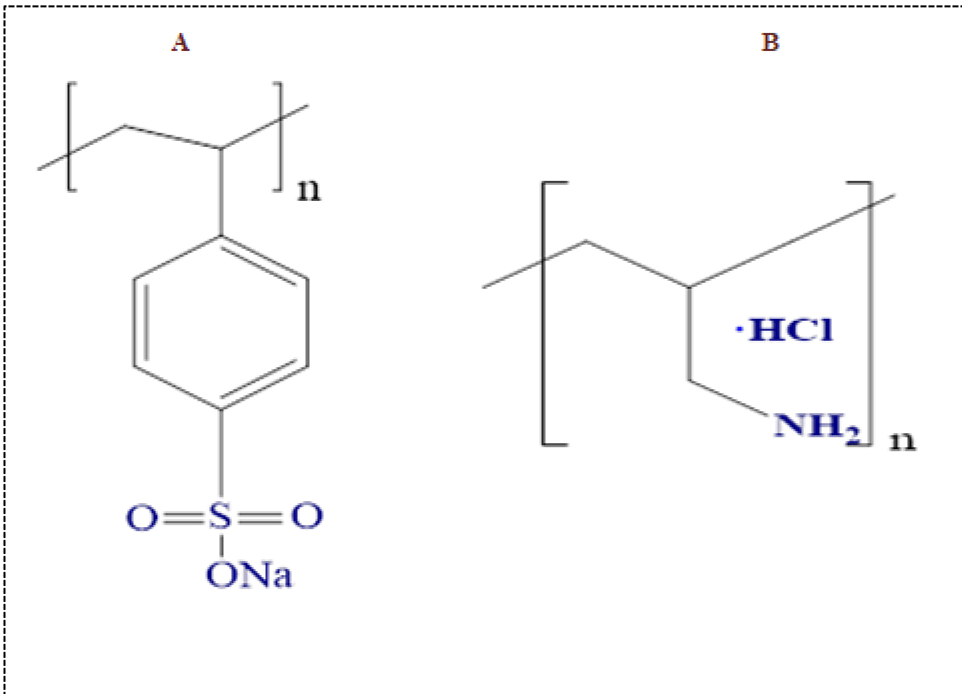

Figure 1.6 A,B The structural formulas of the PSS and PAH [105][106].

1.9 Dyes

dyes are organic chemical compounds that have color due to their ability to absorb light in the visible spectrum (400–700 nm). Because they have a chromophoric structure with an extended conjugated system of p-electrons and frequently bear groups with an electron acceptor or donor, Natural or artificial dyes can be distinguished; artificial dyes have a wide range of structural variations. A variety of dye classes exist, including azo, anthra-quinone, triarylmethine, sulfur, and phthalocyanine [107]. The because of its chemical structure, which is defined by one or more azo groups (-N=N-), azo dyes absorb light in the visible spectrum. A variety of azo dyes can be produced by replacing the azo group with benzene or naphthalene groups, which can contain a variety of substituents, including methyl ($-CH_3$), chloro (-Cl), nitro ($-NO_2$), amino ($-NH_2$), carboxyl (-COOH), and hydroxyl (-OH). Due to their affordability, simplicity of synthesis, stability, and wide range of colors accessible when compared to natural dyes, azo dyes make up the bulk of all textile dyestuffs manufactured.The textile, paper, leather, cosmetic, food, and pharmaceutical industries all employ dyes extensively. The improper disposal of textile dye effluent containing azo dyes in aquatic ecosystems reduces sunlight penetration, which in turn lowers photosynthetic activity, the concentration of dissolved oxygen, and has toxic effects on aquatic flora and fauna that have a global negative impact on the environment. To lessen the influence of synthetic dyes on the environment, a variety of techniques have been used to remove them from water and wastewater, including adsorption, oxidation, filtration, ozonation, microorganisms, and enzymatic methods [108].

1.9.1 Fluorescein Sodium Salt (FSS)

Fluorescein sodium dye, which has the chemical formula ($C_{20}H_{10}Na_2O_5$) as shown in Figure 1.7 and a molecular weight of 376.3g/mol, was a common substance used as a medium and was described by good chemical stability, effective manufacture, and orange-red powder that was dissolved in alcohol[109]. For this study, a non-toxic dye called fluorescein sodium (FSS), also known as uranine, was used [110]. The synthetic organic compound was funded by Adolf Von Baeyer in 1871 [109] This dye belongs to the family of xanthine class dyes, which are distinguished by their effective production and excellent chemical stability of the type of solvent (polarity). FSS has an orange- red to dark crystalline powder that dissolved in water and alcohol (except chloroform).

Figure illustrates the dye's molecular structure (7). In forensics, serology, microscopy, technical chemistry, and other fields, FS has been extensively employed as a fluorescent tracer [109]. In addition to being used as sterile, FS has been utilized for diagnostic purposes in other fields of medicine, including surgery for brain tumors, angiography, and ophthalmology. It is listed on the WHO's list of essential medications. The electrical conductivity and optical characteristics of Fluorescein Sodium Salt (FSS) at a variety of grades (295-370) K were determined. In 2006 the charge transport mechanism of the compound was explained using various conduction types published in literature, and the electronic properties, such as mobility, activation energy, conductivity at room temperature, and optical band gap, were assessed. The conclusion of the study was that the substance is an organic semiconductor. The conductivity of the compound rises with temperature, which suggests that the complex's electron density rises. As a result, this behavior suggests that the substance is an organic semiconductor. The optical band is of the direct transition type, and the electrical parameters are in good accord with those typically established for organic semiconductors as shown in Figure 1.8 [110].

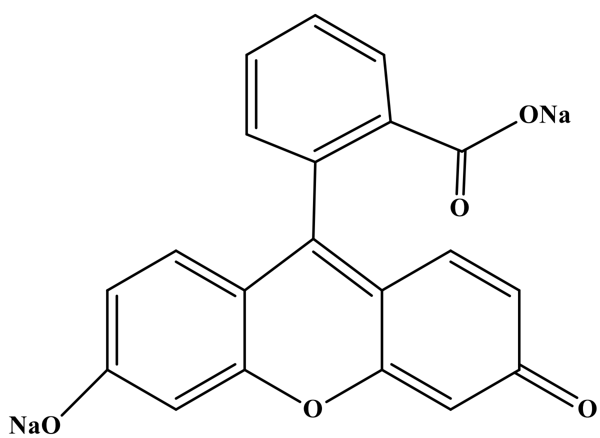

Figure 1.7 The structure of Fluorescein Sodium Salt [111] .

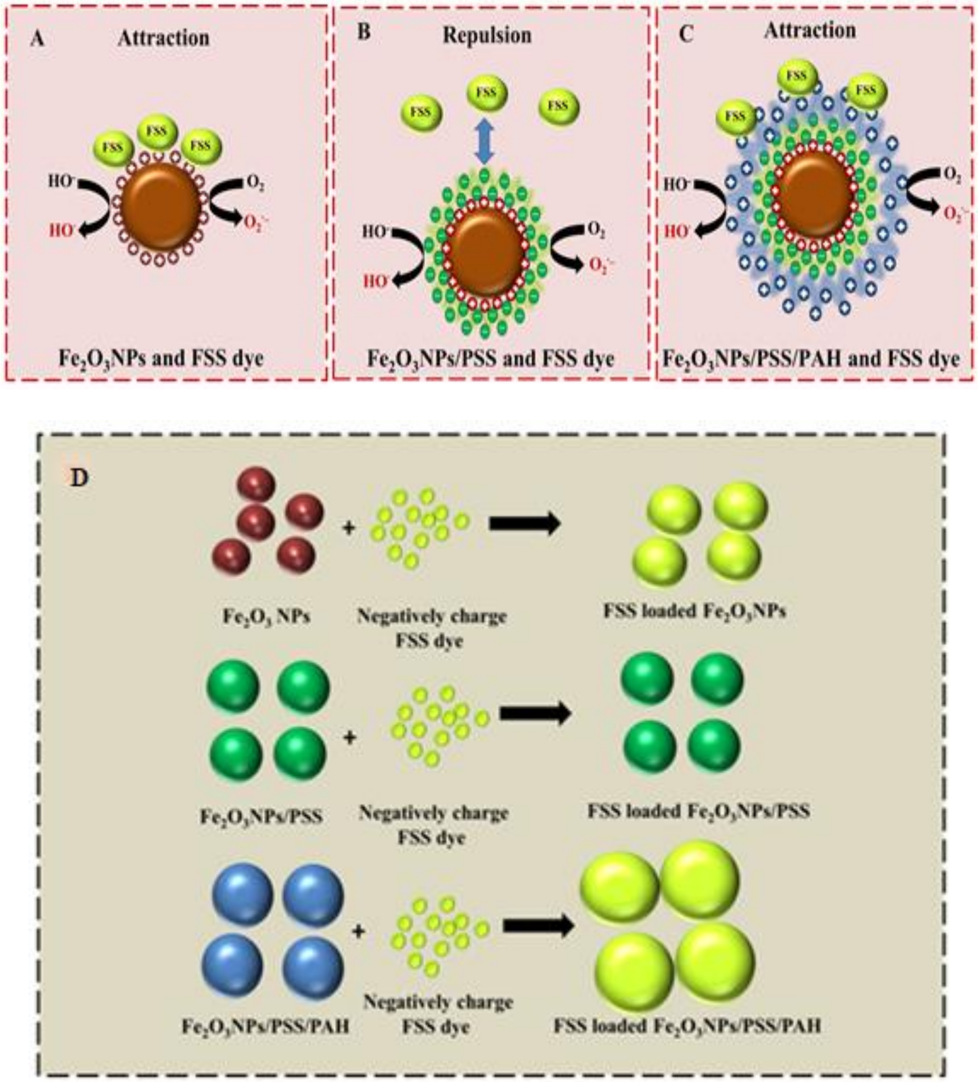

Figure 1.8.Schematic diagram showing the various contacting patterns between the bare and polyelectrolyte-coated Fe_2O_3NPs on FSS dye (**A** and **C**) The adhesion of the uncoated and PAH-coated Fe_2O_3NPs to the FSS dye surfaces is favored because of their opposite surface charges. (**B**) The interaction between the anionic outer surface of the FSS dye and the Fe_2O_3NPs coated with anionic polyelectrolyte is repulsive.**(D)** Schematic diagram showing the adsorption of FSS dye on bare and surface modified Fe_2O_3NPs

1.10 Adsorption principles

Adsorption is the term used to describe the interaction that occurs when a gas or fluid solute forms a subatomic or nuclear film on the surface of a strong or fluid. By working together on the adsorbent, the film is framed from the adsorbate on the exterior of the adsorbent. It hinges on the ability of pore-size permeable materials to store chemicals particularly on the outside of the strong (adsorbent). These adsorbate atoms accumulate on the well of the adsorbent collection and diffuse between body parts. Partition occurs because some particles are held more strongly on the surface than others because to differences in atomic weight, shape, or extremity. Cause some particles to be held more firmly than others on the surface. The adsorbate is generally retained unambiguously enough to allow complete evacuation of that portion of the liquid. Though the adsorption interaction is divided between physical and compound adsorption, the holding concept depends on the species in issue. Each of these cycles is illustrated in the section below [112]

1.10.1 Physical Adsorption

Actual adsorption involves surface-level interactions such as dipole cooperations, hydrogen restricting, and Van der Walls connections. This type of adsorption has an adsorption heat of 20 to 40 KJ/mol. Harmony (between adsorption and desorption) is established immediately because this adsorption doesn't require achieving starting energy. This adsorption lacks the concept of an adsorbent and is an ambiguous, reversible interaction [113]. When the temperature rises, the dynamic energy of the gas particles increases, causing the gas atoms to appear to move away from the adsorbent. This adsorption doesn't just give the compound a surface-level structure; it has several faces on the exterior of the adsorbent. Adsorption is only possible if the pushing factor is increased [114,115].

1.10.2 Chemical Adsorption

Substance adsorption involves surface-level collaborations through a synthetic bond, leading to a very precise arrangement of surface mixtures. This because the adsorption is conceptualized as a single molecule layer, it is made clear that it is irreversible and substantial and that the electronic characteristics of the adsorbents are altered. Powerless compound adsorption, which occurs when the idea of cooperation is a covalent link, and solid synthetic adsorption, which occurs when the idea of association is ionic bonds, are two types of substance adsorption that depend on the idea of constraining adsorbent and adsorbate. Compound adsorption relies on the concept of the adsorbent and necessitates bigger warmth changes (40-400 KJ mol^{-1}) and low temperature since only a particular type of atoms are adsorbed. Activated adsorption is the common name for synthetic adsorption [116].They are because effective at removing toxins, adsorption techniques for wastewater treatment are becoming more common. Adsorption and particle exchange are two systems that lead to decolorization. Many factors affect these two systems, including the connection between the adsorbate and the adsorbent, the surface area, the size of the molecules, the pH, the temperature, and the duration of contact [117].

1.11 Photocatalysis.

Titanium oxide was used to perform the photocatalytic splitting of water by Honda & Fujishima in 1972. Originally, the word "photo catalysis," which has two parts and means "light catalysis," was a Greek word. The definition of this technique was given as the material that produces catalytic activity utilizing light energy [118]. Cycles must be present in the photo catalysis process to prevent reactant deterioration. The photochemical reaction would make use of a wide spectrum of light, including UV, visible, and perhaps infrared. According to the type of phase the reactants and catalyst are in, photo catalysis may generally be divided into two classes: homogeneous photo catalysis and heterogeneous photo catalysis. Both of these classes are capable of producing hydroxyl radicals (OH) [119].

1.11.1 Homogenous Photocatalysis

Catalyst and reactants in this sort of production have the same phases (single-phase) when exposed to near UV radiation. The OH radical is crucial in the deterioration of organic water contaminants like textile dyes. The initial uses of UV light in the photodecomposition of organic pollutants involved the use of UV/ozone and UV/hydrogen peroxide. These uses can be divided into two primary categories .

1- Photo oxidation, in which organic contaminants are attacked by hydroxyl radicals produced when UV light and an oxidant are combined.
2- Direct photo degradation requires UV light to directly excite the organic pollutant [120] .

1.11.2 Heterogeneous Photocatalysis.

In heterogeneous photo catalysis, the catalyst (a semiconductor) and reactants are in different phase under atmosphere O_2 environment and under solar, UV, or visible light. During the irradiation process, a photoelectron is promoted from the valence band to the conductance band, where it donates a positive hole. The generation of the photoelectron hole pair splits by an energy distance known as the band gap. While photo-reduction happens on the conductance band by electron-acceptor species such as O_2, photo-oxidation occurs on the valence band by electron-donor species such as -OH, producing the (OH) used for pollutant degradation [121]. The heterogeneous photo catalysis process has several benefits, including high stability, cheap cost, high activity, and high conversion efficiency.

It is mostly employed in industry and the environment and operates with solar light and UV spectra. Adsorbing them on the photo catalyst increases its efficiency, but when the photo electron-hole was recombined, the efficiency fell [122]. As a rule, metal oxide photocatalysts have large band gaps, which reduce their effectiveness. However, modified photo-semiconductor surfaces have boosted their effectiveness [119].

1.12 photocatalytic and adsorption

The photocatalytic and adsorption activities of free Fe_2O_3NPs and surface-modified Fe_2O_3NPs were examine for the elimination of FSS dye from synthetic dye solutions. Fluorescein dye was quickly and successfully removed from an aqueous solution using surface-modified Fe_2O_3NPs. The ability of the Fe_2O_3NPs to electrostatically attach to fluorescein dye depends on the surface charge of the particles. Here, it was investigating the possibility that covering the Fe_2O_3NPs with an exterior layer of a cationic polyelectrolyte will improve their photocatalytic and adsorption activity, whereas covering them with an exterior layer of anionic polyelectrolyte may decline their photocatalytic and adsorption activity because of electrostatic repulsion from the negatively charged fluorescein dye. The multilayer coverings offer excellent surface coverage and the external PAH layer offers superior photocatalytic and adsorption activity for fluorescein dye. To the best of our knowledge, no research has been done on the application of this type of modification for Fe_2O_3NPs made using the LbL technique and employed for the photocatalytic and adsorption of fluorescein dye. Here, Its show for the first time that surface-modified Fe_2O_3NPs exhibit improved and preferred photocatalytic and adsorption activity for the FSS dye as compared to unmodified Fe_2O_3NPs.

1.13 Mould

Moulds are fungus that can release spores that spread through the air. They grow by creating multicellular filaments (hyphae), which join to form a network known as a "mycelium [123]. Mycotoxins, secondary metabolites produced by mould, are poisonous to both people and animals [123,124]. Moulds can typically grow on a variety of surfaces, both inside and outside, including buildings, food, fibers, wood, and any location where there is moisture, organic material, and oxygen [124]. The growth is distinguished by an unattractive look and a color change that is dependent on the type of mould and the supply of nutrients. The development of mould has been linked to an increase in unfavorable health impacts, such as allergies, headaches, asthma, and respiratory issues, in addition to producing a wide variety of damage to buildings and agriculture [125].

1.14 Antimould

In this study of antimould nanoparticle applications, *Trichoderma* fungus was chose as typical representative of very widespread moulds, which is responsible for multibillion dollar damage to crops, food items and buildings on an annual basis. Testing nanotechnology-based antimould formulations on Trichoderma fungus can help to combat many other members of the Aspergillus and Penicillium genres of moulds and become aware of the mechanisms of their antimould resistance. *Trichoderma* fungus has high rates of proliferation, making them suitable for culturing in lab conditions [42, 126]. Moulds are fungus that can release spores that spread through the air. They produce multicellular filaments (hyphae), which link to form a network known as a "mycelium," as they grow. Secondary metabolites from mould, sometimes known as mycotoxins, can be harmful to both animals and humans. Moulds can typically grow on a variety of surfaces, both inside and outside, including food, buildings, wood, fibers, and any location where there is moisture, organic material, and oxygen [42, 126, 127]. There are several antimould agents that are dangerous to humans and can harm the environment. Thus, there is a critical need to create more effective antimould formulations and agents that may be used both inside and outside and at lower doses.

Trichoderma fungus was also used as model fungal species, to evaluate the antifungal action of the PAH, PSS functionalized Fe_2O_3NPs, compared with non-modified (bare)

Fe_2O_3NPs (Figure 1.9). Here, it was investigating the possibility that covering the Fe_2O_3NPs with an exterior layer of a cationic polyelectrolyte will improve their photocatalytic, adsorption and antimould activity, whereas covering them with an exterior layer of anionic polyelectrolyte may decline their photocatalytic, adsorption and antimould activity because of electrostatic repulsion from the negatively charged fluorescein dye and *Trichoderma* fungus. It was illustrate this design schematically in Figure 1.9. In the present work, Fe_2O_3NPs was created using the precipitation process at 200 and 500 °C of calcination temperatures. The primary advantages of the precipitation method are its high production and low minimum temperature requirement, which inhibits the creation of large grains. The production of iron oxide nanoparticles was also described, their characterisation, and surface modifications utilizing two polyelectrolytes. Here, it was investigate how the adsorption and photocatalytic activity of Fe_2O_3NPs with FSS dye is influenced by surface coatings consisting of anionic poly(sodium 4-styrenesulfonate (PSS) and cationic poly(allylamine hydrochloride (PAH) polyelectrolytes as shown in Figure 1.8A-C. The photocatalytic and adsorption activities of free Fe_2O_3NPs and surface-modified Fe_2O_3NPs was examined for the elimination of FSS dye from synthetic dye solutions. Fluorescein dye was quickly and successfully removed from an aqueous solution using surface-modified Fe_2O_3NPs. The ability of the Fe_2O_3NPs to electrostatically attach to fluorescein dye depends on the surface charge of the particles.

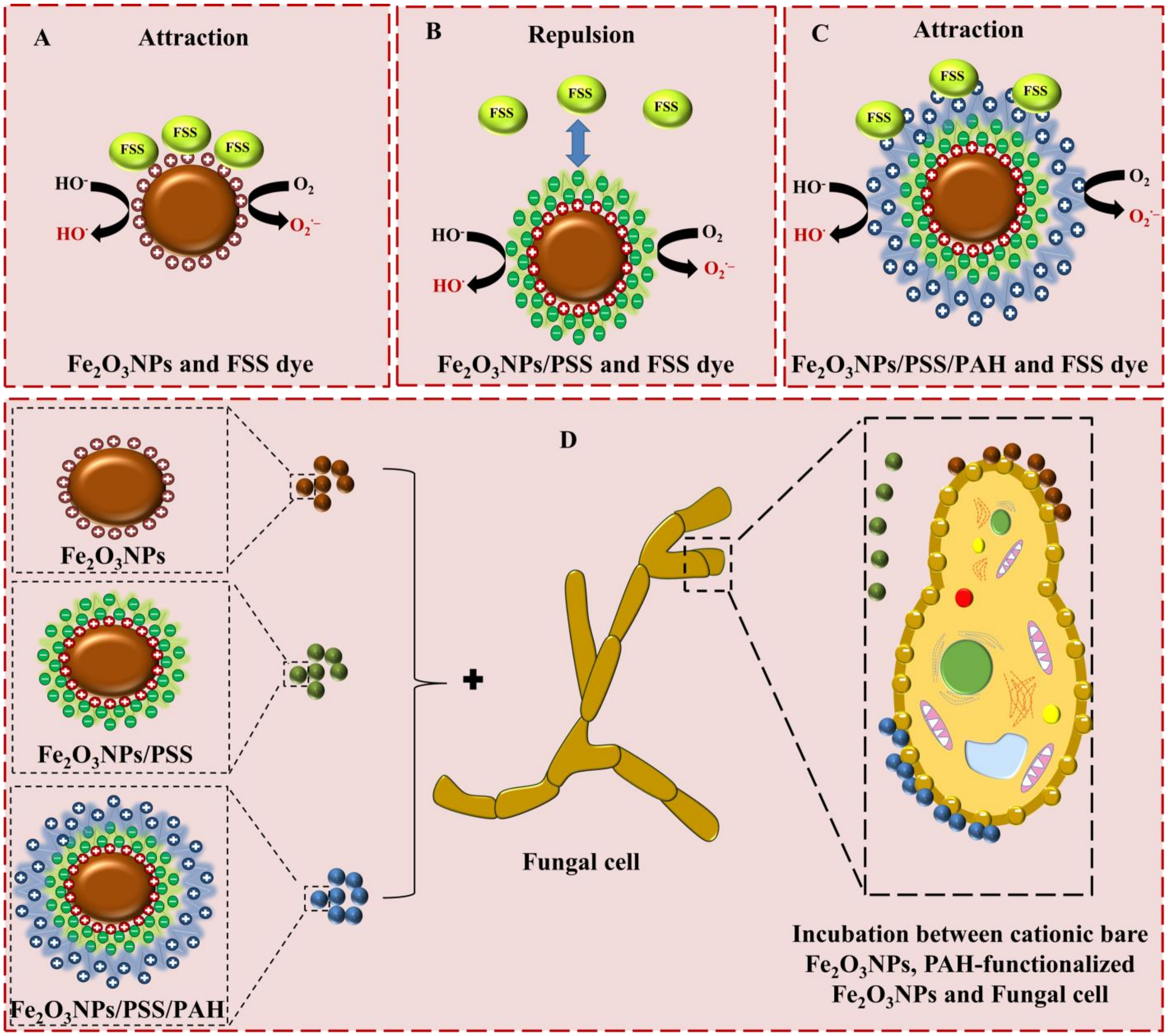

Figure 1.9 Schematic diagram showing the various contacting patterns between the bare and polyelectrolyte-coated Fe_2O_3NPs on FSS dye and *Trichoderma* fungus. (**A** and **C**) The adhesion of the uncoated and PAH-coated Fe_2O_3NPs to the FSS dye surfaces is favored because of their opposite surface charges. (**B**) The interaction between the anionic outer surface of the FSS dye and the Fe_2O_3NPs coated with anionic polyelectrolyte is repulsive. (**D**) The schematic of the electrostatic interaction between bare Fe_2O_3NPs and PAH-coated Fe_2O_3NPs and the outer cell membrane of *Trichoderma* fungus.

Literature Review.

1. Norio Taniguchi used nanotechnology for the first time in 1974 [14]. Nanomaterial composition and real properties, such as their melting point, color, charge limit, and attractivity, can differ from those of mass materials with a comparable configuration[15].

2. Following notions presented by Richard Feynman in 1959 in the Unique chemical and physical properties that make them superior to bulk substances at least one dimension (1-100 nm in length, width, or thickness) [13] [14].

3. To remove dyes from wastewater, a variety of techniques are used, including filtration, precipitation, adsorption, photodegradation, and chemical degradation [1, 30–34].

1.15 Aims of current research

This work aimed to develop nanoparticle formulations for adsorption, photocatalytic activity and antifungal action. The objectives of this study were:

(i) To prepare and characterize various particle sizes of iron oxide nanoparticles by the direct precipitation method after calcination at temperatures (200 and 500 °C).

(ii) To examine the impact of calcination temperatures on particle size and surface charge of iron oxide nanoparticles.

(iii) To coat the bare Fe_2O_3NPs with a layer of anionic poly(sodium 4-styrenesulfonate (PSS) and a layer of cationic poly(allylamine hydrochloride (PAH) polyelectrolytes in order to control the size, stability and nanotoxicity of Fe_2O_3NPs.

(iv) To measure the change of the surface charge of Fe_2O_3NPs upon coating them with PSS and PAH.

(v) To assay the adsorption and photocatalytic activity of bare Fe_2O_3NPs, Fe_2O_3NPs/PSS, and Fe_2O_3NPs/PSS/PAH on FSS dye in both dark conditions and in the existence of UV light.

(vi) To examine the antifungal activity of bare Fe_2O_3NPs, Fe_2O_3NPs/PSS, and Fe_2O_3NPs/PSS/PAH on *Trichoderma* fungus.

2-Experimental Part

2.1 Chemicals Materials

Table 2.1 Preparation chemicals utilized in this study project

NO.	Name of substance	Chemical formula	% Purity	Supplied Company
1	Iron trichloride hexahydrate	$Fecl_3.6H_2O$	99%	Sigma-Aldrich
2	Ammonium Hydroxide	NH_4OH	98%	Fisher Chemical
3	Sodium Chloride	NaCl	98%	Nanoshel–USA
4	Ethanol	C_2H_5OH	99%	BDH
5	Fluorescein Sodium salt	$C_{20}H_{10}Na_2O_5$	99%	Sigma Aldrich
6	Poly sodium 4-Styerenesulfonate	$(-CH_2CH(C_6H_4SO_3Na)-)n$	99%	Sigma Aldrich UK
7	Poly allylamine Hydrochloride	$(CH_2CH(CH_2NH_2 \cdot HCl$	99%	Sigma Aldrich UK

2-2. Instrumentations Analysis

Table 2.2 shows various instruments and equipment are employed for preparation and characterization.

Instrument	Specifications	Laboratory
Scanning electron microscope	S-4160/ Hitachi	Nano-Electronic Lab, University of Tehran, Iran

(SEM)		
Transmission electronic microscopy (TEM)	Carl Zeiss EM900/ Germany	Central Lab, Sharif University of Technology, Tehran, Iran
Energy dispersive X-ray analysis (EDX)		Chemistry department, college of science, University of Tehran, Iran
Fourier transform Infrared spectroscopy (FT-IR)	SHIMADZU FT-IR 8400S/ Japan	Chemistry department, college of science, University of Tehran, Iran
X-ray diffraction (XRD)	SHIMADZU (XRD) 6000 X-Ray Target Cu K, α radiation (λ=1.54180Å)/ Japan	Chemistry department, college of science, University of Tehran, Iran
Electronic spectra (UV-Visible)	SHEMADZU 1800 Double Beam, Japan	Chemistry department, college of science, Babylon University
Furnace oven	Muffle Furnace Size-Two Gallenkamp	Chemistry department, college of science, Babylon University
BET surface area	Micrometrics, 2023, Germany	Chemistry department, college of science, University of Tehran, Iran
Drying Oven	Salden-Nabertherm LH30/12 Germany	Chemistry department, college of science, Babylon University
Electric balance	CPA224S, Germany	Chemistry department, college of science, Babylon University
Heating magnetic stirrer	220V, 2000w/ Taiwan	Chemistry department, college of science, Babylon University
Centrifugations	C 41 7800 r.p.m/ France	Chemistry department, college of science, Babylon University
Ultrasonic cleaner	220v , 30watt/ China	Chemistry department, college of science, Babylon University
Sonication	220/240 V Italy 50/60 Hz	Chemistry department, college of science, Babylon University

2.3 Method

2.3.1 Synthesis of Iron Oxide Nanoparticles

The synthesis of Fe_2O_3NPs from NH_4OH as a precipitating agent and $FeCl_3.6H_2O$ as a precursor was carried out using the direct precipitation method. The first step was to dissolve 4 g of $FeCl_3.6H_2O$ in 100 mL of distilled water under stirring at room temperature. Then, a 50 mL aqueous solution of 2 M of NH_4OH solution was added dropwise to the $FeCl_3.6H_2O$ solution under stirring. The resulting black dispersion was heated for 3 h at 80 °C while being continuously stirred at room temperature to produce a brown powder. The resulting sediment was collected by centrifugation at 6000 rpm and washed three times with ethanol and distilled water and finally dried at 80 °C as shown in (Figure 2.1). The final product was cooled to room temperature and calcined at (200 and 500 °C) for 4 h [128].

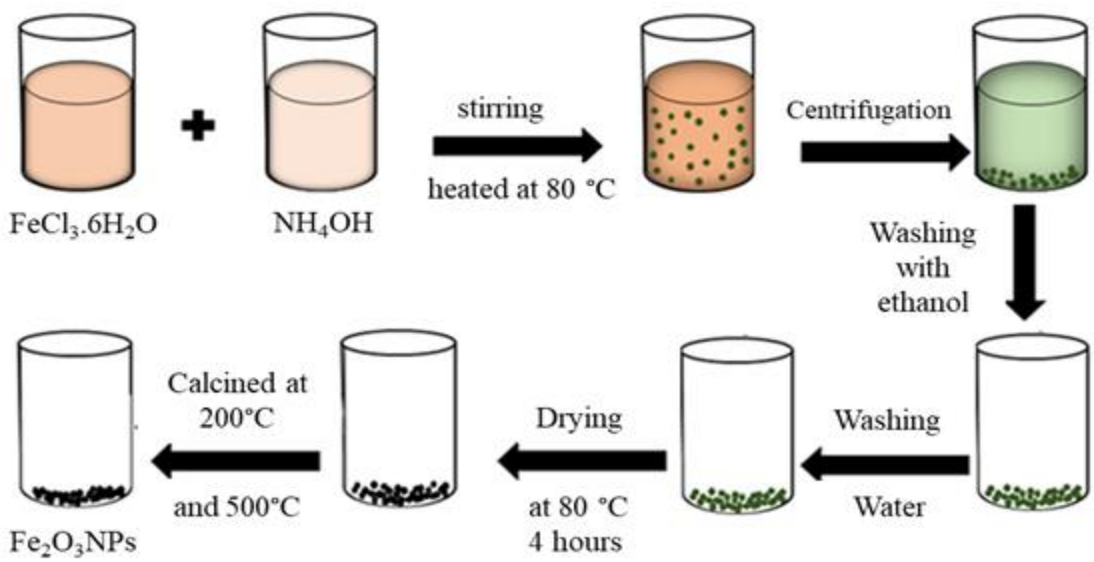

Figure 2.1 A schematic overview is summarizing of the synthesis method of Fe_2O_3NPs.

2.3.2 Preparation of Polyelectrolyte-Coated Fe_2O_3NPs

Polyelectrolyte-coated Fe_2O_3NPs were prepared using Fe_2O_3NPs synthesized after annealing of Fe_2O_3 at 200 and 500 °C. The first step was to disperse 2.5 g of Fe_2O_3NPs in 25 mL of distilled water with sonication for 30 min at room temperature. Fe_2O_3NPs dispersion was added dropwise to an equal volume of 2.5 g in 25 mL anionic polyelectrolyte PSS solution in 1 mM NaCl. The samples were homogenized for 1 h on an orbital shaker, and then the excess PSS was removed by centrifuging them for 1 h at 8000 rpm after being rinsed three times with distilled water. The zeta potential distributions and particle size of the Fe_2O_3NPs/PSS particles were measured after they had been resuspended in 25 mL of distilled water. The Fe_2O_3NPs/PSS suspension was added dropwise into 2.5 g in 25 mL of cationic polyelectrolyte PAH solution that was dissolved in 1 mM NaCl to create PAH-coated Fe_2O_3NPs as shown in (Figure 2.2). The formed nanoparticles was shaken for 1 h and centrifuged three times for 1 h at 8000 rpm to create Fe_2O_3NPs/PSS/PAH [87]. The zeta potential and particle size of the surface-functionalized Fe_2O_3NPs (with PSS and PAH) were measured by dynamic light scattering.[87]

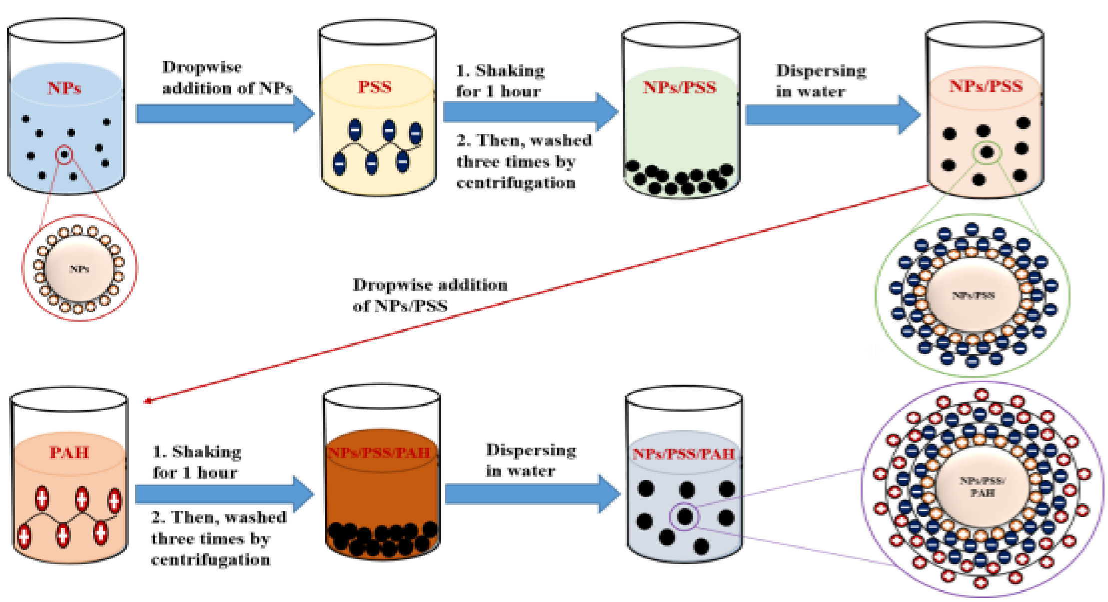

Figure 2.2. The schematic diagram of LbL polyelectrolytes coating of nanoparticles.[129]

2.4 Characterization of the synthesized materials.

All the formed nanoparticles were characterized separately, for their morphology, structural, surface properties, and chemical composition. For this purpose various techniques were used, such as dynamic light scattering (DLS), scanning electron microscopy (SEM), energy dispersive X-ray analysis (EDX) Transmission Electron Microscopy (TEM), Fourier Transform Infrared (FTIR), UV-Vis Spectrophotometer, BET and X-ray diffraction (XRD).

2.4.1 Scanning electron microscopy (SEM)

SEM was used to examine the prepared materials' surface morphology. This method utilizes a finely focused beam of electrons from an electron source that may be thermionic like a tungsten filament (in some regular SEM) or may be a field emitting source to provide an image in one dimension of the scanned sample and demonstrate the relative homogeneity of the investigated samples (in SEM). SEM Hitachi model S-4160 pictures from the Nano-Electronic Lab at the University of Tehran, Iran, were used for the investigation. Figure 2.3 displays an image and a general breakdown of the key elements of SEM[130].

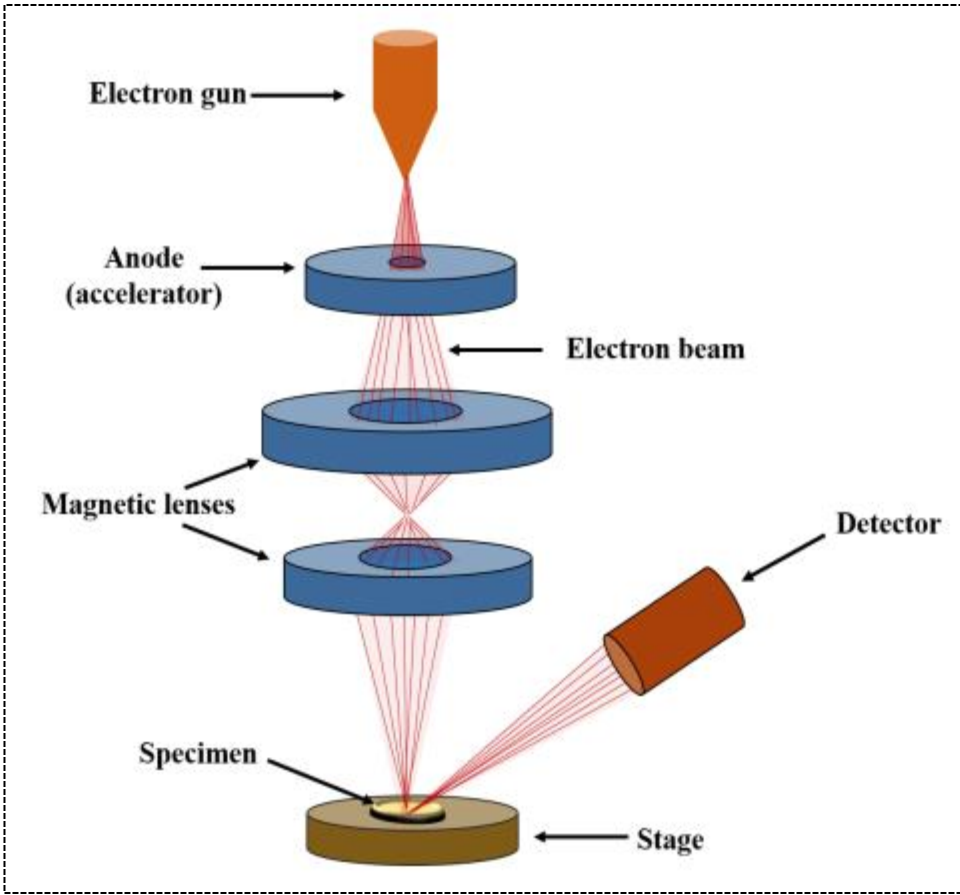

Figure 2.3 Schematic diagram of the components of scanning electron microscopy. Redrawn from ref.[131].

2.4.2. Transmission electron microscopy (TEM)

This device is frequently employed for examining the morphology of a material's surface. In this technique, sample preparation is done under a high vacuum, and the samples also need to be modulated into thin layers . A transmitted electron has a wave-like quality that is relevant to the de Broglie equation in terms of TEM operation.

$\lambda = h/mv$ or $\lambda = h/p$ ………………….2.1

We used a Carl Zeiss EM900, manufactured in Germany, at the Nano-Electronic Lab of the University of Tehran in Iran. Samples were prepared by deposition carbon foil on a plate that is supported by a copper grid. Figure 2.4 depicts a general description of TEM compartments.[132].

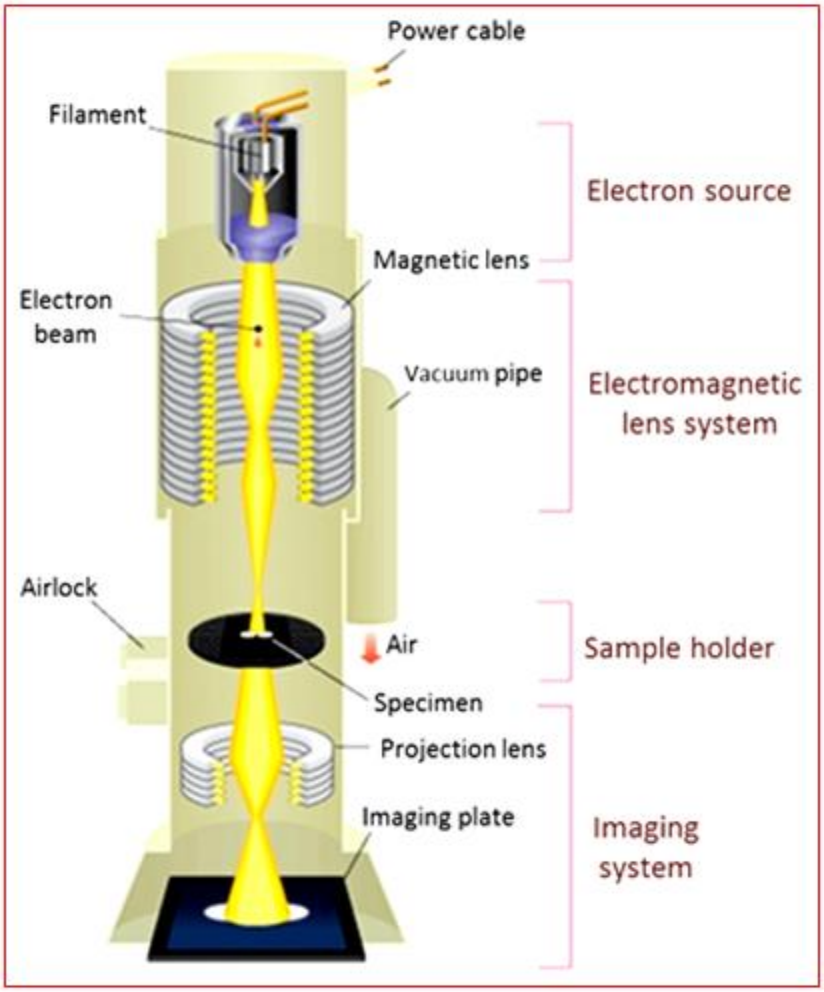

Figure 2.4 Schematic diagram shows the main units of a TEM.[132].

2.4.3 X-ray diffraction(XRD)

XRD method was used to examine the crystal structure of the produced materials and created composites. XRD is typically used to analyze the crystal structure of solid materials . By using Sheerer's formula on the XRD data, the crystalline size can be calculated.

$$L(D)= K. \lambda / B.COS\Theta \ldots\ldots\ldots\ldots 2.2$$

where k is Scherrer's constant and L is the average crystallite size (0.94)

depending on the crystal's form, x-ray wavelength (0.15406 nm for Cu k), full width at half maximum (FWHM) intensity expressed in radians (initially measured in degrees, then multiplied by (/180) to convert to radians), and diffraction (Bragg) angle.

completed in The University of Tehran in Iran the XRD patterns using a SHIMADZU (XRD) 6000 X-Ray diffraction spectrometer with a high-intensity Cu K, radiation (=0.15406 nm) and a graphite monochromatic source. Figure 2-5 provides a visual representation of the XRD system used in this investigation.[133]

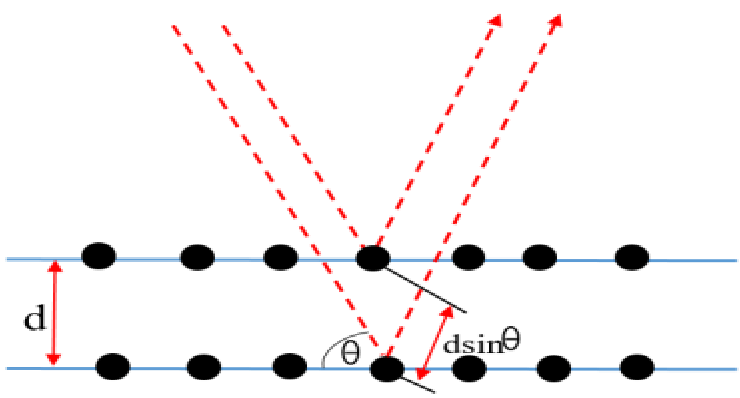

Figure 2.5. Bragg diffraction appeared by the interaction between X-rays and a crystalline sample.[134].

2.4.4 Fourier transform infrared (FTIR)

Utilizing FTIR spectroscopy, functional groups at the surface of the produced materials were investigated . In order to determine the surface characteristics of the Nano products, FTIR spectra were taken using a KBr disc and a (SHIMADZU FT-IR 8400S) instrument operating in the 4000–400 cm-1 range. in the University of Tehran in Iran, FTIR measurements were performed[135].

Figure 2.6 Pictorial for FT-IR machine presentation

2.4.5 BET-Surface Area Measurements Instrument.

The prepared materials' specific surface areas (BET) were calculated using the BET relation, which was based on the N_2 gas's adsorption at -196°C. To get rid of all pre-adsorbed species, the tested sample was dried at about 110°C while being flushed with N_2. In Figure 2.13, a schematic picture of this method is displayed [136].

Figure 2.7 Image of surface area analyzer[136].

2.4.6 Energy dispersive X-ray analysis (EDX)

The Energy Dispersive X-ray (EDX) microanalysis method of elemental analysis is based on the production of distinctive Xrays that indicate the presence of elements present in the specimens and is connected to electron microscopy [137]. The last ten years have seen a significant improvement in the characterization of nanoparticles thanks by the increasing availability of three-dimensional structural data from electron tomography. With this method, the sample is tilted at various angles along one or more axes while a series of photographs are taken at each tilt angle. Using this information and a dependable tomographic method, the three-dimensional sample volume may be recreated as shown in Figure 2.3 [138].

2.4.7 Dynamic Light Scattering (DLS)

A Zetasizer Nano ZS (Malvern) was used to examine the hydrodynamic diameter by DLS. DLS relies on upon illuminating the sample with a monochromatic beam of laser light which is scattered into an indicator situated at an angle (θ) identifying with the transmitted light, which permits the estimation of the size dissemination of solutions. Figure 2.9 shows a schematics diagram of the Zetasizer Nanoseries NanoZS instrument.

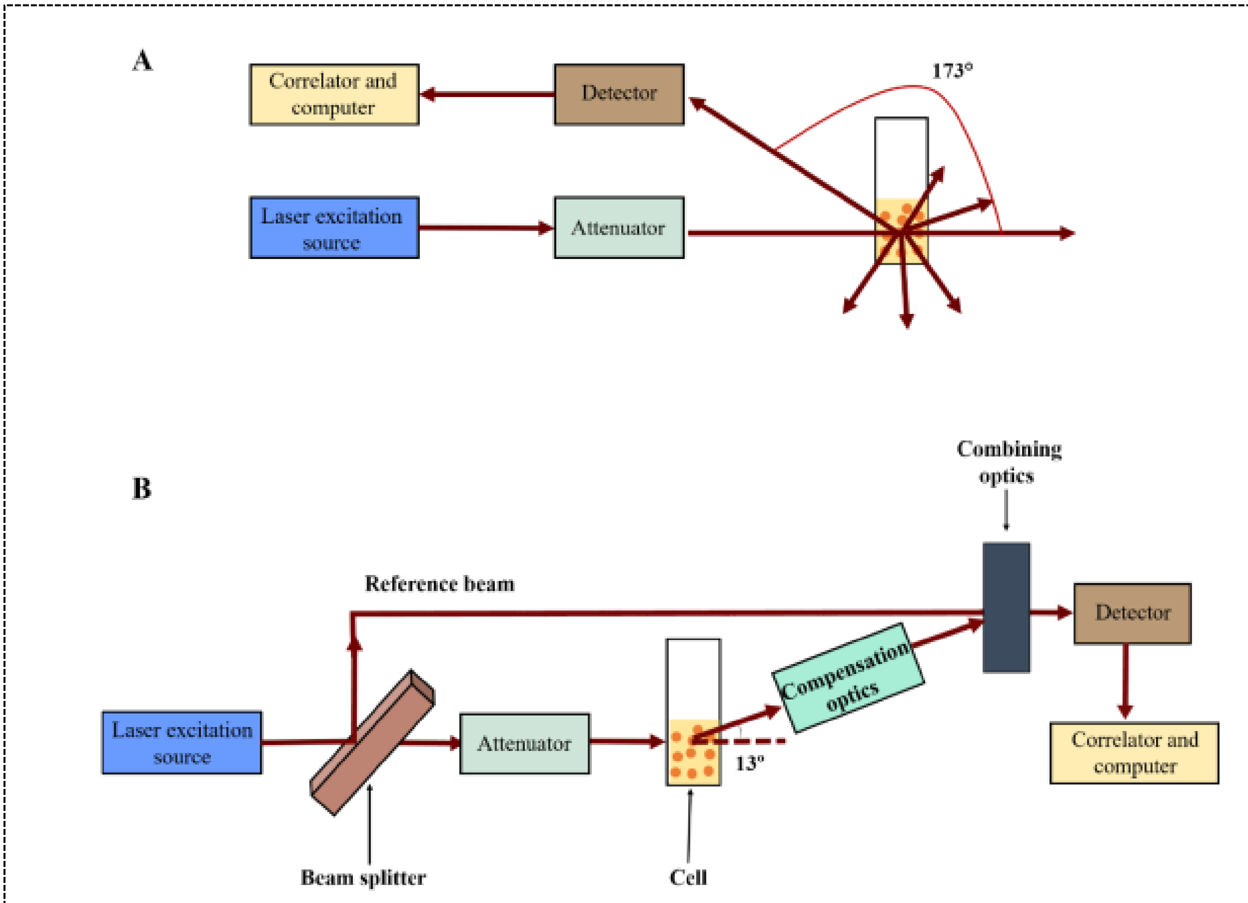

Figure 2.8 Schematic representation of the Zetasizer Nanoseries NanoZS (Malvern instruments) for the measurement of the (A) average diameter and (B) zeta potential. Redrawn from ref. [139]

2.4.8 Zeta potential

Z.P. is a parameter that can be utilised for examining and anticipating colloid stability and surface morphology. [140] It can be characterized as the electric potential (ψ) in the electric double layer at the shear plane between a moving charged particles and the stable liquid phase in which a particle is suspended. At the point when particles are put in an aqueous suspensions, an electric double layer is formed around them with one layer comprised of ions unequivocally adsorbed on the surface of the particles and this layer is named (Stern layer). On the other hand, the other layer is enveloped of diffusely distributed ions, as appeared in Figure 2.10. The last part of the potential variance is known as the zeta potential, and it is measured at the shear plane; thus, the zeta-potential is an estimation of the amount of charge present on the particle surface on the shearing part of the dispersing media.

The Z.P. of any dispersion is impacted by the surface chemistry. The surface chemistry can be varied by any number of means involving a variation in the salt concentration, pH, surfactant concentration, and other formulation choices. It is, consequently, frequently desirable to examine how pH influences the Z.P. of dispersion. An isoelectric point estimation concentrates how pH impacts Z.P. and determines at which pH the Z.P. equals zero. In addition to that, the size of the NPs can be changed by varying the pH of a solution [141].

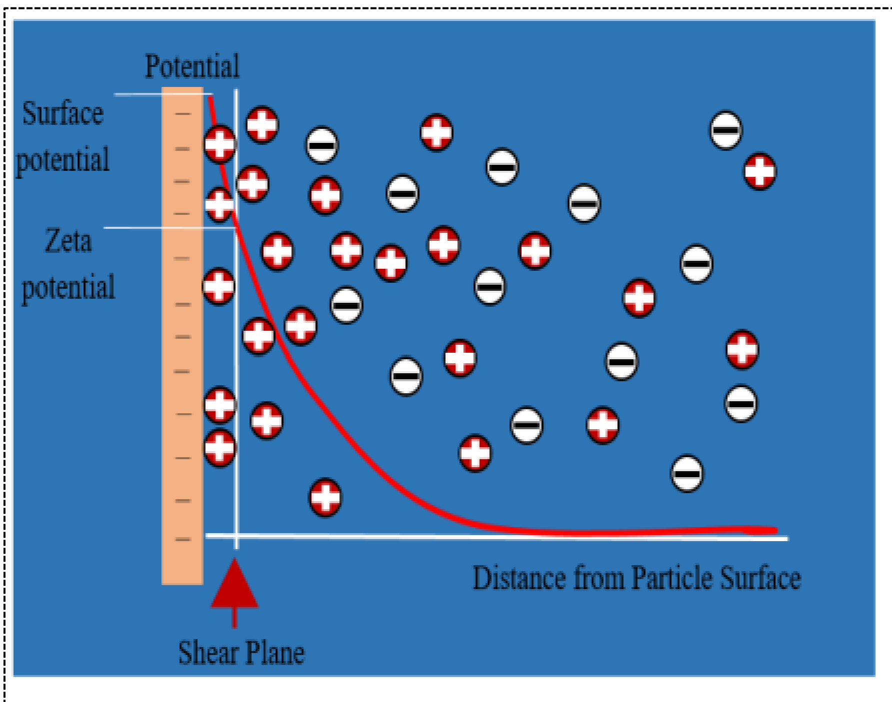

Figure 2.9 The schematic diagram of zeta potential which demonstrating the distribution of ions around the charged particle.[141].

2.5 Adsorption and Photocatalytic Experiments

The adsorption ability of the uncoated and surface-coated Fe_2O_3NPs to adsorb dye was examined using FSS dye. A UV-Vis spectrophotometer with a 490 nm setting was used to record the experimental results. Firstly, uncoated Fe_2O_3NPs and surface-coated Fe_2O_3NPs were prepared and mixed with 100 cm^3 of FSS dye solutions. The solutions were regularly shaken for 60 min in the dark using a platform shaker as shown in (Figure 2.12A). Was measured the absorbance at the maximum absorption wavelength both before and after adsorption. The removal percentage (R %) of FSS dye on uncoated and surface-coated Fe_2O_3NPs was calculated by batch adsorption experiment, that consisted of placing 100 cm^3 solution of 10 mg L^{-1} of FSS dye with 0.2 g of bare and surface-coated Fe_2O_3NPs in conical flasks. The free Fe_2O_3NPs and surface-coated Fe_2O_3NPs with FSS were gently shaken in the dark at 25 ± 5 °C till they reached equilibrium. The shaker speed was set at 230 rpm. Equations 1, 3, and 4 in the Supporting Information were used to calculate the FSS removal % and the amount of FSS adsorbed per unit mass of adsorbent at equilibrium Qe (mg g^{-1}) and at a specific time Qt [29].

The photodegradation activity of FSS dye with bare Fe_2O_3NPs, Fe_2O_3NPs/PSS, and Fe_2O_3NPs/PSS/PAH was also examined in the presence of light. Four 15 W mercury lamps from Philips (CLEO), Poland, were used in the photocatalytic experiment, which was carried out in a photochemical reactor. The uncoated and surface-coated Fe_2O_3NPs were irradiated with FSS in conical flasks using a platform shaker as presented in (Figure 2.12B). In all of the photodegradation experiments, 0.2 g of uncoated and surface-coated Fe_2O_3NPs was suspended in 100 cm^3 of an aqueous solution of FSS dye. After illumination, 3 cm^3 of the reaction suspension was taken, and the bare Fe_2O_3NPs, Fe_2O_3NPs/PSS and Fe_2O_3NPs/PSS/PAH were extracted by spinning the mixture for 15 minutes at 4000 rpm in a centrifuge. A second centrifugation was found to be necessary to separate out small bare and surface-coated Fe_2O_3NPs particles [29]. After the second centrifugation, the absorbance of FSS at 490 nm was recorded. The photodegradation efficiency (PDE) of FSS was also calculated according to equation 2 in the Supporting Information.

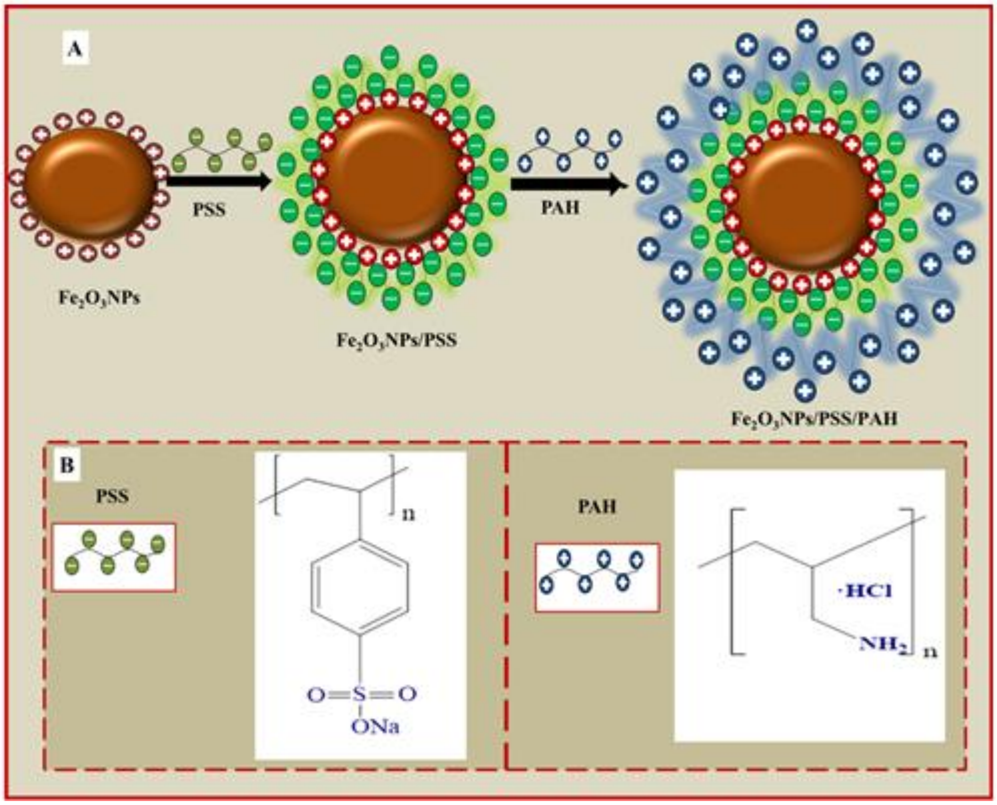

Figure 2.10 (**A**) Schematic diagram of the PAH, PSS functionalized Fe_2O_3NPs by using the layer-by-layer technique. The PSS-loaded Fe_2O_3NPs was surface coated with PAH (cationic polyelectrolyte). (**B**) The structural formulas of the PSS and PAH.

Figure 2.11 (A) The adsorption reactor and (B) the photocatalytic reactor.

2.6 Calibration Curve

Using standard(FSS) dye aqueous solutions, the calibration curves were produced. The absorbance of each concentration was measured at 490 nm using the fluorescein sodium salt dye, whose molar mass is 376.27 g mol^{-1} and whose chemical formula is $C_{20}H_{10}Na_2O_5$.

Table (1.3) exhibit the typical calibration values.

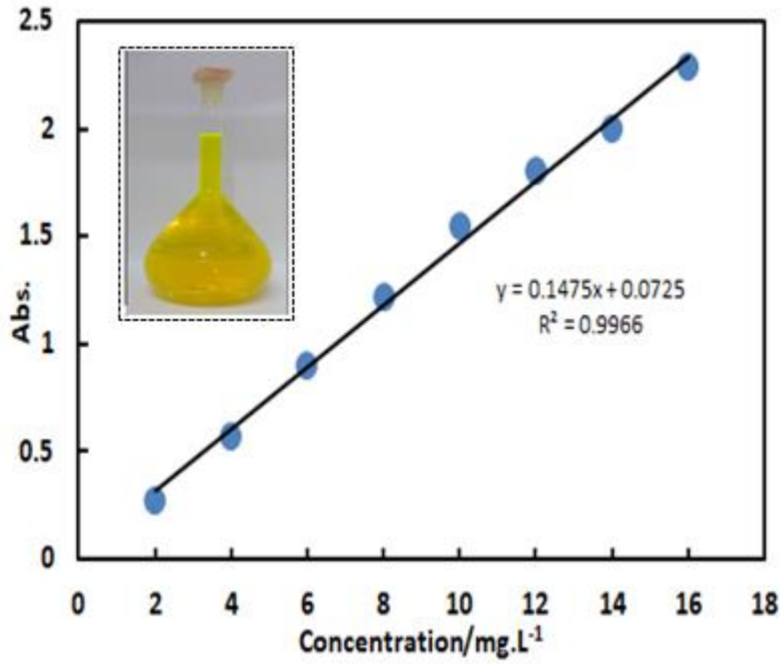

C mg.L^{-1}	Abs
2	0.272
4	0.573
6	0.898
8	1.218
10	1.543
12	1.805
14	2.005
16	2.287

Figure 2.12 Calibration curve for different concentrations of FSS dye and measured at 490 nm.

2.7 Preparation of the Fungus Growth Medium

The Czapek-Dox medium, which contains 3 g sodium nitrate, 30 g sucrose, 1 g potassium dihydrogen phosphate, 0.5 g magnesium sulphate heptahydrate, 0.01 g ferrous sulphate, and 0.5 g potassium chlorate in 1 L of water, was used to generate the culture media for fungus growth. The Czapek-Dox medium was sterilized at 121 $^{\circ}$C under high pressure for 20 min prior to cultivating *Trichoderma* fungal hyphae. For around 3 days, many *Trichoderma* fungal hyphae that had been activated were incubated in 100 mL of culture media at 37 $^{\circ}$C and 150 rpm of shaking. The fungal could appear in the shape of enormous pellets under these conditions. A magnetic stirrer was used to agitate the sample vigorously (1500 rounds per minute) in order to obtain a fungal mycelium dispersion. A refrigerator set to 4 $^{\circ}$C was used to keep the prepared disseminated fungal hyphae for future use.

2.7.1 Testing of the Antimould Activity of Surface Functionalized Fe_2O_3NPs towards *Trichoderma* fungus

1000 mL of deionized water was used to dissolve 40 g of potato dextrose agar (PDA). The PDA was then dissolved by boiling the solution. The flask was cooled for an additional 15 min after the agar had been autoclaved for 15 min at 121 ˚C. The medium was then poured into the Petri dish with the top slightly partially open. Before preparing the Petri dishes with the PDA, the hood was cleaned by spraying it with ethanol. The mouths of the tubes were cleaned both before and after use by the flame of a Bunsen burner. To prevent the production of bubbles, the agar solution was added gently. The Petri dishes were filled halfway with PDA solution, and they were left alone until the agar solution gelled at 25 °C.

The fungal samples were grown in Petri dishes filled with pre-made PDA medium, and the antimould activity of uncoated and surface-coated Fe_2O_3NPs formulations were tested. The surface of the PDA-loaded Petri was covered with 0.5 mL of each of the uncoated and surface-coated Fe_2O_3NPs suspension samples (see Figure 2.13). The PDA-gel plates were left for an hour to absorb the antimould formulation after the dish was tilted to distribute it uniformly. 5 mm discs that had not been impregnated were inserted into the fungus solution tube using tweezers, being careful to wipe up any excess fungus solution from the disc before inserting it. The disc was placed into the PDA-loaded Petri dish after being lightly dampened, and the parafilm M tape was used to close the dish. The samples were kept at 37 °C, and the PDA-gel plate was photographed for several days to track the stage of colony growth in each sample. The growing diameter of the fungus on the PDA-gel plate was calculated using the Image J program and a ruler.

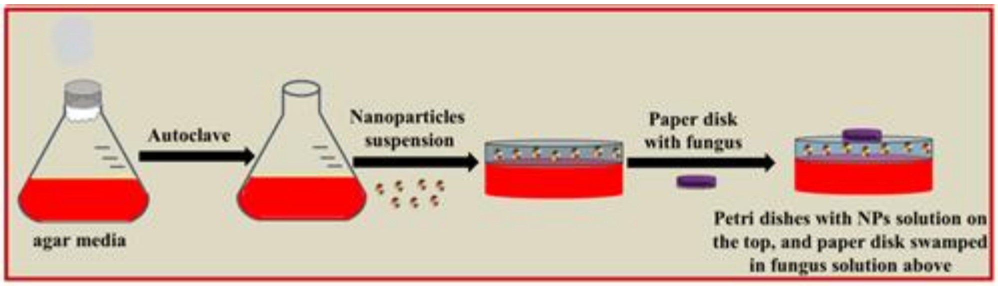

Figure 2.13 Schematic of the method of application of the free and nano-formulated antifungal agents in Fe_2O_3NPs coated with PSS and PAH at various antifungal concentrations to the *Trichoderma* fungus.

3.Results and Discussion

3.1 Characterization of Fe_2O_3NPs

3.1.1 Transmission electron microscopy (TEM)

The size and morphology of synthesized Fe_2O_3NPs were examined by TEM analysis. TEM examination was performed to get clear information about shape, size and structural details. Figure 3.1 and Figure 3.2 shows the TEM images of Fe_2O_3NPs that were produced using the precipitation method and calcined for 4 h at 200 and 500 °C. The average particle diameter of the Fe_2O_3NPs after a 4 h heat treatment was determined to be 48 ± 10 nm at 200 °C Figure 3.1 and 96 ± 7 nm at 500 °C Figure 3.2. It is evident that nanoparticles are primarily found in nature as granules with small and big spherical shaped particles. The calcination temperature utilized in the synthesis of Fe_2O_3NPs has a significant impact on the nanoparticle size. The TEM images of Fe_2O_3NPs were proved that the particle size increased with the increase of the calcination temperature Figure 3.1 and Figure 3.2

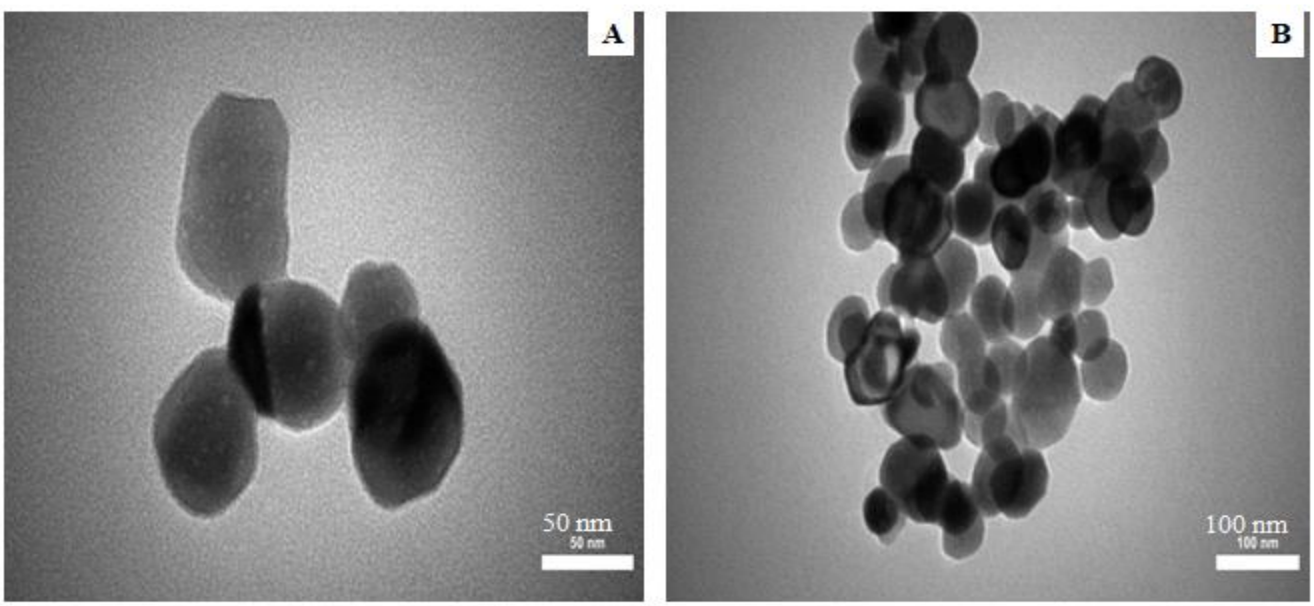

Figure 3.1 TEM images of Fe_2O_3NPs at lower and higher magnifications prepared with different calcination temperatures. **A,B** calcined at 200 °C.

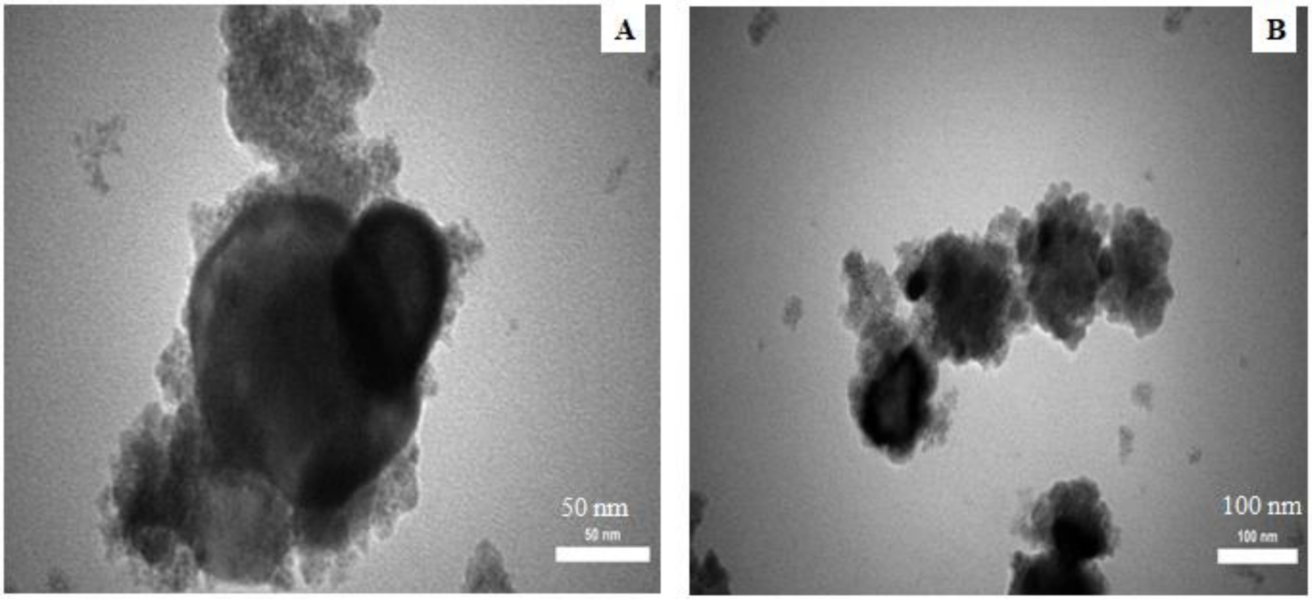

Figure 3.2 TEM images of Fe_2O_3NPs at lower and higher magnifications prepared with different calcination temperatures. **A,B** calcined at 500 °C.

3.1.2 Fourier transform infrared (FTIR)

FTIR spectroscopy was used to further confirm the production of Fe_2O_3 nanoparticles. Figure 3.3 displays FTIR spectra of Fe_2O_3 uncalcined and calcined at 200 and 500 °C formed by using the precipitation method. The significant absorption peaks at 443 and 556 cm^{-1} for the uncalcined Fe_2O_3 nanoparticles product can be attributed to the vibrations of the Fe-O band [142, 143].

The very broad absorption band centered at 3398 cm^{-1} and reaching peak at 1638 cm^{-1} is attributed to the stretching and bending vibrations of the hydroxyl groups and/or water molecules, respectively [144].

The results show that the products were prepared in an aqueous solution, which resulted in the presence of structural hydroxyl groups as well as a minor quantity of absorbed water on their surface. FTIR spectrum analyses of pure Fe_2O_3 nanoparticles calcined at 200 and 500 °C generated by precipitation method displays the reduction of bands related to the hydroxyl group. It was also observed the appearance of two bands at 434 and 527 cm^{-1} that can be related to the Fe–O bond of Fe_2O_3NPs [145].

The characteristic peak at 434 and 527 cm^{-1} becomes very strong for Fe_2O_3 nanoparticles calcined at 200 and 500 °C, indicating the creation of the stretching mode of Fe_2O_3.

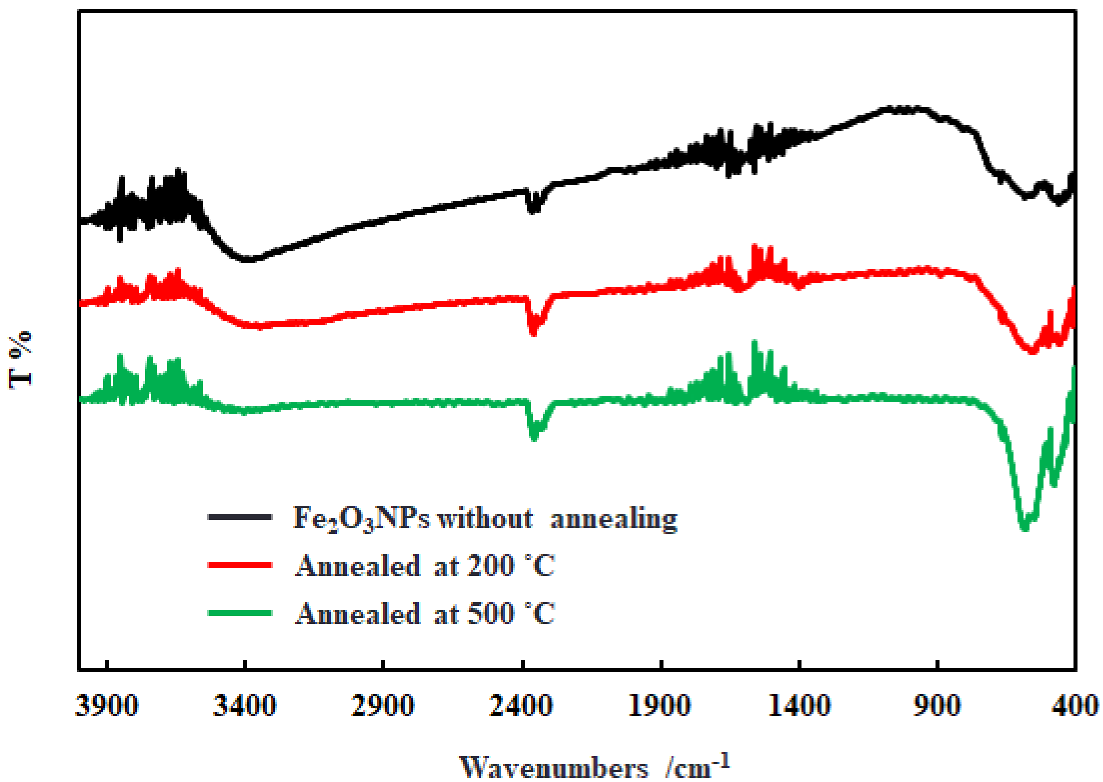

Figure 3.3 FTIR spectrum of Fe_2O_3 uncalcined and calcined at 200 and 500 °C produced by precipitation method.

3.1.3 BET-Surface Area Measurements Instrument

The BET technique was used to measure the surface areas of Fe_2O_3NPs formed from Fe_2O_3 at different temperatures. Note that the Fe_2O_3NPs surface area declined as the calcination temperature increased from 199 m^2 g^{-1} at 80 °C to 27 m^2 g^{-1} at 500 °C as shown in Figure 3.4.

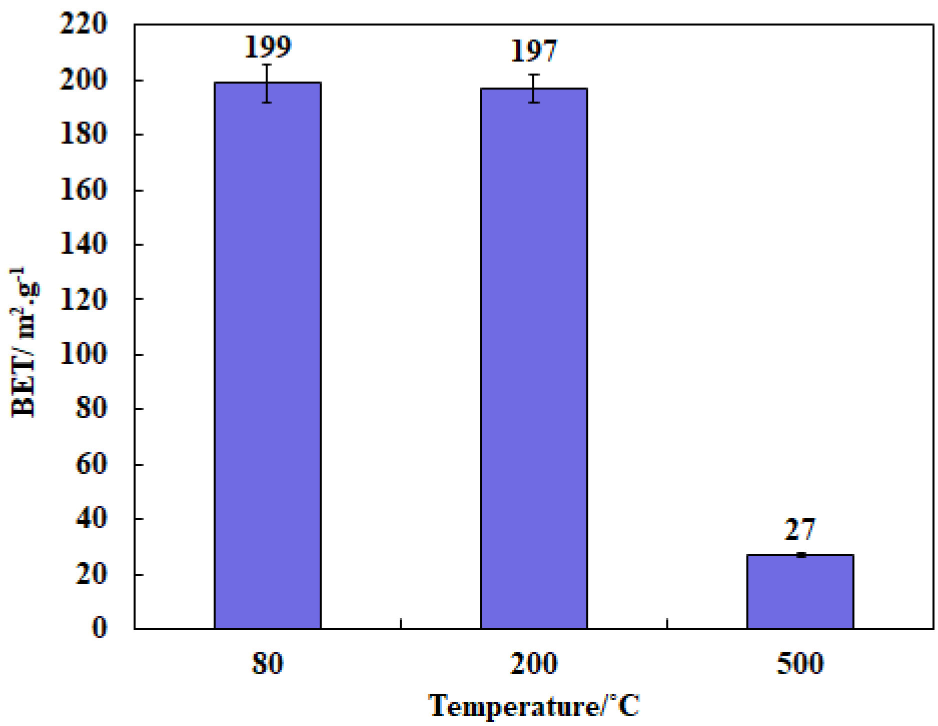

Figure 3.4 The impact of the calcination temperature during the Fe_2O_3NPs synthesis on the BET surface area of Fe_2O_3NPs from 80 to 500 ^oC.

3.1.4 Dynamic Light Scattering (DLS) and Zeta potential

To study the formation of each polyelectrolyte layer deposited on the Fe_2O_3NPs, the zeta potential and hydrodynamic diameter experiments were measured by DLS. Was coated two additional layers of PSS and PAH to cover Fe_2O_3NPs that were 70 nm at 200 °C and 95 nm at 500 °C using the methods described below [5, 87]. Figure 3.5 and Figure 3.7 displays that the coated Fe_2O_3NPs size increases after each additional polyelectrolyte coating because of partial aggregation. The variation of zeta potential with the polyelectrolyte layer number for PSS and PAH coatings are presented in Figure 3.5 and Figure 3.7. The zeta potential of the Fe_2O_3NPs changed from a positive charge to a negative charge for Fe_2O_3NPs/PSS due to PSS single layer being a negatively charged. An additional PAH coating produced positively charged Fe_2O_3NPs/PSS/PAH with zeta potentials of +42 mV Figure 3.6 and +31 mV Figure 3.8. Adding the polyelectrolyte layer with the opposing charge causes the particle surface charge to alternate, as expected.

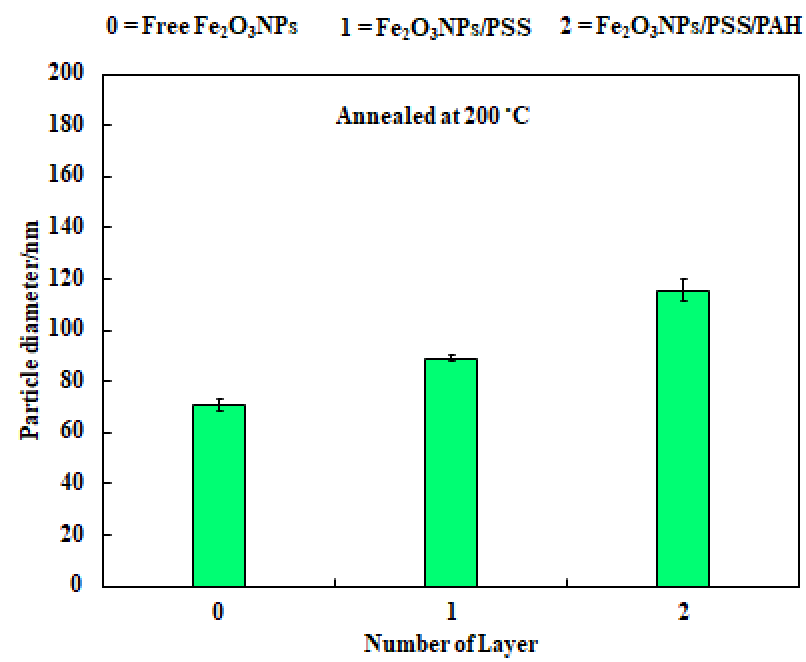

Figure 3.5 The particle size of bare-and polymer-modified Fe_2O_3NPs calcined at 200 as a function of PSS and PAH layers. The free Fe_2O_3NPs are represented by the zero layers. PSS deposition is represented by layer number 1 and PAH deposition is represented by layer number 2.

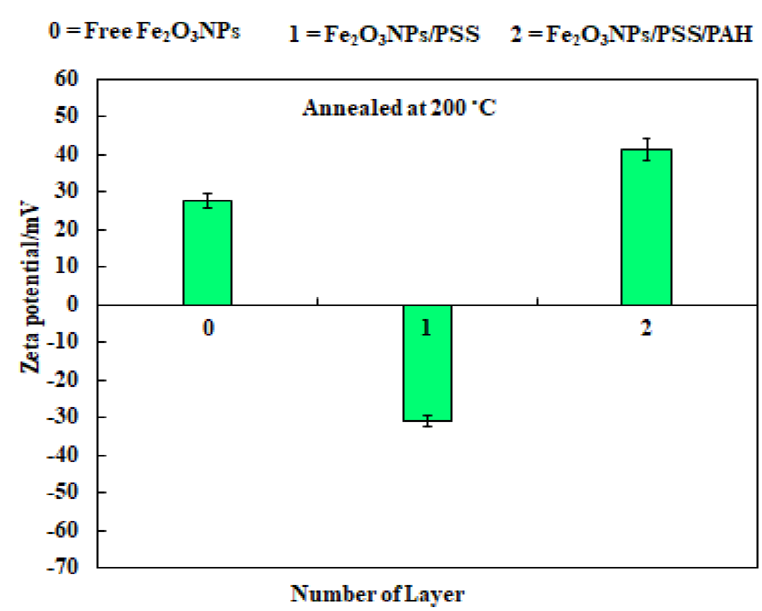

Figure 3.6 The zeta potential of bare-and polymer-modified Fe_2O_3NPs calcined at 200 as a function of PSS and PAH layers. The free Fe_2O_3NPs are represented by the zero layers.

PSS deposition is represented by layer number 1 and PAH deposition is represented by layer number 2.

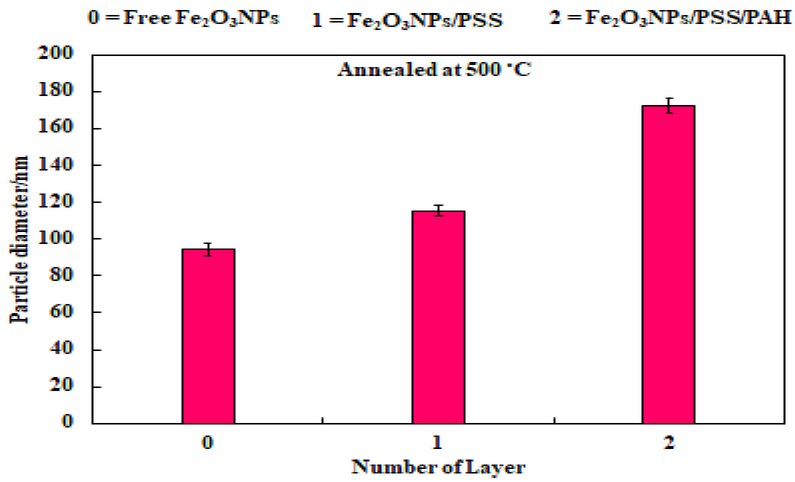

Figure 3.7 The particle size of bare-and polymer-modified Fe_2O_3NPs calcined at 500 °C as a function of PSS and PAH layers. The free Fe_2O_3NPs are represented by the zero layers. PSS deposition is represented by layer number 1 and PAH deposition is represented by layer number 2.

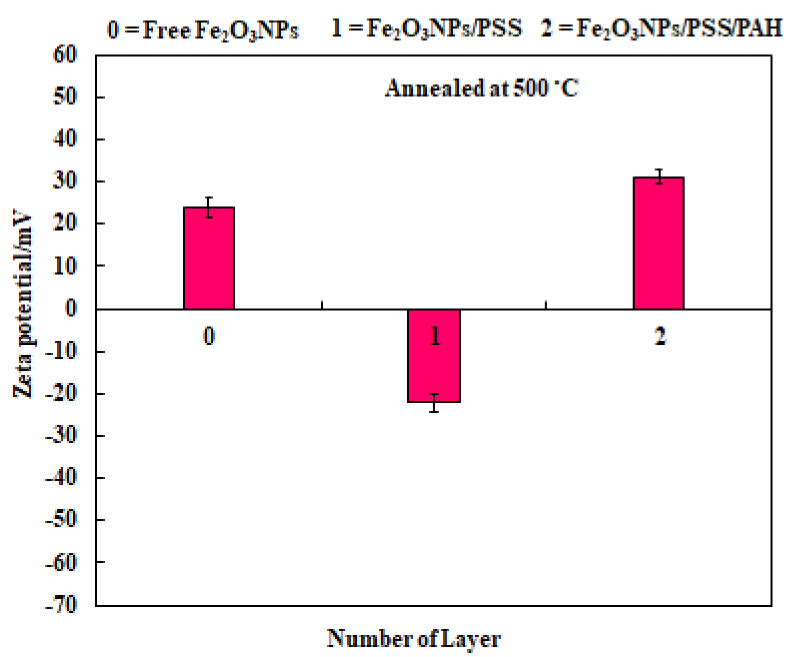

Figure 3.8 The zate potential of bare-and polymer-modified Fe_2O_3NPs calcined at 500 °C as a function of PSS and PAH layers. The free Fe_2O_3NPs are represented by the zero

layers. PSS deposition is represented by layer number 1 and PAH deposition is represented by layer number 2.

DLS measurements were used to examine how each polyelectrolyte layer that was deposited on the Fe_2O_3NPs formed. To cover Fe_2O_3NPs that were 70 nm at 200 °C and 95 nm at 500 °C, it was coated two additional layers of PSS and PAH using the methods mentioned above [5, 87]. The results in Figure 3.(9,11,13) and Figure 3.(15,17,19) show that the size of the coated Fe_2O_3NPs increases as more polyelectrolytes are added due to partial aggregation. Figure 3.(10,12,14) and Figure 3.(16,18,20) show how the zeta potential varies with the number of polyelectrolyte layers for coatings consisting of PSS and PAH, respectively. It was found that the zeta potential of the Fe_2O_3NPs changed from a positive charge to a negative charge for Fe_2O_3NPs/PSS Figure 3.12 and Figure 3.18 because of PSS single layer being a negatively charged. A second coating with the PAH layer resulted in positively charged for Fe_2O_3NPs/PSS/PAH with zeta potentials of +42 mV Figure 3.14 and +33.5 mV Figure 3.20. The expected result of adding the polyelectrolyte layer with the opposing charge is that the particle surface charge will alternate.

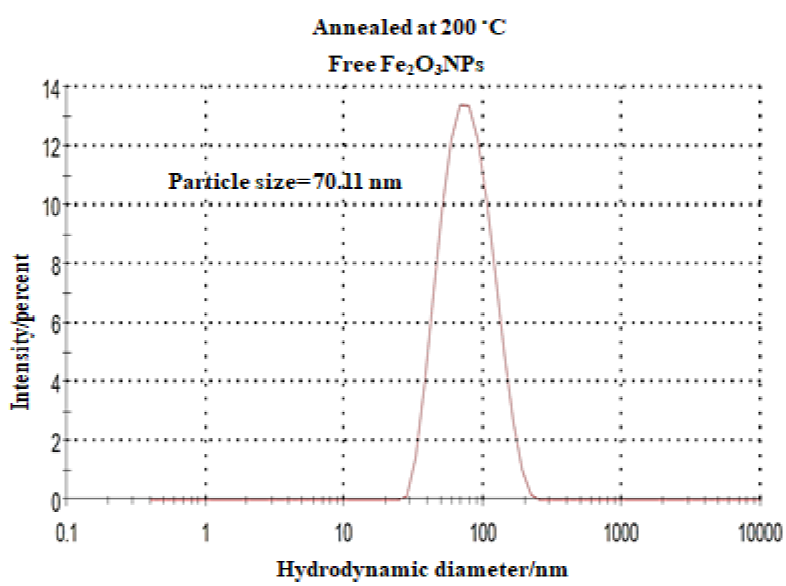

Fig. 3.9 The particle size of Fe_2O_3NPs calcined at 200 °C.

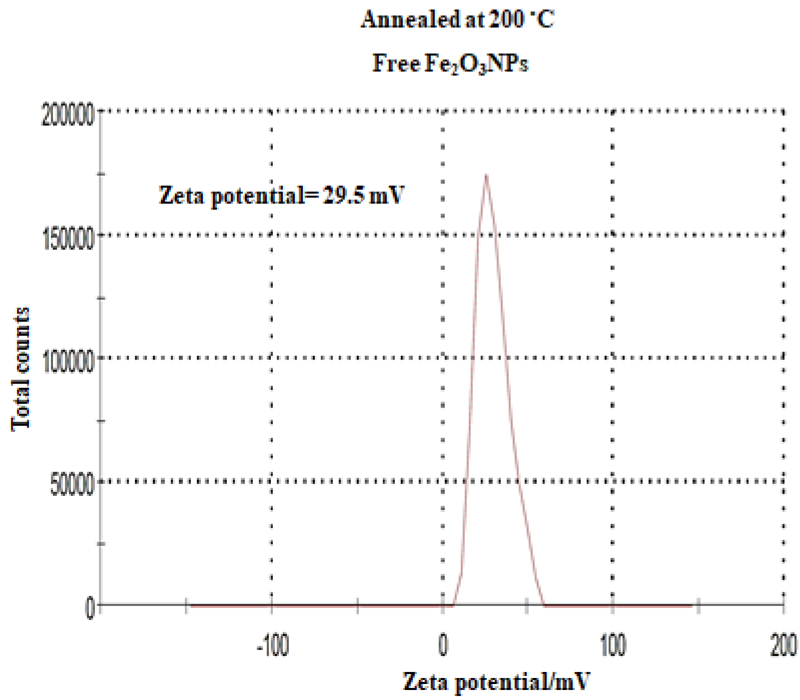

Fig. 3.10 The zeta potential of Fe_2O_3NPs calcined at 200 °C.

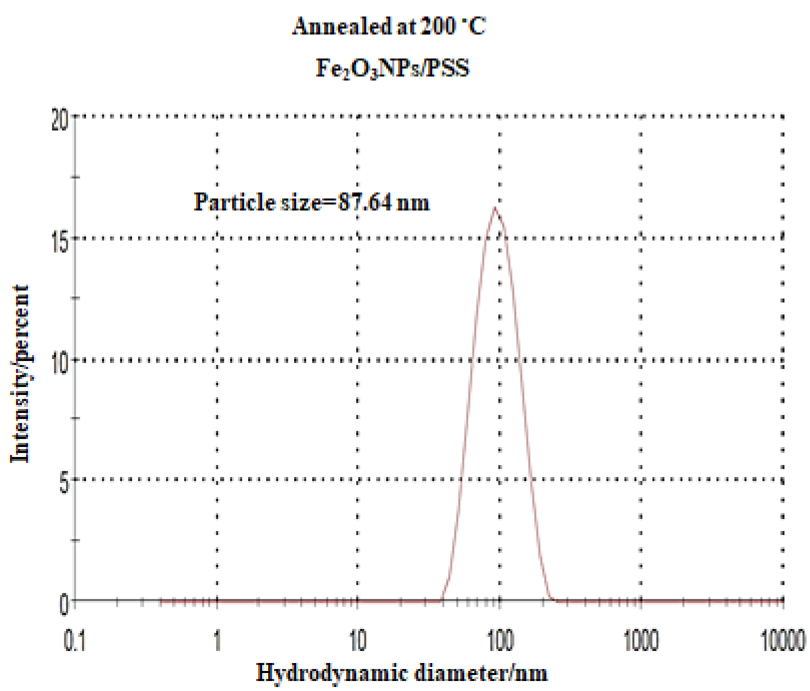

Figure 3.11 The particle size of polymer-modified Fe_2O_3NPs calcined at 200 °C.

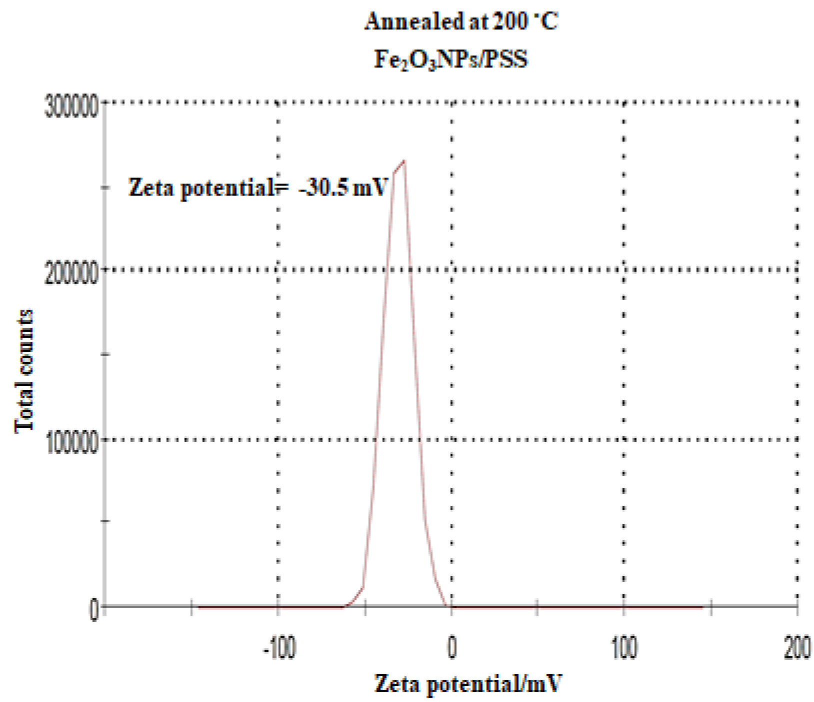

Figure 3.12 The zeta potential of polymer-modified Fe_2O_3NPs calcined at 200 °C.

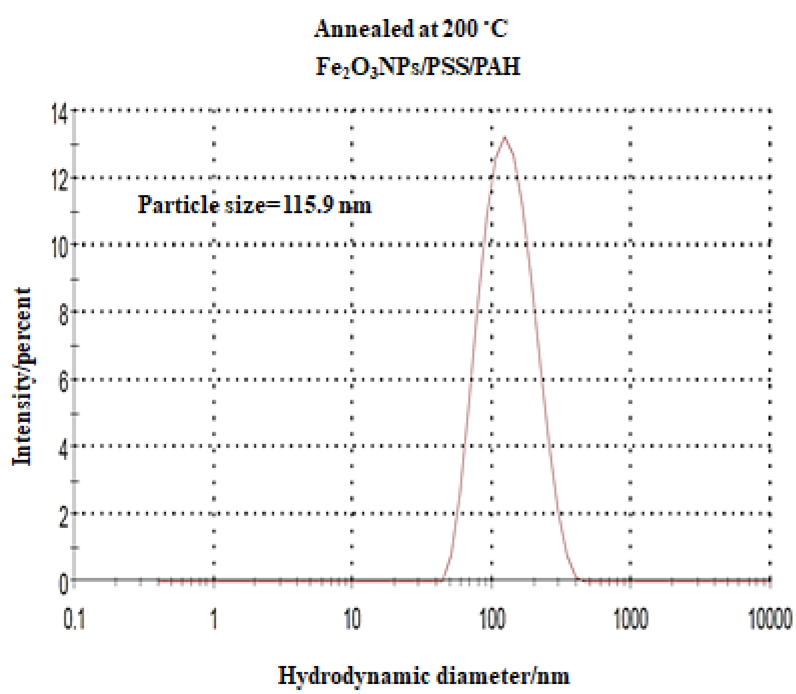

Figure 3.13 The particle size of polymer-modified Fe_2O_3NPs calcined at 200 °C.

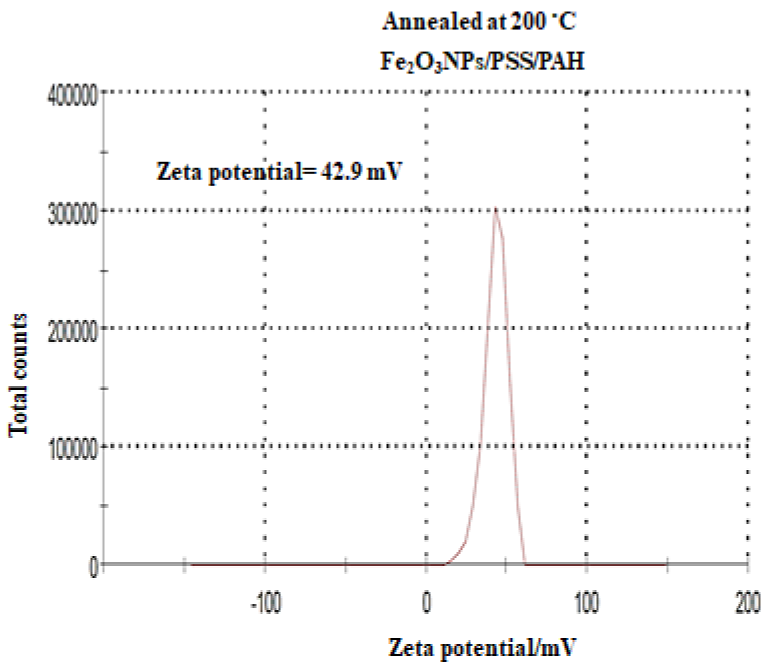

Figure 3.14 The zeta potential of polymer-modified Fe_2O_3NPs calcined at 200 °C.

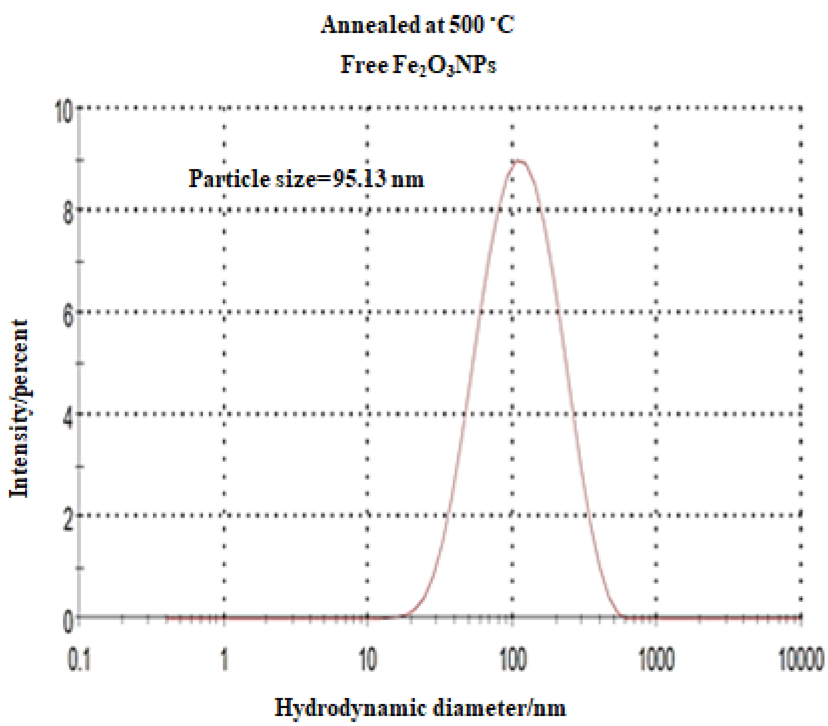

Figure 3.15 The particle size of Fe_2O_3NPs calcined at 500 °C.

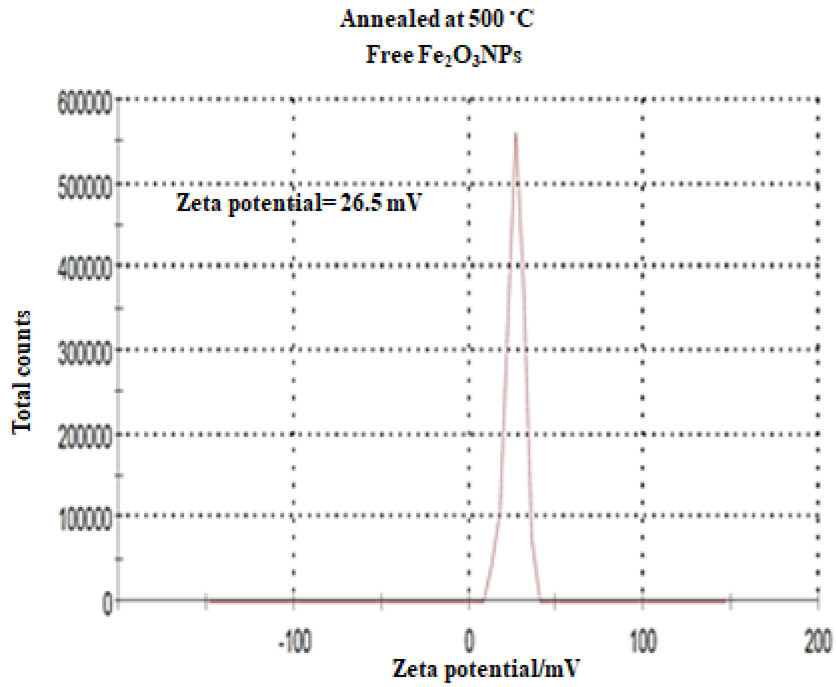

Figure 3.16 The zeta potential of Fe_2O_3NPs calcined at 500 °C

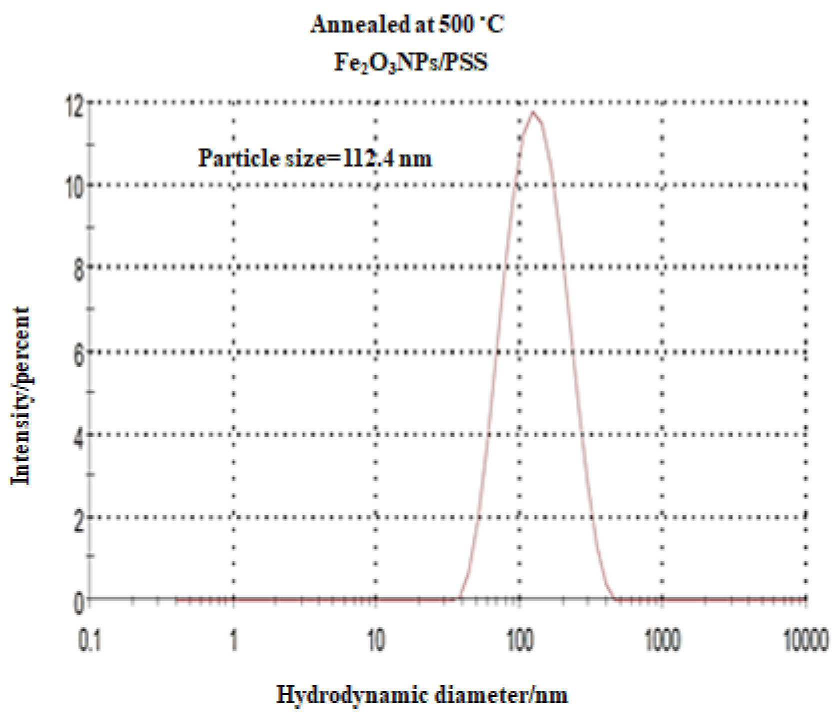

Figure 3.17 The particle size of polymer-modified Fe_2O_3NPs calcined at 500 °C

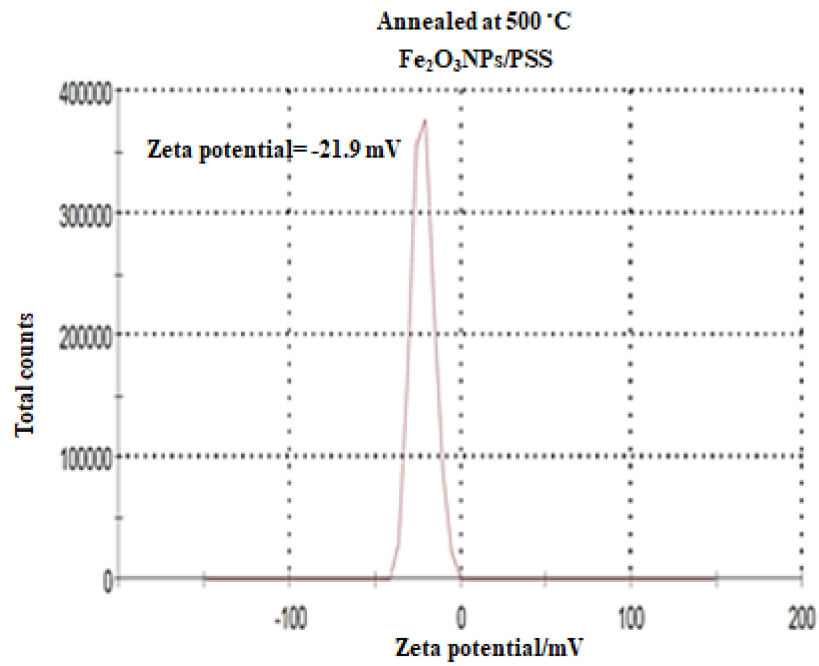

Figure 3.18 The zeta potential of polymer-modified Fe_2O_3NPs calcined at 500 °C

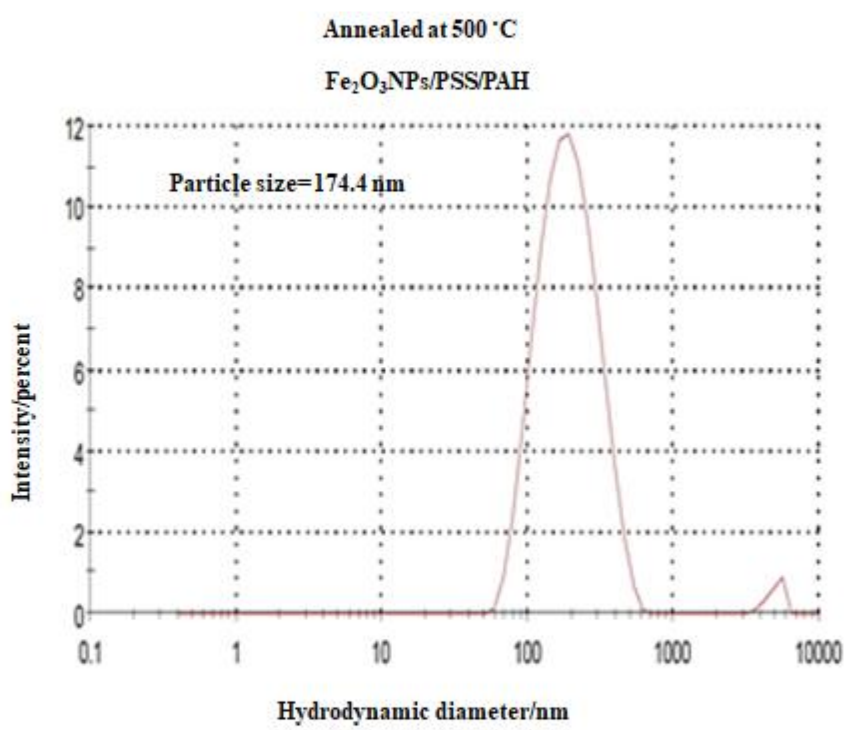

Figure 3.19 The particle size of polymer-modified Fe_2O_3NPs calcined at 500 °C

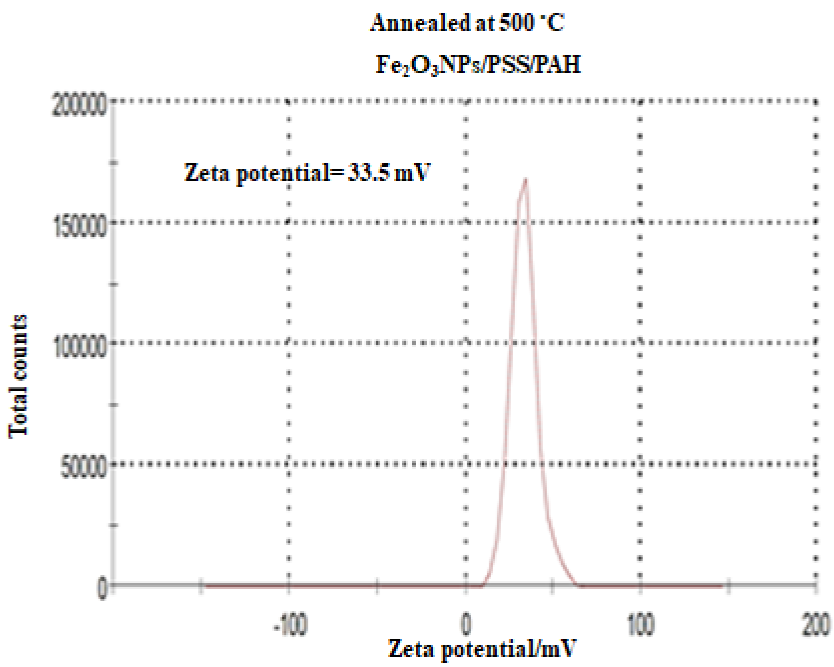

Figure 3.20 The zeta potential of polymer-modified Fe_2O_3NPs calcined at 500 °C

3.1.5 Scanning electron microscopy (SEM)

SEM analysis was also used to examine the surface morphologies of the prepared samples of Fe_2O_3NPs at 200 and 500 °C. Figure 3.21A,B and Figure 3.22A,B displays the average size of the produced iron oxide nanoparticles as a function of the calcination temperatures. It was discovered that the form of every single nanoparticle is spherical.

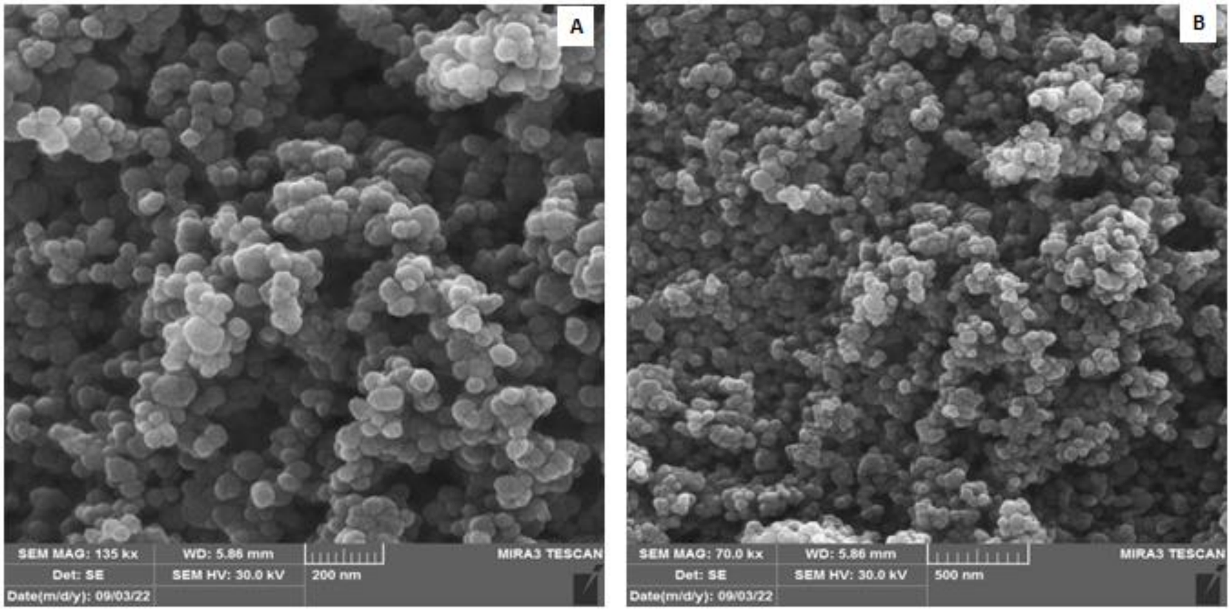

Figure 3.21 SEM images of the Fe_2O_3NPs: (A and B) annealed sample at 200 °C at different magnifications.

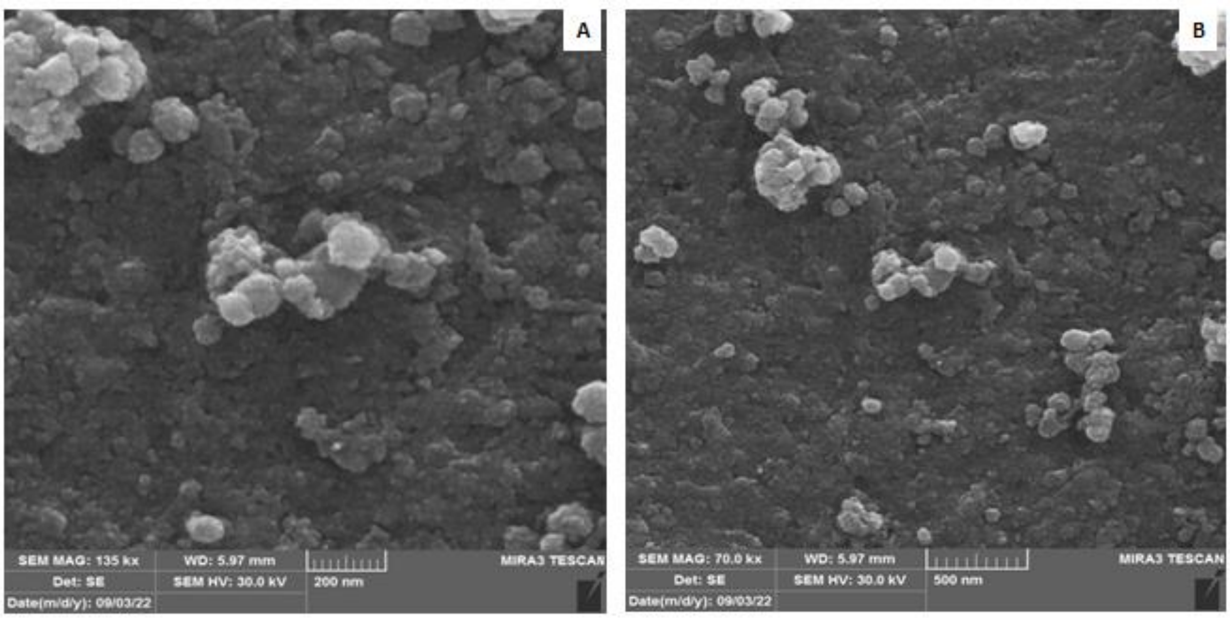

Figure 3.22 SEM images of the Fe_2O_3NPs: (A and B) annealed sample at 500 °C at different magnifications.

3.1.6 X-ray diffraction(XRD)

The results also show that when the calcination temperature is increased from 200 to 500 °C, the average particle diameter of Fe_2O_3NPs increases from 35 ± 8 nm to 92 ± 5 nm Figure 3.23 to Figure 3.27. The crystalline sizes were determined using X-ray diffraction (XRD). The X-ray diffraction patterns of the Fe_2O_3NPs powder are displayed in Figure 3.23 to Figure 3.25. The XRD pattern of the sample prior to annealing is shown in Figure 3.23 and the XRD pattern after heat treatment is shown in Figure 3.24 and Figure 3.25.

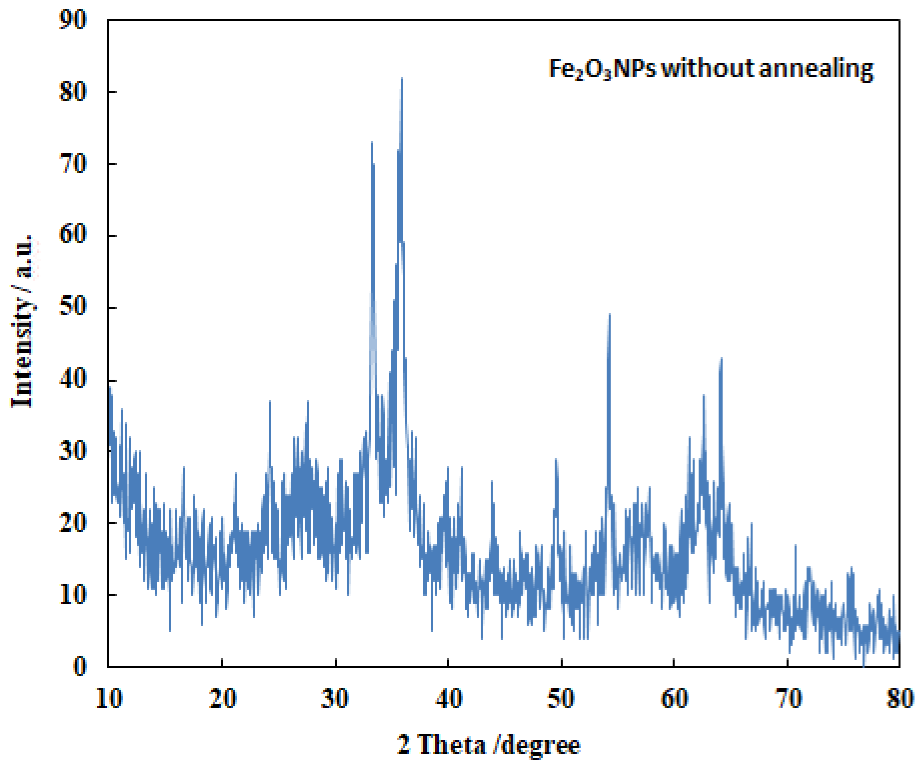

Figure 3.23 XRD pattern of Fe_2O_3NPs uncalcined

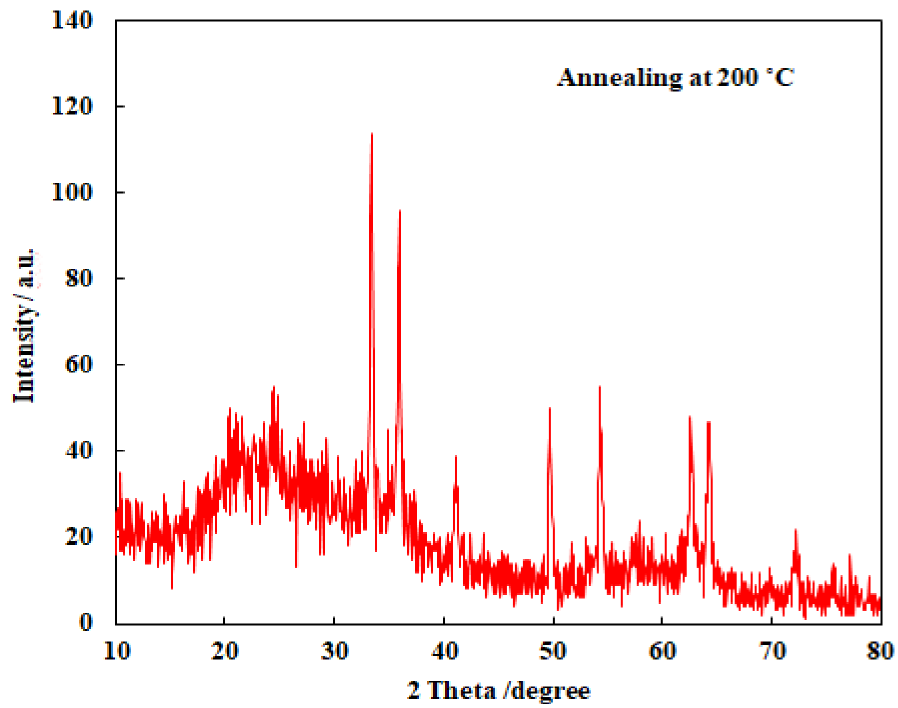

Figure 3.24 XRD pattern of Fe_2O_3NPs calcined at 200 °C

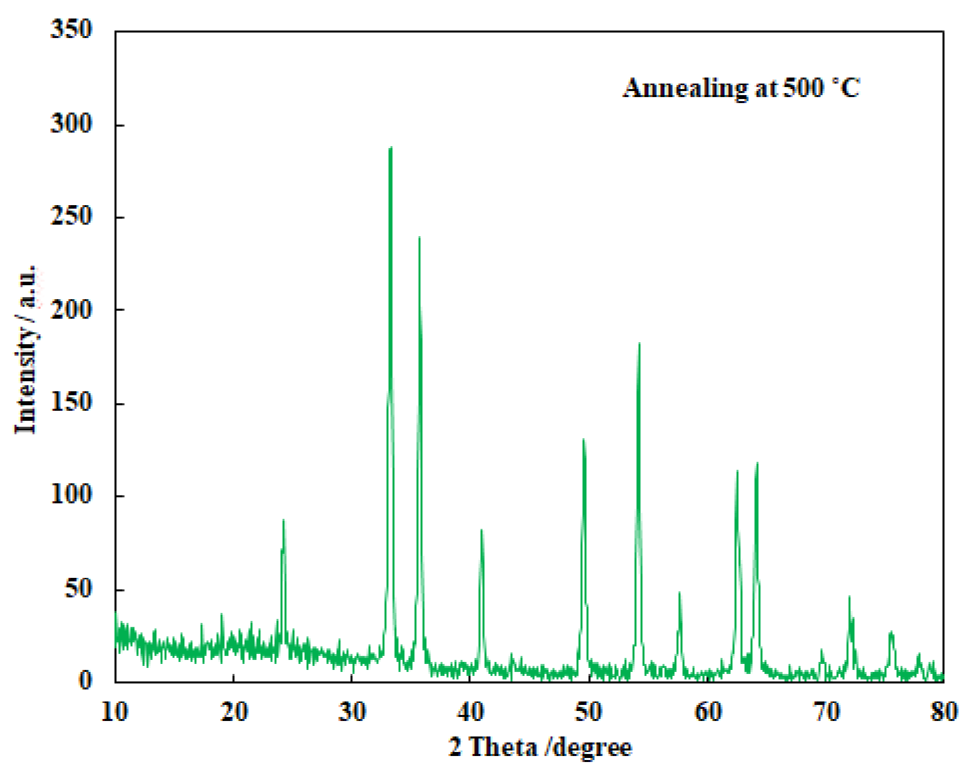

Figure 3.25 XRD pattern of Fe_2O_3NPs calcined at 500 °C.

The XRD data in Figure 3.23 to Figure 3.25 show that the diffraction peak's intensity and half-height width gradually decrease when the calcination temperature is increased and this leads to an increase in crystalline size. The Scherrer equation was used to determine the average crystallite size (D) of Fe_2O_3NPs, $D=K\lambda/\beta\cos\theta$, K is a dimensionless shape constant taken as 0.94, 2θ is the diffraction angle, λ is the wavelength of the X-ray radiation (CuKα = 0.15406 nm), and β is the full width at half-maximum (FWHM) of the diffraction peak. The range of average crystallite sizes found in the XRD data was 4 to 16 nm. As a result, it was found that changing the calcination temperature caused a change in the crystallite size of pure Fe_2O_3NPs.

3.1.7 Energy dispersive X-ray analysis (EDX)

In order to confirm the elemental composition of the produced Fe_2O_3NPs, an Energy Dispersive X-ray Diffraction (EDX) examination was performed. The EDX data in Figure 3.26 and Figure 3.27 confirm the presence of iron and oxygen signals in the Fe_2O_3NPs sample.

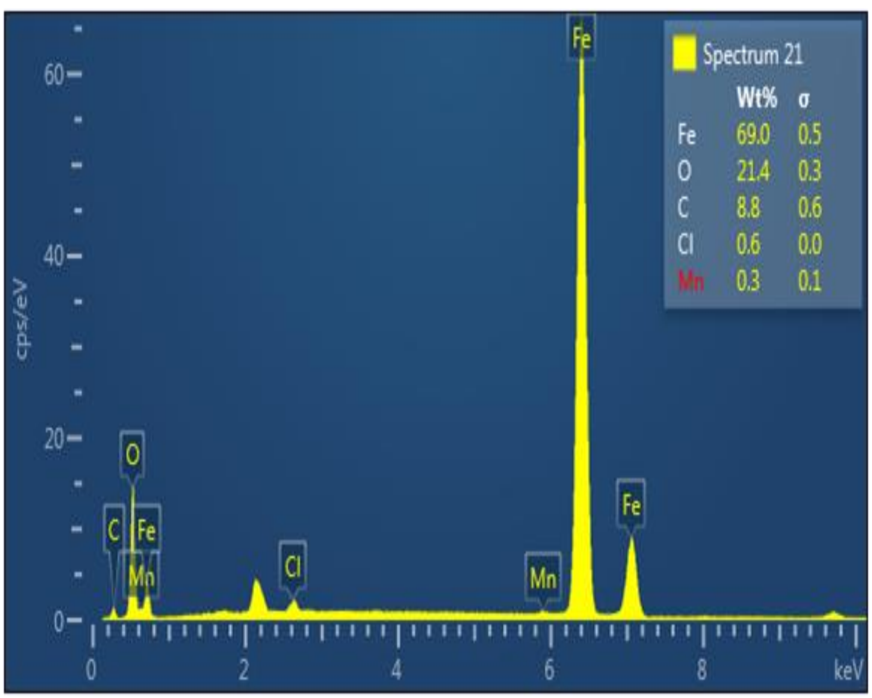

Figure 3.26 EDX spectra of the as-synthesized Fe_2O_3NPs prepared by direct precipitation method. calcined at 200 °C.

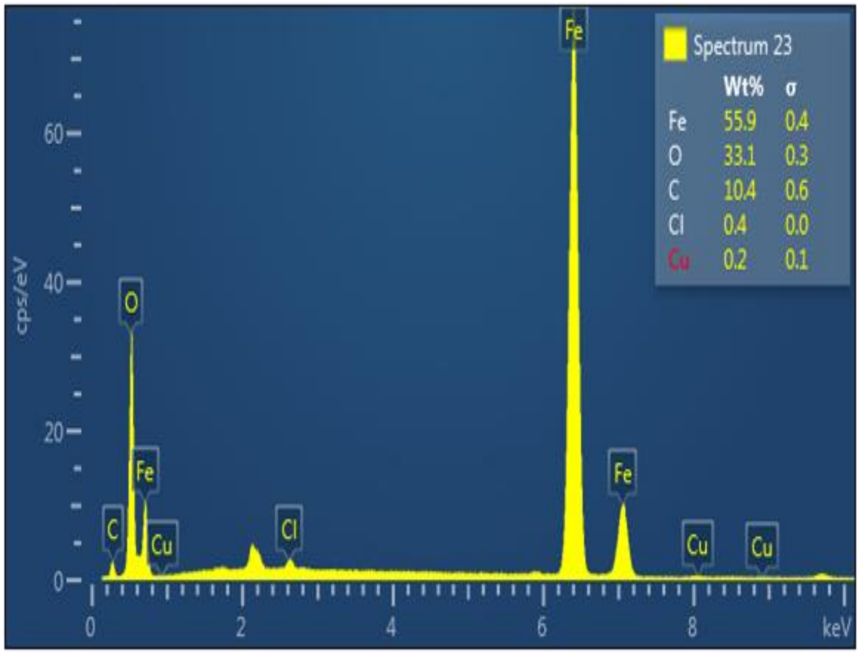

Figure 3.27 EDX spectra of the as-synthesized Fe_2O_3NPs prepared by direct precipitation method. calcined at 500 °C.

3.2 FSS Dye Adsorption and Photocatalytic Studies

3.2.1 The Effect of the Amount of Fe_2O_3NPs on FSS Dye Adsorption

The photocatalytic and adsorption properties of Fe_2O_3NPs toward FSS dye was investigated under UV irradiation as well as in dark conditions. Different Fe_2O_3NPs adsorbent amounts including 0.05 g, 0.1 g, 0.15 g, 0.2 g, 0.25 g and 0.3 g were utilized to evaluate the effects of nanoparticle amounts calcined at 200 and 500 °C in the removal of FSS dye. The works were carried out in 100 cm^3 solution of 10 mg L^{-1} initial FSS concentration at room temperature. The percentage of FSS dye adsorption and photodegradation efficiency increased with increasing doses of Fe_2O_3NPs as illustrated in Figure 3.28 and Figure 3.29. This was explained by the fact that as the amount of adsorbent increases, there is a higher chance that the FSS dye will come into touch with the available active sites of the Fe_2O_3NPs. As an anionic dye model, FSS dye was used in the present research to evaluate how well Fe_2O_3NPs removed FSS dyes in both dark and light conditions. This result could be attributed to the anionic dye being electrostatically attracted to cationic Fe_2O_3NPs, which causes the FSS dye to be absorbed by Fe_2O_3NPs. After adsorption of 0.05 g of Fe_2O_3NPs with 10 mg L^{-1} of FSS dye, there was a noticeable difference in FSS dye removal in dark Figure 3.28(C) and Figure 3.29(C) and UV light conditions Figure 3.28(D) and Figure 3.29(D) because of the photoactivity of the Fe_2O_3NPs. FSS dye quickly adsorbs to Fe_2O_3NPs at first, but the adsorption activity gradually slows and reaches equilibrium after 10 minutes under UV light and darkness, as illustrated in Figure 3.28 and Figure 3.29. The rate of adsorption varies quickly since all of the adsorbent sites are initially empty. The decrease in the number of unoccupied adsorbent sites and the dye concentration over time cause the adsorption rate to become low. The decreased rate of adsorption indicates that FSS probably formed a monolayer on the surface of the Fe_2O_3NPs. As a consequence, once equilibrium is reached, there aren't enough free active sites, therefore more absorption is required. The removal percentage of FSS dye that was adsorbed by Fe_2O_3NPs calcined at 200 and 500 °C in both light and dark was reported. Figure 3.28 and Figure 3.29 show that the removal percentage of FSS dyes using Fe_2O_3NPs under UV light is higher than that in the dark at the same conditions. One probable description is that aqueous suspensions of Fe_2O_3NPs under UV light can produce ROS like $O_2^{\bullet-}$ and H_2O_2 [87]. The decolorization of dyes is widely discussed in the literature review. The hydroxyl radicals are generated in a solution that acts as an oxidant, which is formed on Fe_2O_3NPs. Furthermore, when water molecules on the surface of Fe_2O_3NPs interact with holes ($h^+_{(VB)}$), hydroxyl ion radicals are generated. Therefore, hydroxyl ion radicals destroy the FSS dye [29, 38].

The results represented in Figure 3.29 show that the Fe_2O_3NPs calcined at 500 °C have lower adsorption and photocatalytic activity on FSS dye when compared to the Fe_2O_3NPs calcined at 200 °C Figure 3.28 . One possible explanation is that the increase of the calcination temperature leads to an increase of size of Fe_2O_3NPs. Thus, the smallest size was obtained at the lowest calcination temperature (200 °C). It was also found that the Fe_2O_3NPs surface area increased as the calcination temperature declined as described below.

Adsorption and photocatalytic equations

$$\% R = \frac{C_0 - C_t}{C_0} \times 100\% \quad \dots\dots\dots 1$$

$$PDE = \frac{C_0 - C_t}{C_0} \times 100\% \quad \dots\dots\dots 2$$

$$Q_t = \frac{(C_0 - C_t)\, V}{m} \quad \dots\dots\dots 3$$

$$Q_e = \frac{(C_0 - C_e)\, V}{m} \dots\dots\dots 4$$

Where C_0 is the initial concentration of FSS ($mg.dm^{-3}$) before adsorption

C_t - is the FSS concentration after adsorption at a given time t

C_e - concentration of FSS in solution at equilibrium time ($mg.dm^{-3}$)

V - is the volume of FSS solution (dm^3)

m - is the weight of bare and surface-coated Fe_2O_3NPs (g).

PDE- The photodegradation efficiency of FSS dye.

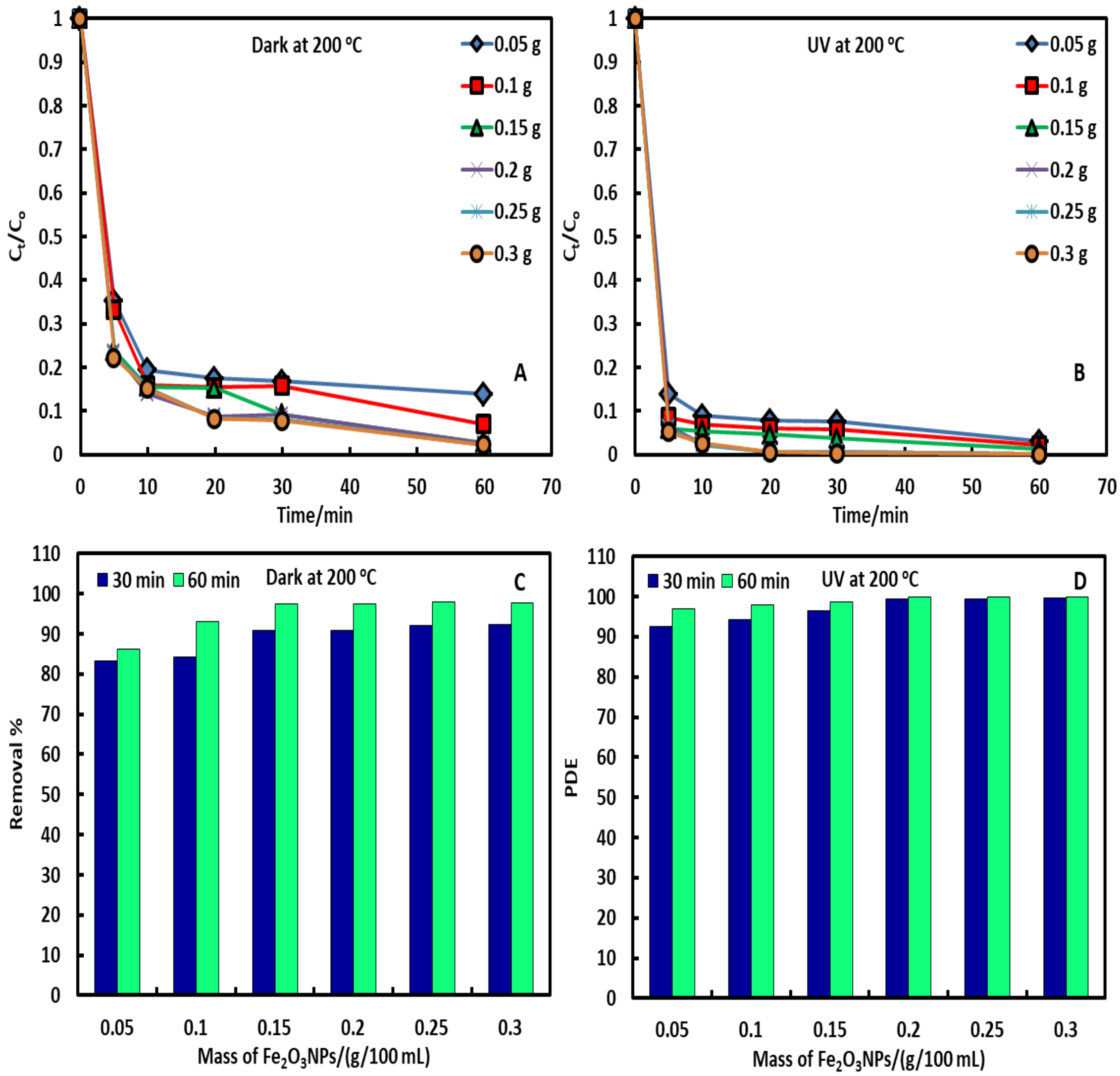

Figure 3.28 The impact of Fe_2O_3NPs amount calcined at 200 °C on the removal percentage and photodegradation efficiency of FSS dye under (**A** and **C**) dark conditions and (**B** and **D**) UV light.

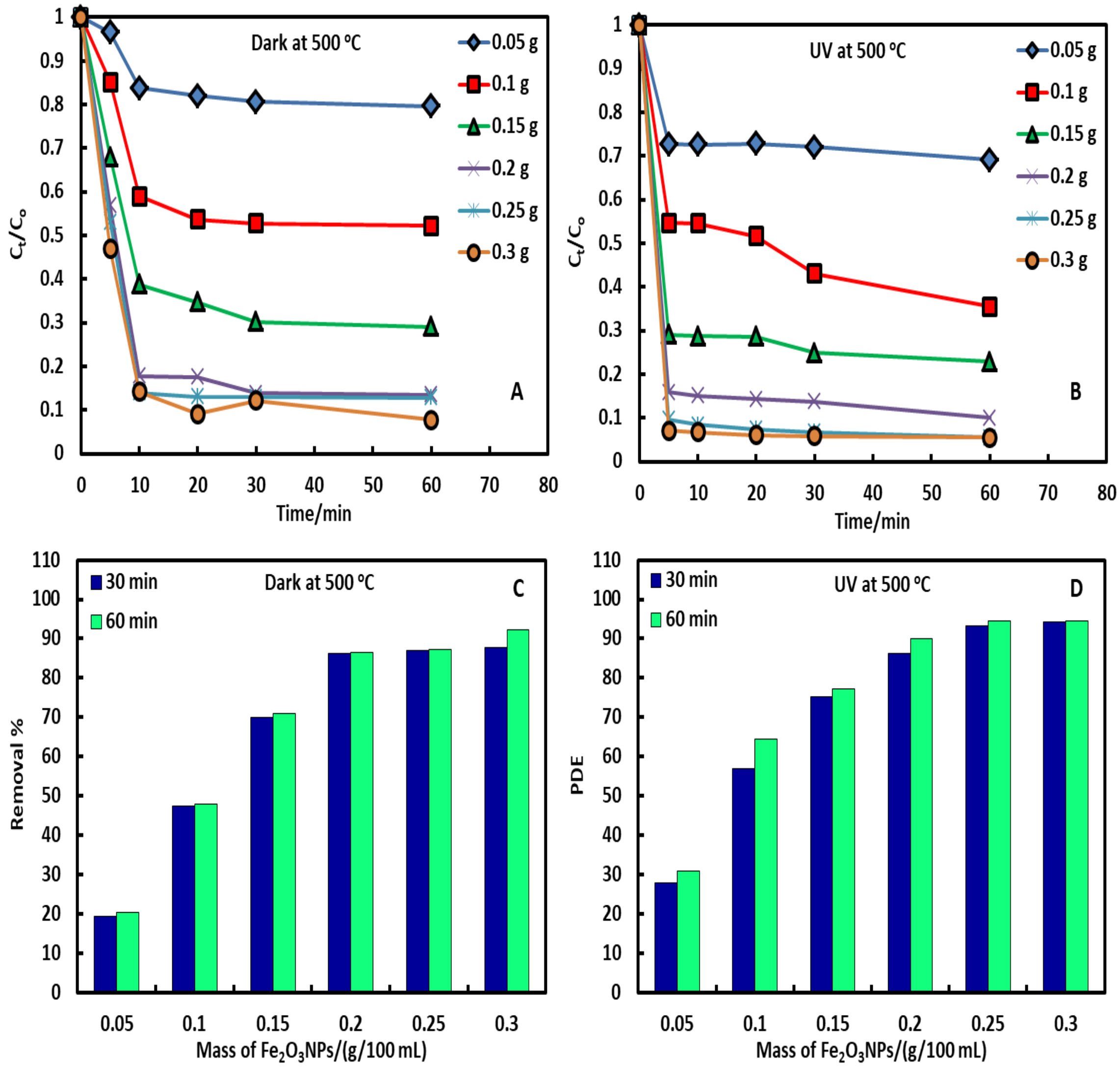

Figure 3.29 The impact of Fe_2O_3NPs dose calcined at 500 °C on the removal percentage and photodegradation efficiency of FSS dye under (**A** and **C**) dark conditions and (**B** and **D**) UV light.

3.2.2 Effect of Initial FSS Dye Concentration

One of the most significant aspects affecting the adsorption process may be the initial dye concentration since it indirectly impacts the effectiveness of dye removal by lowering or raising the number of binding sites on the adsorbent surface. The effectiveness of dye removal and the maximum amount of dye bound in equilibrium in such systems of water treatment are strongly related to the initial dye concentration [146].

By changing the initial concentration of the FSS dye over a wide range (5 - 50 mg L^{-1}), the impact of the initial concentration on the removal percentage and photodegradation efficiency was examined. Adsorption and photocatalytic tests were conducted at various initial FSS dye concentrations of FSS dye at a fixed pH and 0.2 g of Fe_2O_3NPs. The results in Figure 3.30 and Figure 3.31 show that the removal percentage and photodegradation efficiency of FSS dye decreased with increasing the initial FSS dye concentration.

The saturation of adsorption sites on the adsorbent surface can explain for this phenomenon. In this situation, as the initial FSS dye concentration increases, so does the ability of the adsorbent, which is because of the high mass transfer driving force at high initial FSS concentrations. The initial FSS dye concentration of the solute drives the adsorption process by favoring mass transfer and diffusion from the solution (which contains a higher amount of FSS dye) to the adsorbent's free surface [146]. At higher initial FSS dye concentrations, the total free adsorption sites are limited, which could result in a decrease in the removal percentage of FSS dye. The rise at higher initial FSS dye concentrations could be attributed to increased driving forces. On the other hand, because the ratio of active sites to FSS dye molecules can be high at low concentrations, all molecules can interact with the adsorbent and are nearly immediately removed from the solution [146].

The adsorption and photocatalytic activity of bare Fe_2O_3NPs toward various concentrations was also examined of FSS dye upon illumination with UV light compared with that under dark conditions to assess the influence of the oxidative stress owing to the reactive oxygen species (ROS). The data in Figure 3.30 and Figure 3.31 show that there was a remarkable difference between the removal percentage of FSS dye in dark conditions Figure 3.30(C) and that under UV light Figure 3.3(D) because of the photoactivity of the Fe_2O_3NPs. One possible explanation is that under UV irradiation, electrons in the VB may be stimulated to the CB of the oxide, with the concomitant creation of the same quantity of holes in the VB, resulting in the creation of an electron-hole pair. Redox reactions with organics can then result from further charge separation and the migration of the created charge carriers toward the surface of the catalyst. Direct oxidation of the FSS dye to reactive intermediates is possible due to the high oxidative potential of the hole (h^+) (VB) in the Fe_2O_3NPs.

Another way that water might decompose is to produce hydroxyl radicals, which are extremely reactive. On the other hand, a more effective reaction will occur when electrons interact with dissolved oxygen molecules to form superoxide radical anions, which then protonate to become hydroperoxyl radicals ($HO_2^{\bullet}$) and lastly $OH^{\bullet}$ radicals [145].

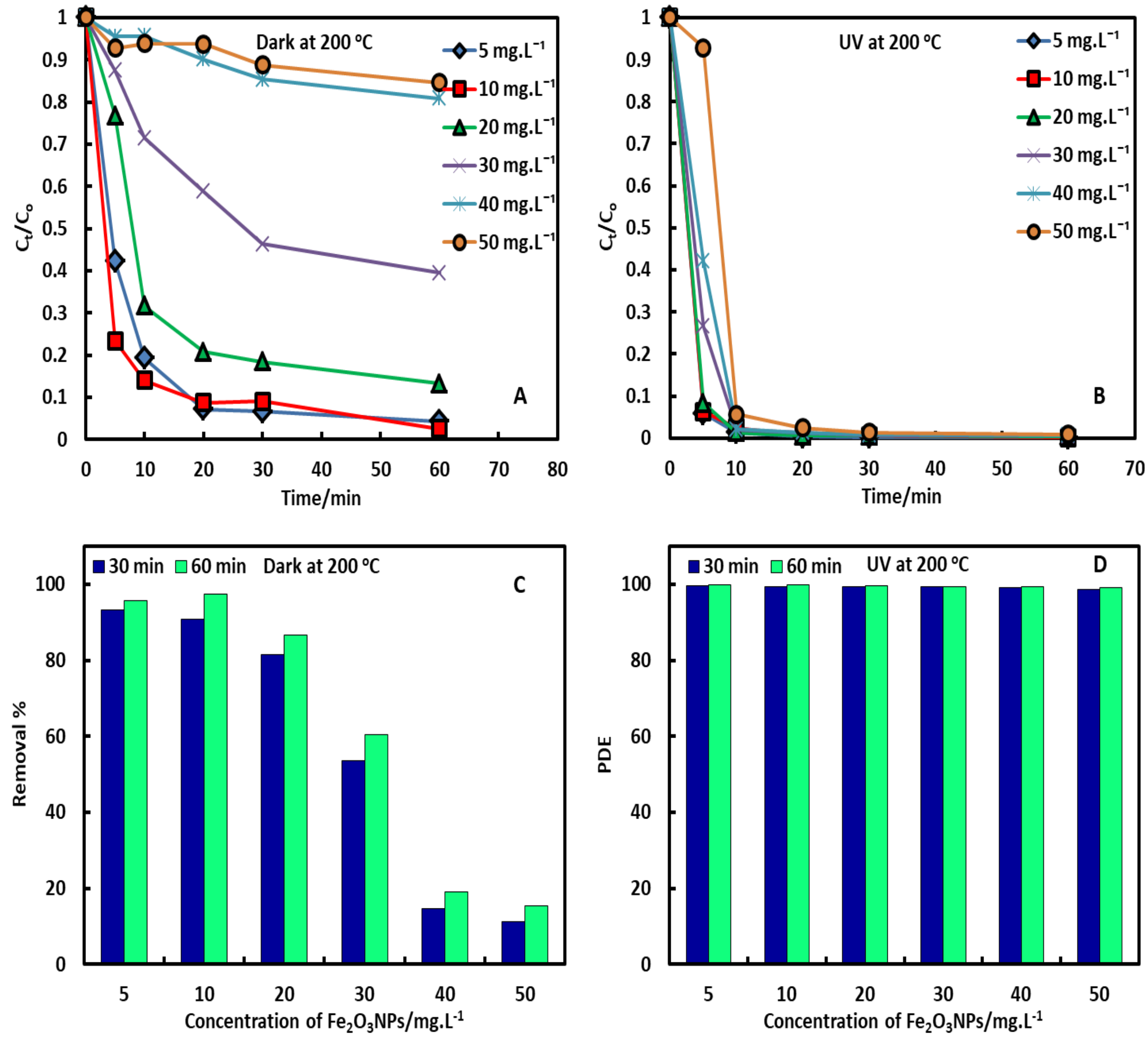

Figure 3.30 Effect of initial concentration on the removal percentage and photodegradation efficiency of FSS dye under (**A** and **C**) dark conditions and (**B** and **D**) UV light in the presence of Fe_2O_3NPs calcined at 200 °C.

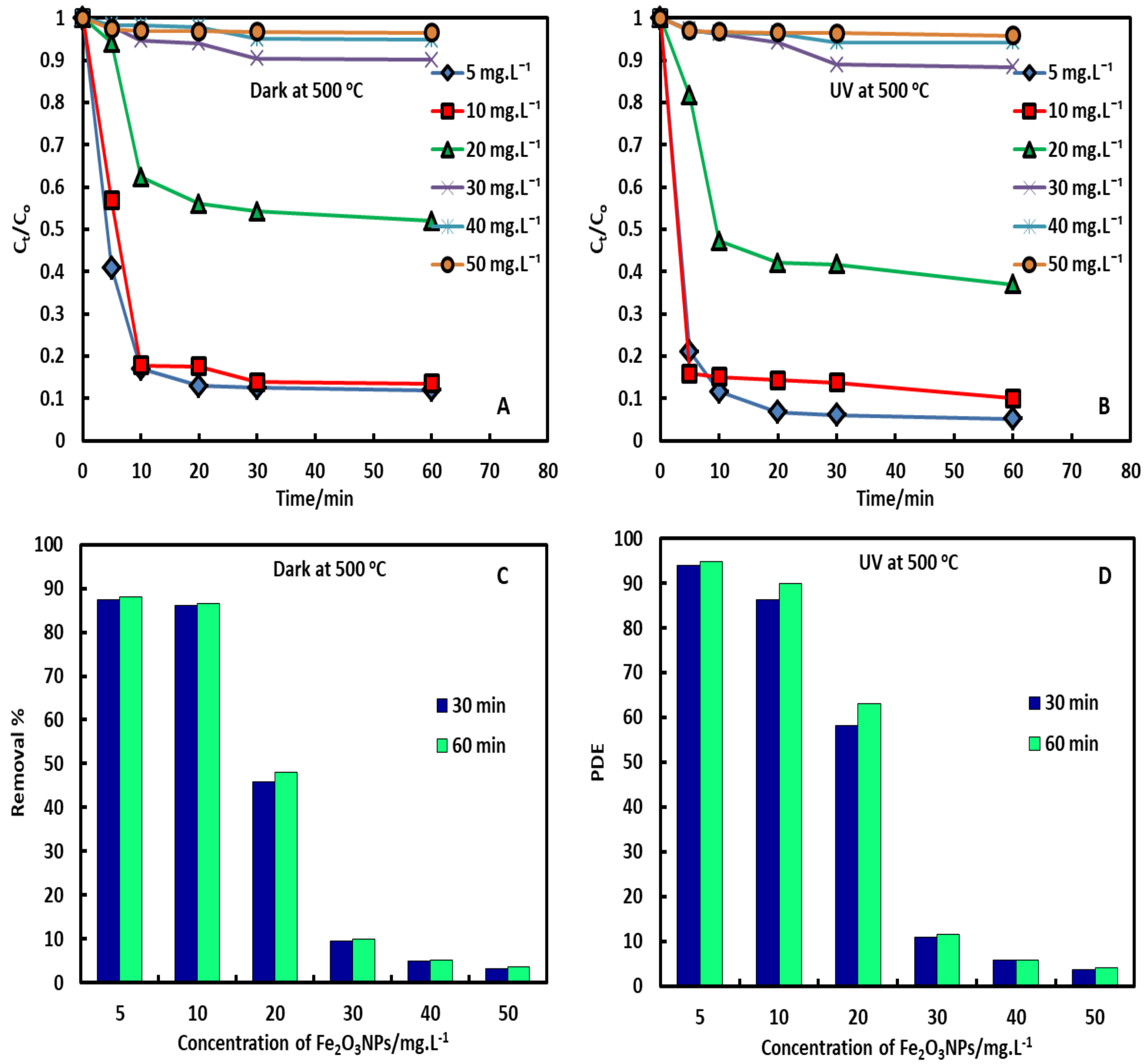

Figure 3.31 Effect of initial concentration on the removal percentage and photodegradation efficiency of FSS dye under (**A** and **C**) dark conditions and (**B** and **D**) UV light in the presence of Fe_2O_3NPs calcined at 500 °C.

3.2.3 The Impact of Temperature on FSS dye Adsorption and Photocatalytic Activity

In this experiment, four different temperatures were used to study how the temperature affected FSS adsorption by using Fe_2O_3NPs in dark and UV light, and the results are shown in Figure 3.32 and Figure 3.33. It can be seen from Figure 3.32 and Figure 3.33 that the amount of FSS that is adsorbed increases with increasing ambient temperature.

The fact that the adsorption increases with temperature suggests that the FSS dye molecules are moving more quickly. Furthermore, as temperature rises, dye molecules diffuse more quickly because the viscosity of the dye solution decreases. The values of $\Delta S°$, $\Delta H°$ and $\Delta G°$ obtained from the temperature data utilizing related equations [25] are 161 J/K, 24 kJ/mol and -22 kJ/mol, respectively. The results show that the adsorption process was a spontaneous process, according to the negative value of $\Delta G°$. The fact that $\Delta G°$ decreases as temperature increases suggest that adsorption is more effective at higher temperatures. The positive values of $\Delta H°$ confirm that the sorption of FSS dye onto Fe_2O_3NPs is endothermic in nature. Figure 3.34 displays the Van't Hof plot for the adsorption of FSS dye on Fe_2O_3NPs [25].

It is well knowledge that several operations carried out in the dyeing and printing departments of the textile industry take place at high temperatures. In these situations, the treatment plant receives the wastewater containing dyes at high temperatures. Given that adsorption improves at high temperatures, it is reasonable to assume that by using Fe_2O_3NPs in the textile industry, high adsorption efficiency can be obtained [147]. The results represented in Figure 3.33 show that the Fe_2O_3NPs calcined at 500 °C have lower adsorption and photocatalytic activity on FSS dye when compared to the Fe_2O_3NPs calcined at 200 °C Figure 3.32 . One possible explanation is that the increase of the calcination temperature leads to an increase of size of Fe_2O_3NPs. Thus, the smallest size was obtained at the lowest calcination temperature (200 °C). It was also found that the Fe_2O_3NPs surface area increased as the calcination temperature declined.

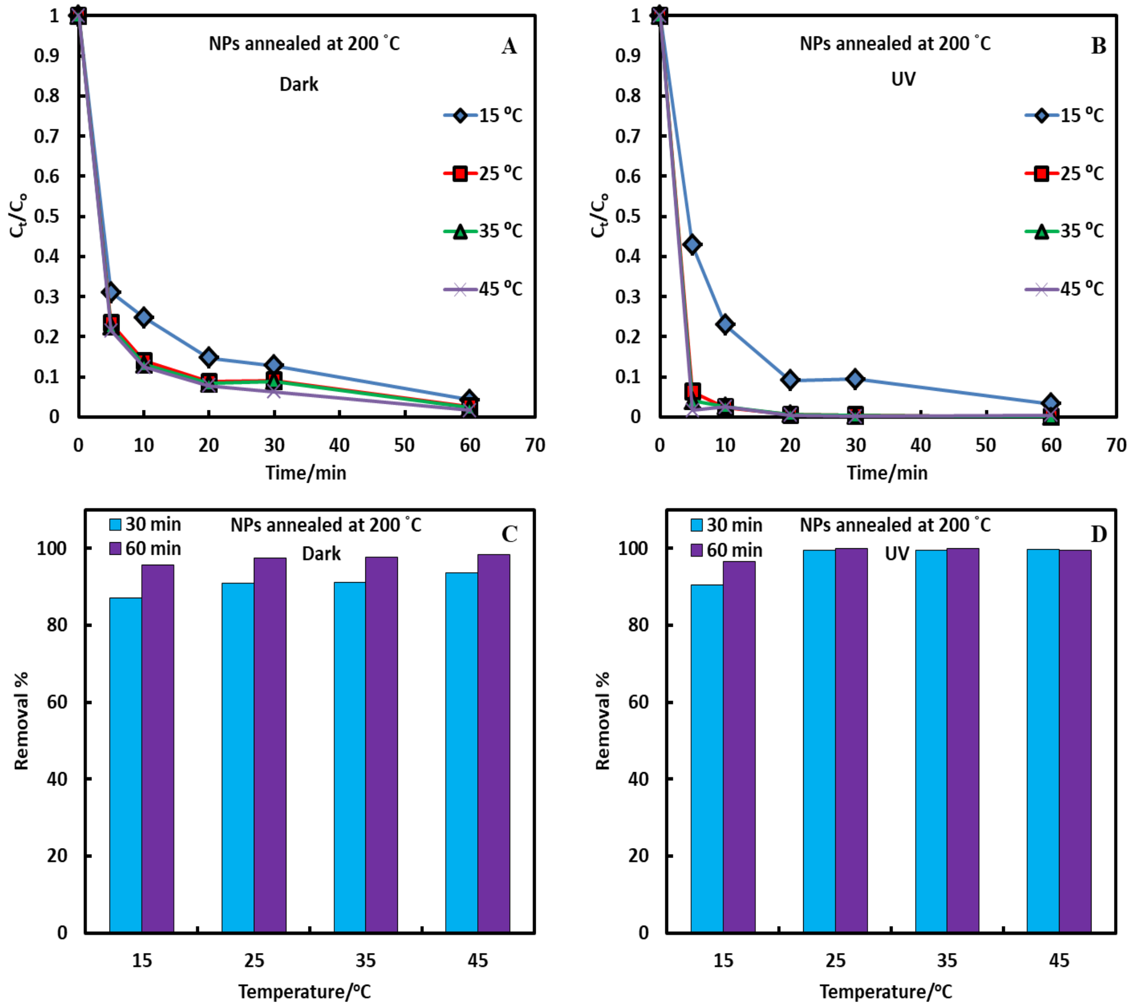

Figure 3.32 The impact of the temperature on FSS dye adsorption and photodegradation efficiency of Fe_2O_3NPs synthesized after annealing of Fe_2O_3 at 200 °C (**A, C**) under dark and (**B**, **D**) UV light.

The photocatalytic and adsorption properties of different amounts of Fe_2O_3NPs toward was also examined of FSS dye under UV irradiation as well as in dark conditions Figure 3.28. The works were carried out in 100 cm^3 solution of 10 mg L^{-1} initial FSS concentration at room temperature. The percentage of FSS dye adsorption and photodegradation efficiency increased with increasing doses of Fe_2O_3NPs as illustrated in Figure 3.28.

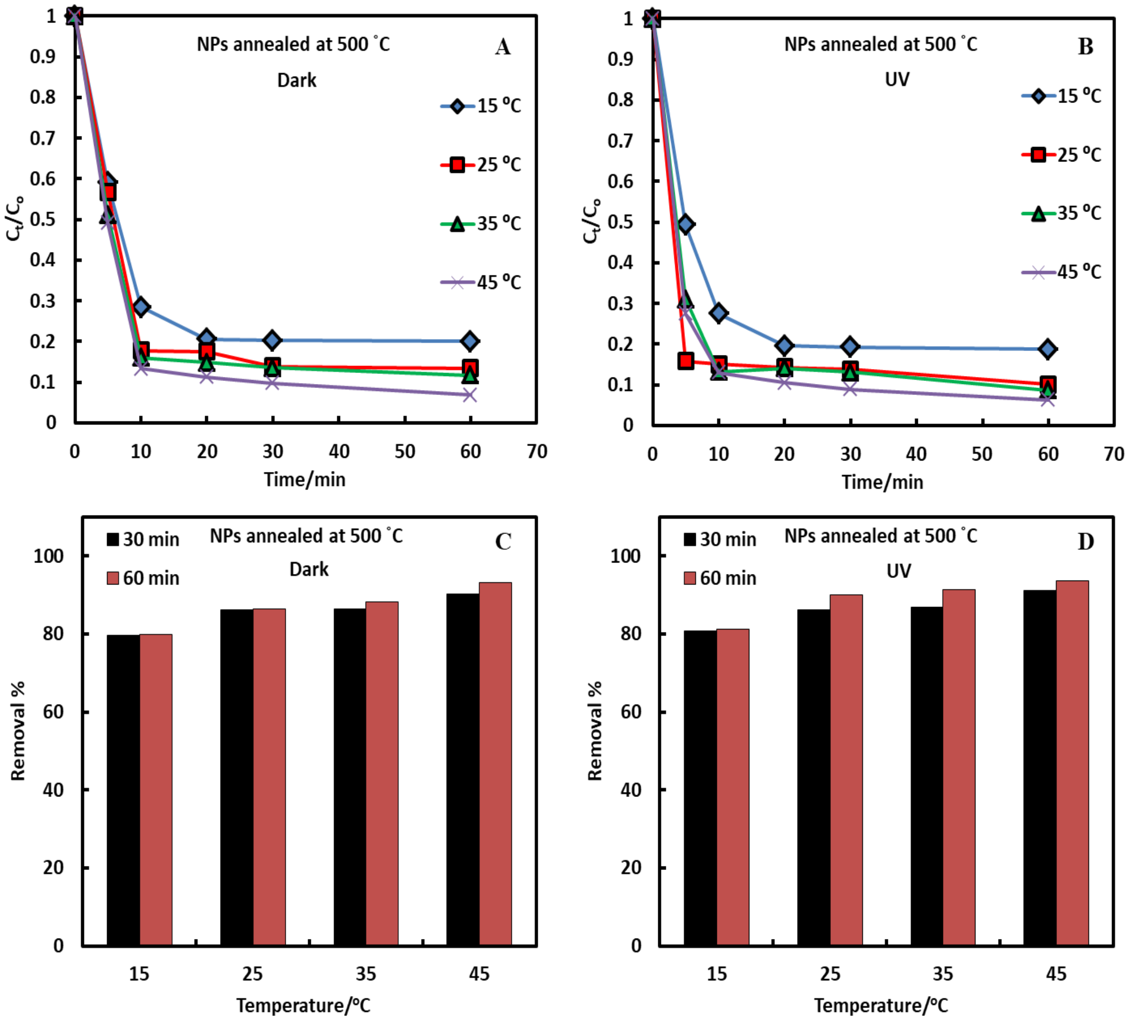

Figure 3.33 The influence of the temperature on FSS dye adsorption and photodegradation efficiency of Fe_2O_3NPs synthesized after annealing of Fe_2O_3 at 500 °C (**A, C**) under dark and (**B**, **D**) UV light.

3.2.4 Kinetics and Adsorption Isotherms of FSS Dye Adsorption on Fe_2O_3NPs

The kinetics of FSS adsorption on Fe_2O_3NPs was studied. At room temperature, batch systems were used for all experimental tests. Kinetic studies are crucial in the field of adsorption because they shed light on the adsorption mechanism. The adsorption ability and rate constant of a Fe_2O_3NPs substance used as an adsorbent must be higher. In this work, pseudo-first- and second-order kinetics was used.

The perfectly matched plots of the adsorption kinetic model are shown in Figure 3.35 and Figure 3.36. First-order kinetic graphs for the FSS dye are shown in Figure 3.35, whereas second-order kinetic plots are shown in Figure 3.36. It was discovered that the correlation coefficient of the pseudo-second-order model was significantly higher than that of the pseudo-first-order model Table 1. Additionally, it was observed that the pseudo-second-order model's plotted simulated adsorption capacity had a better fit with the data than the pseudo-first-order model's estimated adsorption capacity see Figure 3.35 and Figure 3.36. Thus, the pseudo-second-order model provides the most accurate description of the adsorption mechanism for FSS dye on Fe_2O_3NPs.

The kinetic parameters for FSS dye on Fe_2O_3NPs obtained from the plots in Figure 3.35 and Figure 3.36 are given in Table 1. The interaction between adsorbate particles and adsorbents can be predicted using the isotherm models, which offer useful information. Applying the Langmuir and Freundlich linear isotherm models, the mechanism of FSS dye adsorption onto Fe_2O_3NPs was investigated. Figure 3.37 displays the Langmuir isotherms of FSS dye on Fe_2O_3NPs, whereas Figure 3.38 displays the Freundlich isotherm models. These models were used to determine the maximum adsorption abilities of FSS dye on Fe_2O_3NPs. It was found that adsorption isotherms of FSS dye adsorption on Fe_2O_3NPs show good agreement with the Langmuir isotherm model. It was use the calculated n values of the Freundlich model to illustrate the heterogeneities on the surface of Fe_2O_3NPs Figure 3.38. In cases where n is more than 1, equal to 1, or less than 1, adsorption will be physical, linear, or chemical, respectively. The FSS dye has n values higher than 1 as shown in Table 2, which in our study suggests that the absorption is physical absorption [29].

Van't Hof equation $\Delta G° = \Delta H° - T\,\Delta S°$

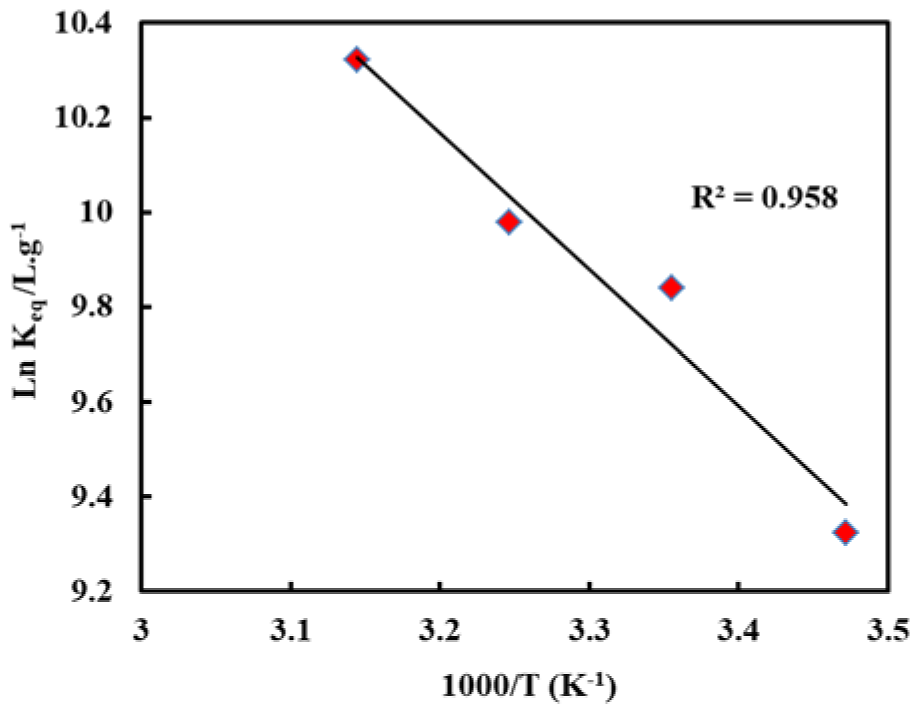

Figure 3.34 Plot of $\ln K_{eq}$ versus 1000/T for estimation of thermodynamic parameters.

Table 3.1 Pseudo first and pseudo second order kinetic models for adsorption of FSS dye on Fe_2O_3NPs

Fe_2O_3NPs Mass/g	Pseudo-first order kinetic model				Pseudo-second order kinetic model		
	$q_{e,exp}$ (mg/g)	$q_{e,cal}$ (mg/g)	k_1 (min^{-1})	R^2	$q_{e,cal}$ (mg/g)	k_2 (g/mg min)	R^2
0.05	**18.033**	**18.832**	**1.713**	**0.901**	**18.450**	**0.707**	**0.9997**
0.1	**9.728**	**9.832**	**1.879**	**0.876**	**9.990**	**0.441**	**0.9977**
0.15	**6.788**	**6.618**	**1.301**	**0.938**	**6.988**	**0.430**	**0.9982**
0.2	**5.094**	**5.099**	**1.365**	**0.95**	**5.213**	**0.555**	**0.9992**
0.25	**4.094**	**4.096**	**1.397**	**0.946**	**4.199**	**0.539**	**0.9995**
0.3	**3.407**	**3.408**	**1.329**	**0.945**	**3.491**	**0.562**	**0.9996**

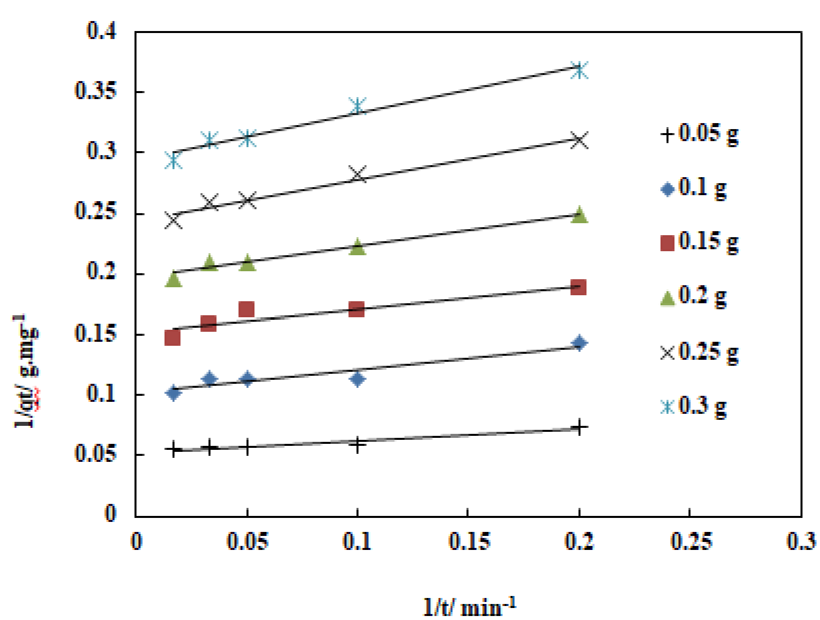

Figure 3.35 Kinetics and adsorption isotherms of FSS dye adsorption on Fe_2O_3NPs. Pseudo-first-order for FSS dye.

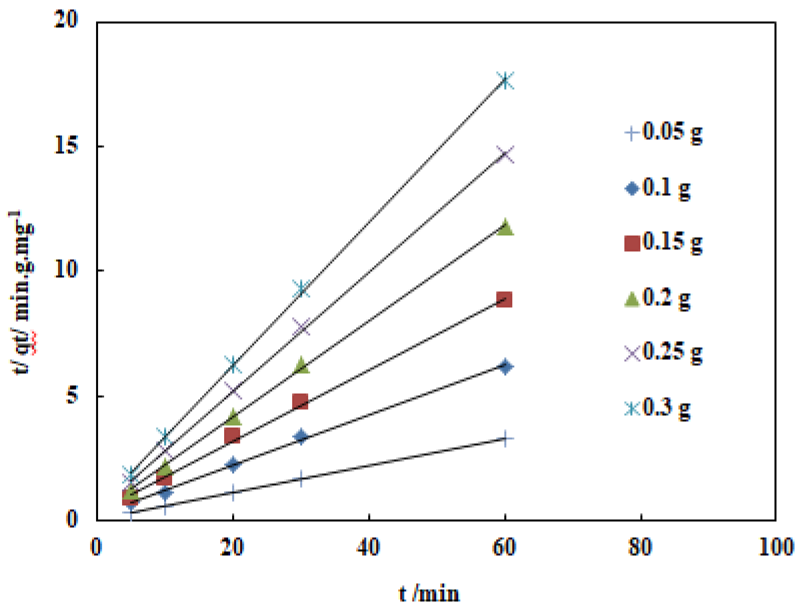

Figure 3.36 Kinetics and adsorption isotherms of FSS dye adsorption on Fe_2O_3NPs pseudo-second-order model for FSS dye.

Table 3.2 Adsorption isotherms for FSS dye on Fe_2O_3NPs according to Langmuir and Freundlich isotherm models.

Langmuir Isotherm			Ferundlich Isotherm		
q_m $(mg.g^{-1})$	$b(dm^3.g^{-1})$	R^2	K_f $(mg.g^{-1})$	n	R^2
16.025	0.624	0.956	5.922	2.957	0.881

Langmuir Ce/qe =1/qmK1 + Ce/qm

Freundlich Log qe = Log K

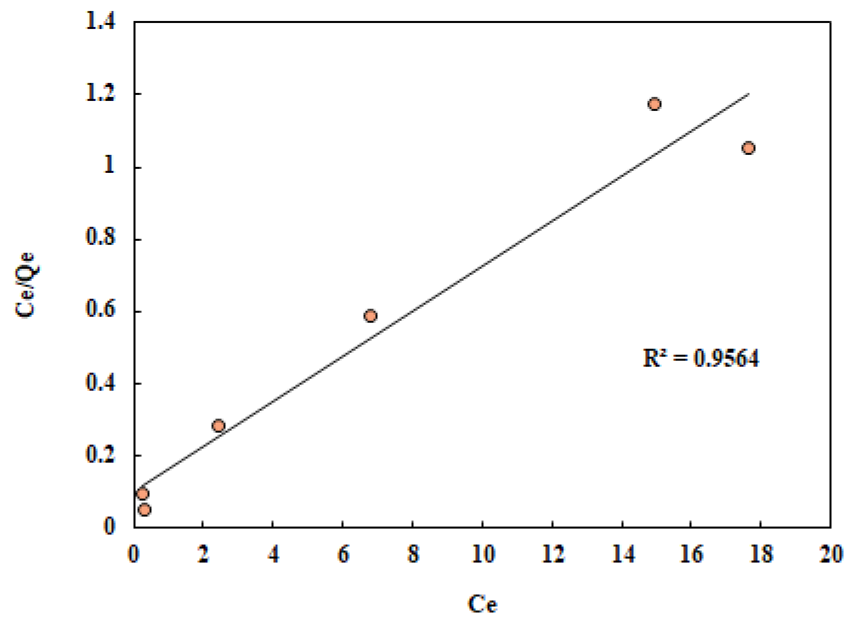

Figure 3.37 Adsorption isotherms for FSS dye on Fe_2O_3NPs according to Langmuir isotherm models.

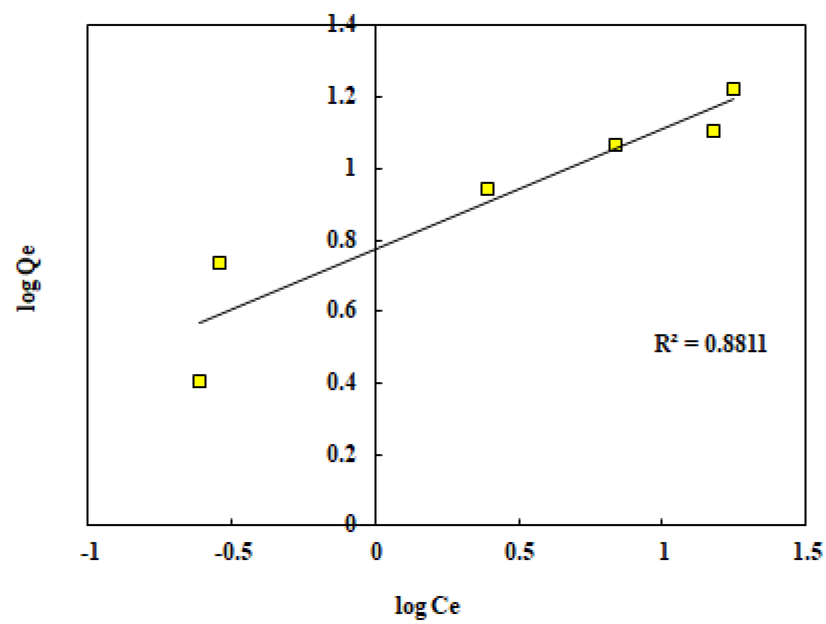

Figure 3.38 Adsorption isotherms for FSS dye on Fe_2O_3NPs according to Freundlich isotherm models.

3.2.5 Adsorption and Photocatalytic Action of FSS Dye on Polyelectrolyte-Coated Fe_2O_3NPs

The adsorption and photocatalyst efficiency of polyelectrolyte-coated Fe_2O_3NPs with FSS dye was tested. It was designed and synthesized Fe_2O_3NPs with PSS and PAH and compared their photodegradation efficiency and FSS dye removal % to that of the uncoated Fe_2O_3NPs under UV light and dark. The 0.2 g of Fe_2O_3NPs/PSS and Fe_2O_3NPs/PSS/PAH were combined with the aqueous solution of 10 mg L^{-1} FSS dye at different times for up to an hour. The data shown in Figure 3.40(C) and Figure 3.41(C) indicate that the anionic Fe_2O_3NPs/PSS has less ability for adsorption and photocatalytic degradation of the FSS dye than the cationic bare Fe_2O_3NPs (see Figure 3.28). Similar treatment with the cationic Fe_2O_3NPs/PSS/PAH displayed high FSS dye adsorption and photocatalytic activity as displayed in Figure 3.40(D) and Figure 3.41(D). The results show that the removal percentage and photodegradation efficiency of Fe_2O_3NPs coated with an outer layer of anionic polyelectrolyte is greatly reduced, as a result of the electrostatic repulsion between the anionic surface of FSS dye and the anionic Fe_2O_3NPs/PSS. However, after applying the second layer of PAH to coat Fe_2O_3NPs/PSS, the surface charge of the particles is reversed from negative to positive. Polyelectrolyte-coated Fe_2O_3NPs were also examined for their ability to adsorb and act as a photocatalyst when combined with a high concentration of FSS dye (50 mg L^{-1}) as shown in Figure 3.42 and Figure 3.43. The removal rate of FSS dye was significantly influenced by the positive surface charge of the Fe_2O_3NPs/PSS/PAH. The polyelectrolyte-coated Fe_2O_3NPs formula for alternate photocatalytic and adsorption activity appears to be related to their surface charge and the associated electrostatic adherence to the negatively charged FSS dye [29]. The results show that the photodegradation efficiency and removal % of FSS dye on the cationic nanoparticles Fe_2O_3NPs/PSS/PAH Figure 3.40(D) and Figure 3.41(D) are much higher than those of their anionic form Fe_2O_3NPs/PSS Figure 3.40(C) and Figure 3.41(C).

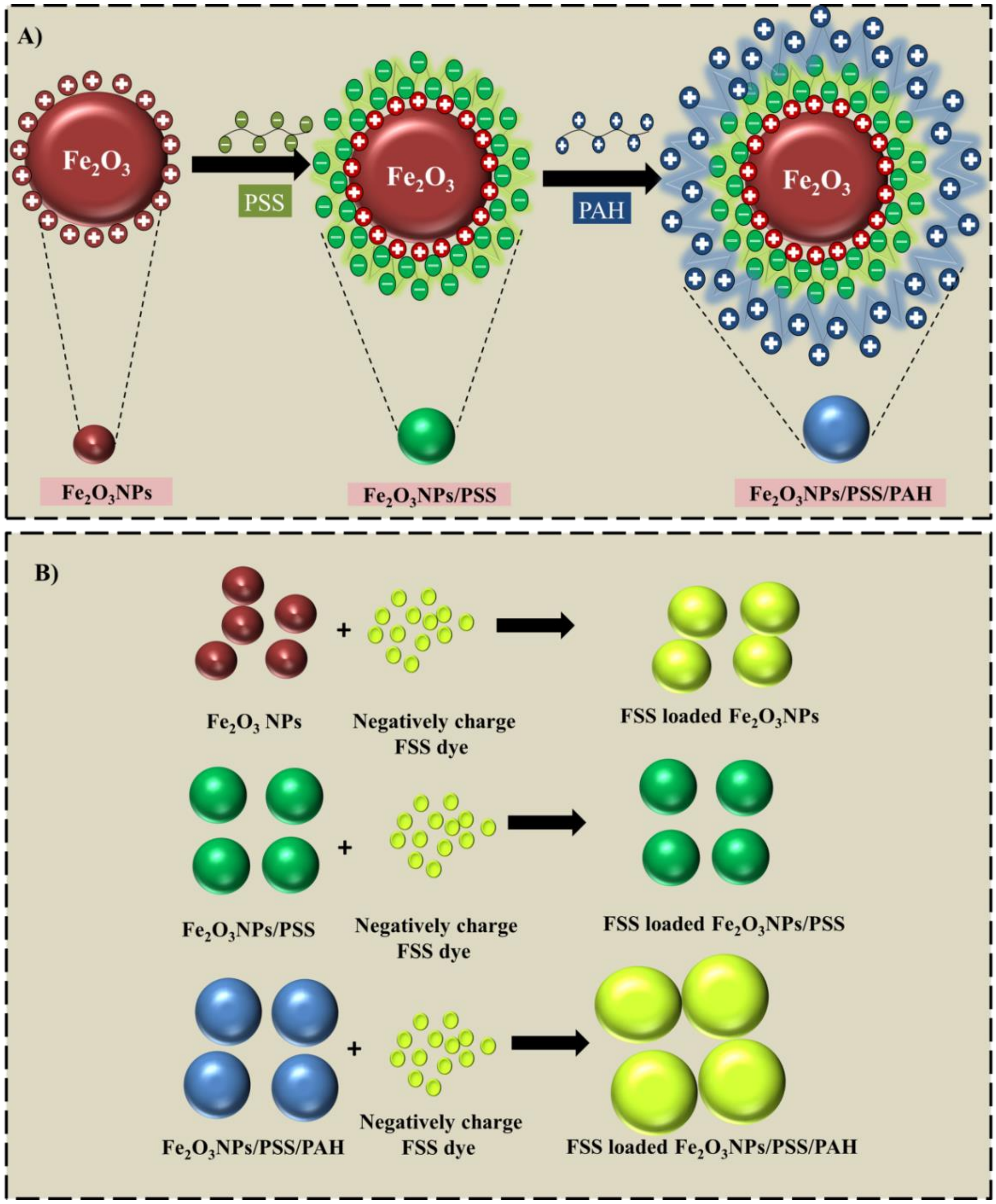

Figure 3.39 A Schematic diagram showing the coating of bare Fe_2O_3NPs with two consecutive layers of anionic PSS and cationic PAH polyelectrolytes. **B** Schematic diagram showing the adsorption of FSS dye on bare and surface modified Fe_2O_3NPs.

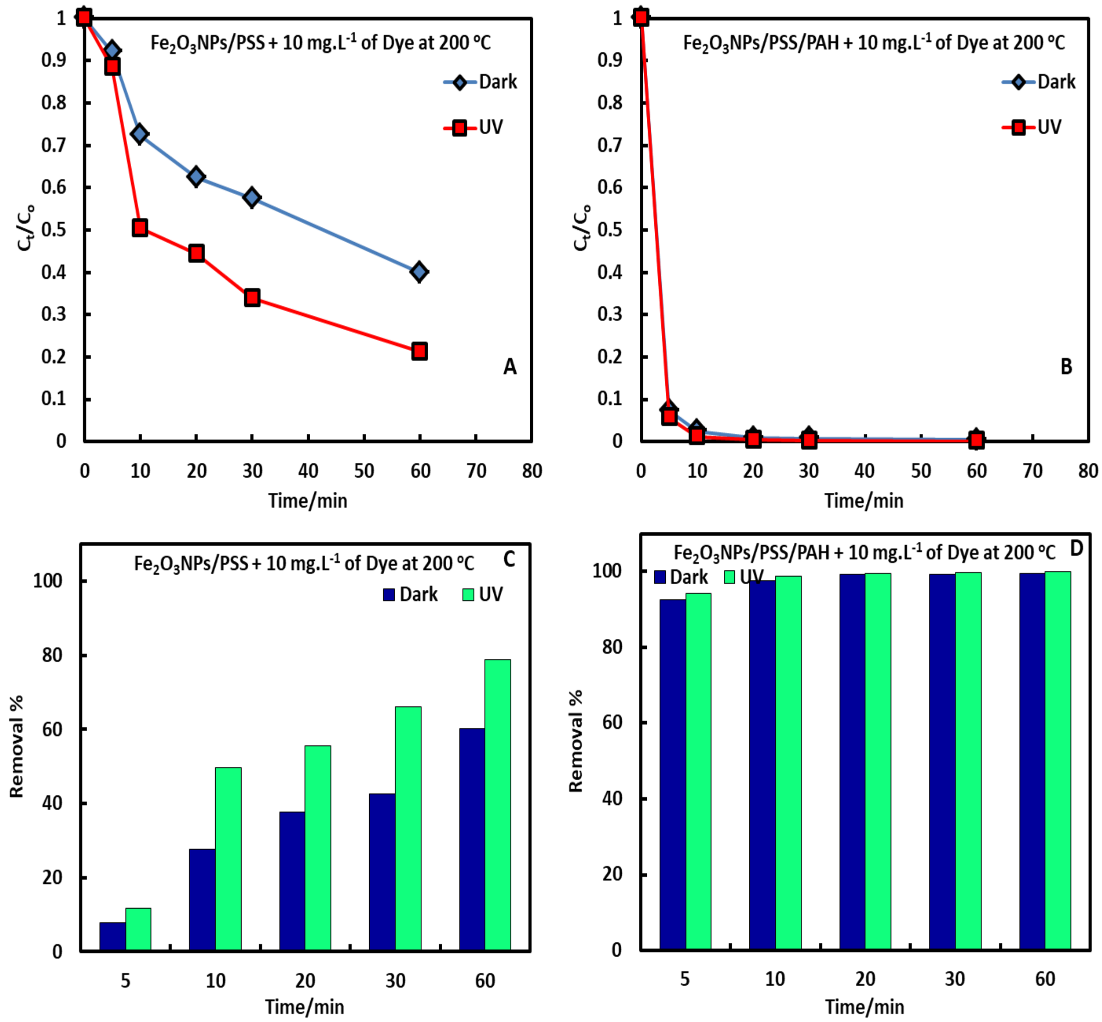

Figure 3.40 The removal percentage and photodegradation efficiency of FSS dye on polyelectrolyte-coated Fe_2O_3NPs synthesized after annealing of Fe_2O_3 at 200 °C toward FSS dye. The removal percentage of 10 mg L^{-1} FSS dyes after mixing for up to 1 h with (**A**, **C**) 0.2 g of Fe_2O_3NPs/PSS and (**B**, **D**) Fe_2O_3NPs/PSS/PAH at room temperature.

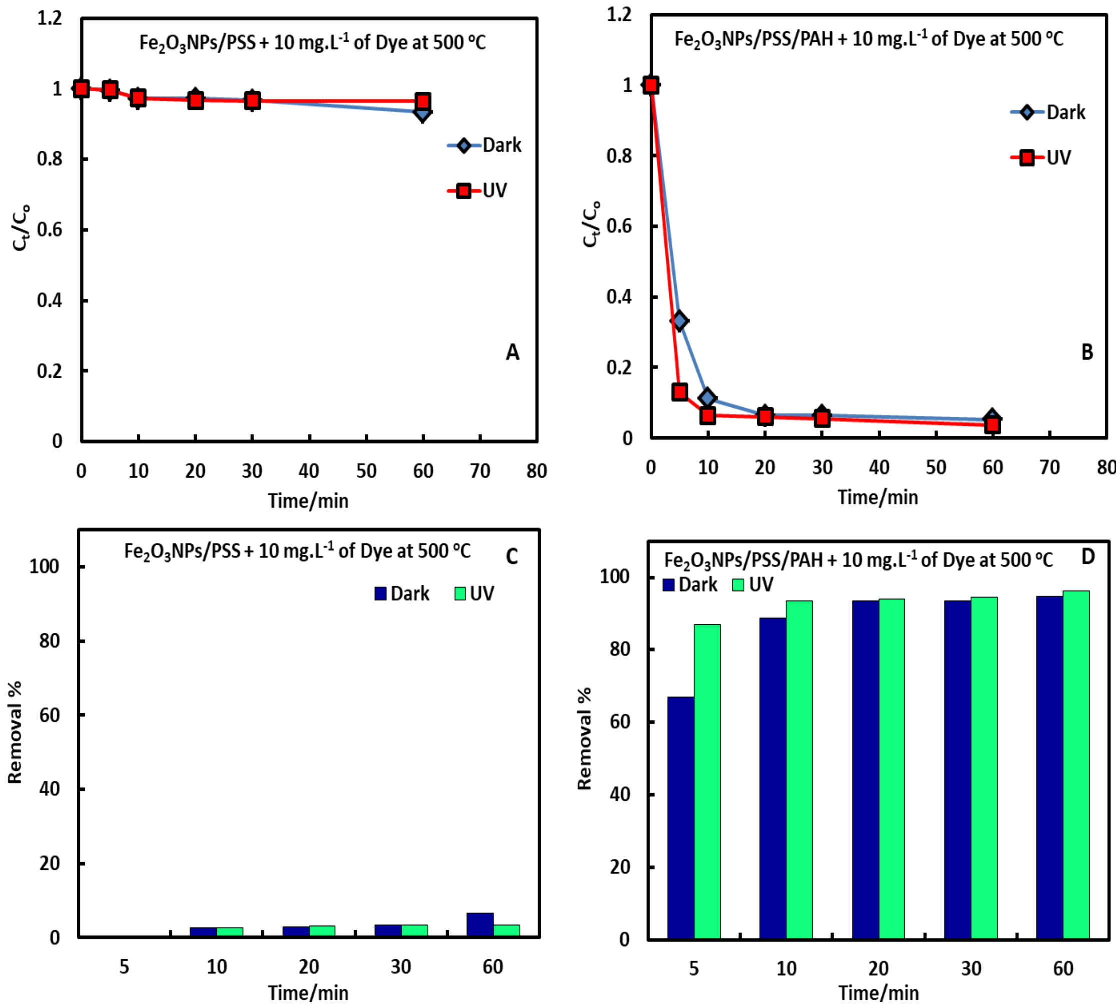

Figure 3.41 The removal percentage and photodegradation efficiency of FSS dye on polyelectrolyte-coated Fe_2O_3NPs synthesized after annealing of Fe_2O_3 at 500 °C toward FSS dye. The removal percentage of 10 mg L^{-1} FSS dyes after mixing for up to 1 h with (**A**, **C**) 0.2 g of Fe_2O_3NPs/PSS and (**B**, **D**) Fe_2O_3NPs/PSS/PAH at room temperature.

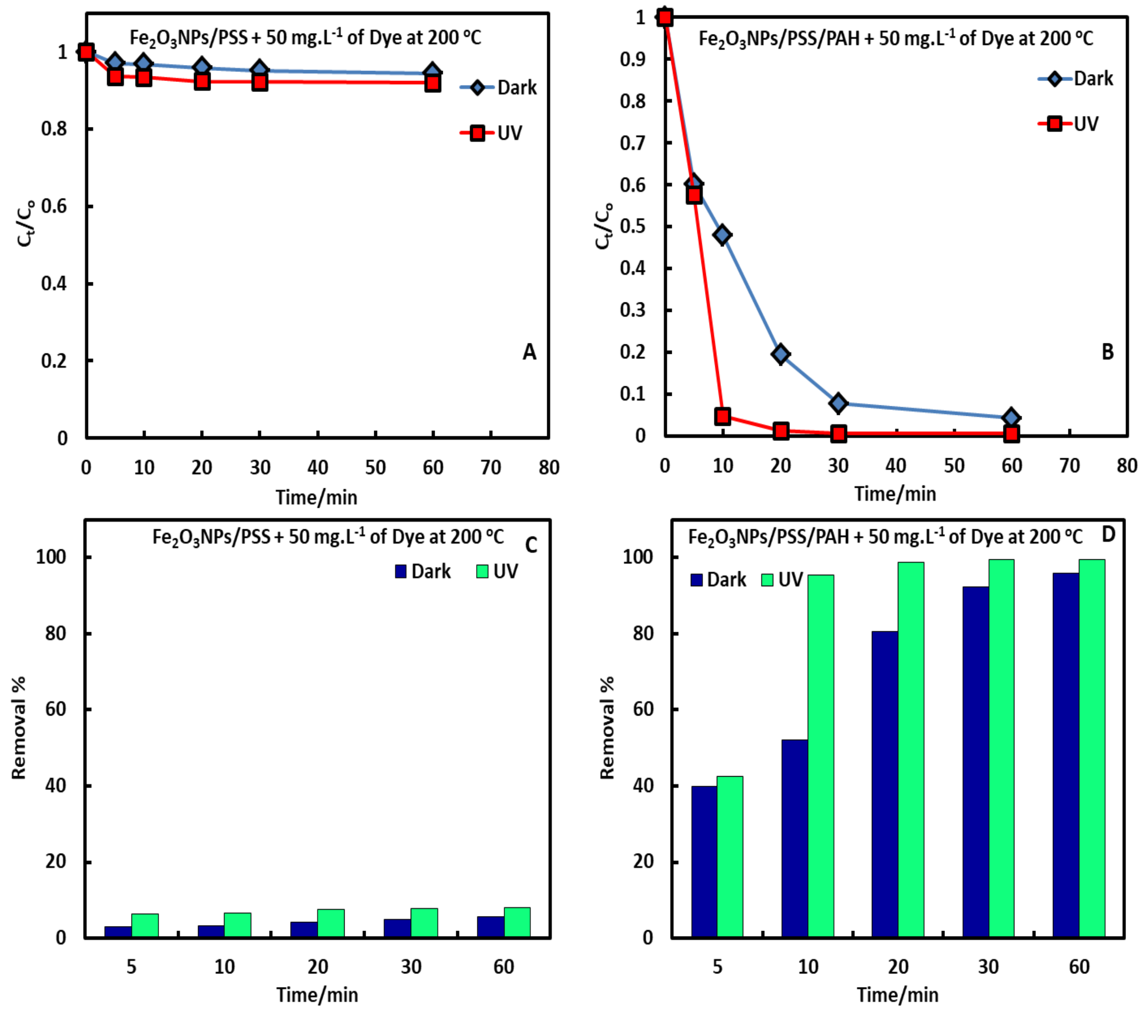

Figure 3.42 The removal percentage and photodegradation efficiency of FSS dye on polyelectrolyte-coated Fe_2O_3NPs synthesized after annealing of Fe_2O_3 at 200 °C toward FSS dye. The removal percentage of 50 mg L^{-1} FSS dyes after mixing for up to 1 h with (**A**, **C**) 0.2 g of Fe_2O_3NPs/PSS and (**B**, **D**) Fe_2O_3NPs/PSS/PAH at room temperature.

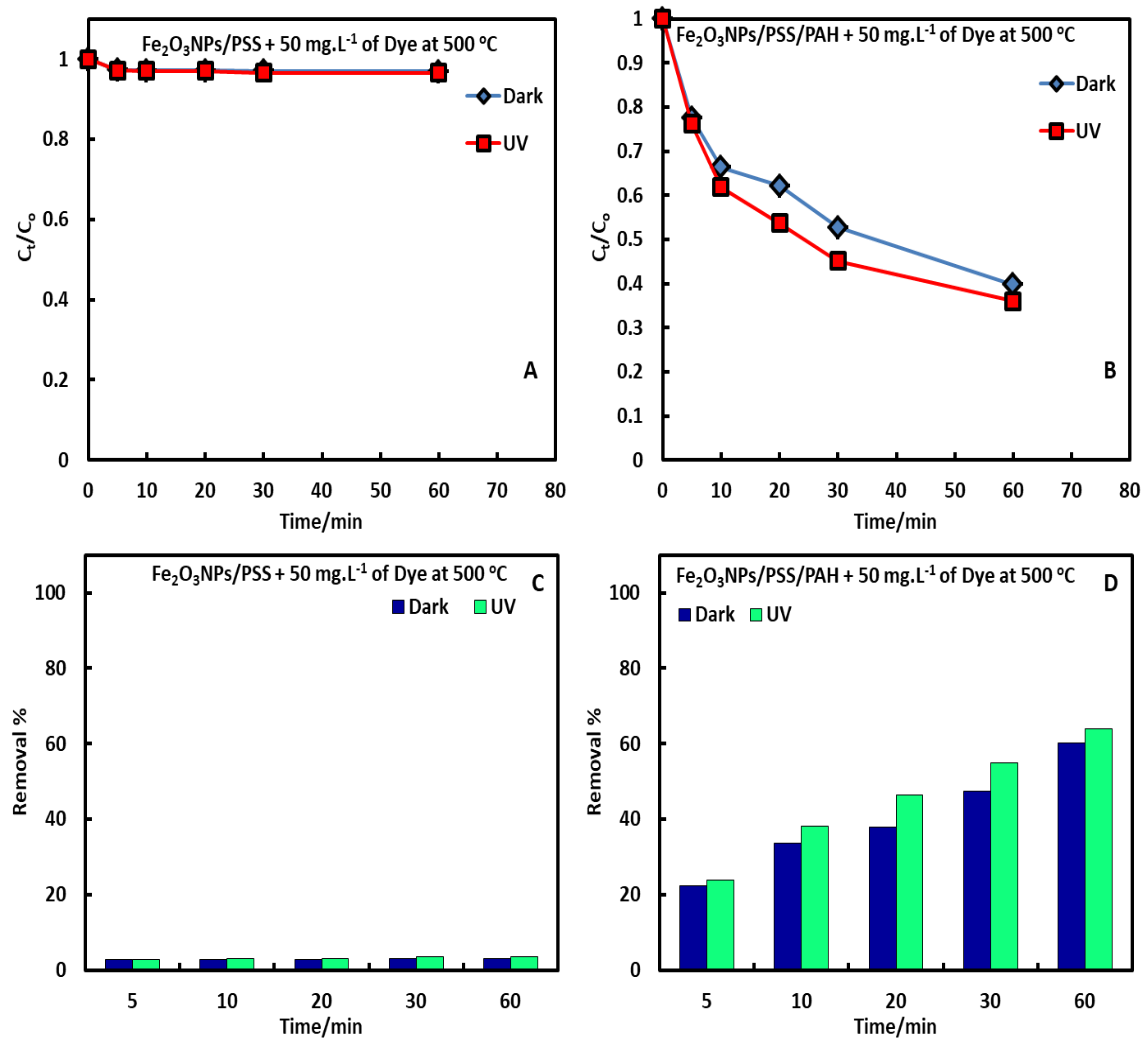

Figure 3.43 The removal percentage and photodegradation efficiency of FSS dye on polyelectrolyte-coated Fe_2O_3NPs synthesized after annealing of Fe_2O_3 at 500 °C toward FSS dye. The removal percentage of 50 mg L^{-1} FSS dyes after mixing for up to 1 h with (**A**, **C**) 0.2 g of Fe_2O_3NPs/PSS and (**B**, **D**) Fe_2O_3NPs/PSS/PAH at room temperature.

3.2.6 Comparison of the effect of Polyelectrolyte-Coated Fe_2O_3NPs, free PSS and free PAH on the removal percentage of FSS

Figure 3.44 Shows the effect of free PSS and Figure 3.45 shows the effect of free PAH and Figure 3.46 to Figure 3.49 summarizes the effect of free PSS, free PAH, bare Fe_2O_3NPs, Fe_2O_3NPs/PSS and Fe_2O_3NPs/PSS/PAH on the removal percentage and photodegradation efficiency of 10 mg L^{-1} FSS dye under the same conditions of 0.2 g particle dose for 1 h in dark and UV light. This result indicated that the bare Fe_2O_3NPs and Fe_2O_3NPs/PSS/PAH have a strong effect on the removal of FSS dye both in dark and under UV light. This influence can be described with the positive particle surface charge leading to a strong electrostatic attraction between the cationic surface of the bare Fe_2O_3NPs and Fe_2O_3NPs/PSS/PAH and the anionic surface of the FSS dye.

The data in Figure 3.(46,47) and (Figure 3.49) show that the presence of Fe_2O_3NPs/PSS/PAH has a much higher impact on the FSS dye removal percentage in dark, and UV light conditions than that of the bare Fe_2O_3NPs, as the adhesion of the latter to the FSS dye is driven mainly by electrostatic forces. The results confirm that free PSS and free PAH on FSS dye have a negligible adsorption and photocatalytic activity on the FSS dye, whereas Fe_2O_3NPs/PSS have some low level of effect compared with the uncoated Fe_2O_3NPs and Fe_2O_3NPs/PSS/PAH. This is most likely due to the electrostatic repulsion between Fe_2O_3NPs/PSS and FSS dye as both have negatively charged surfaces in aqueous media which leads to a decrease in the removal percentage and photodegradation efficiency of FSS dye on Fe_2O_3NPs/PSS.

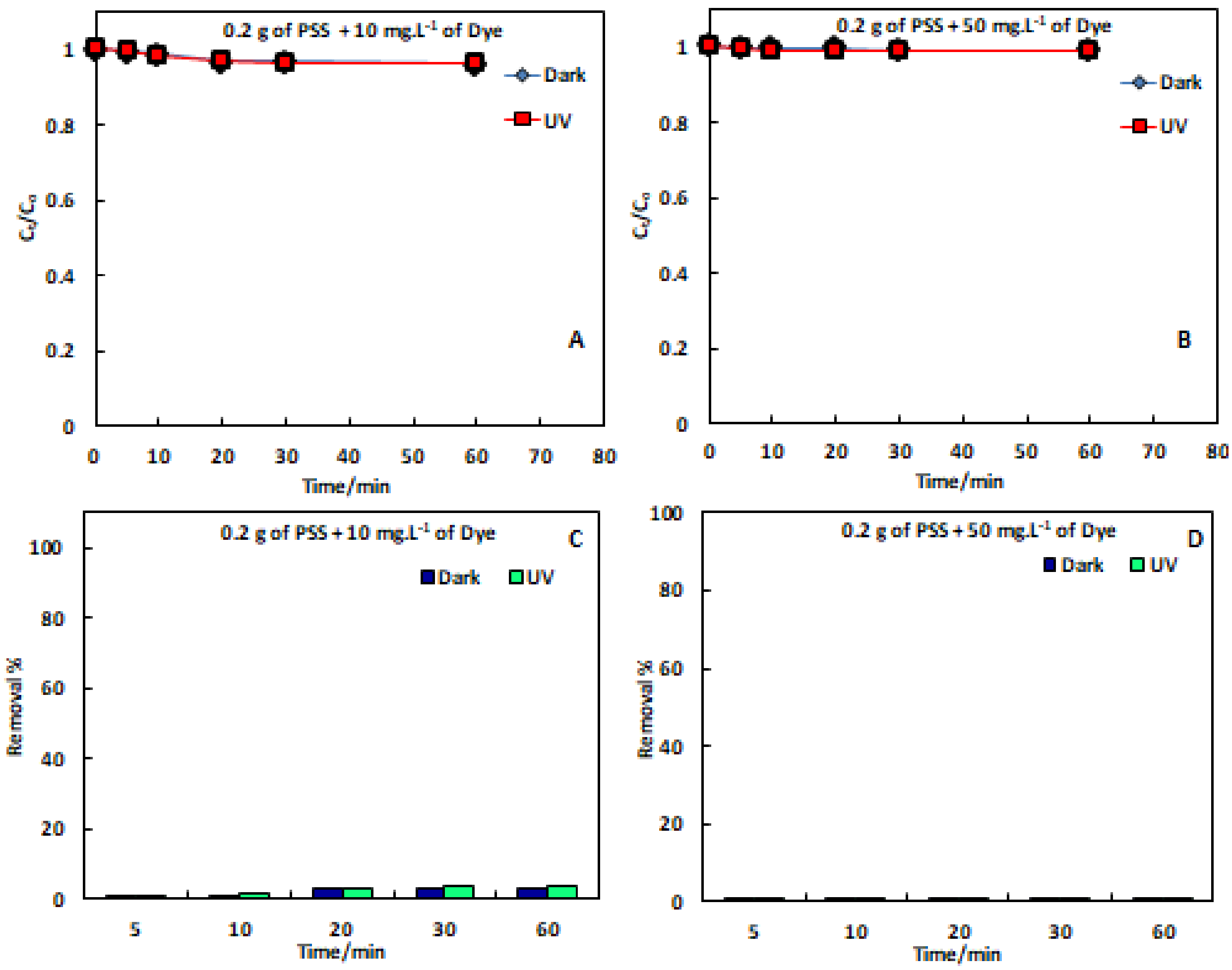

Figure 3.44 Comparison the effect of free PSS on the removal percentage of 10 and 50 mg.L^{-1} FSS dyes after mixing for up to 1 h with 0.2 g of PSS at UV light and Dark.

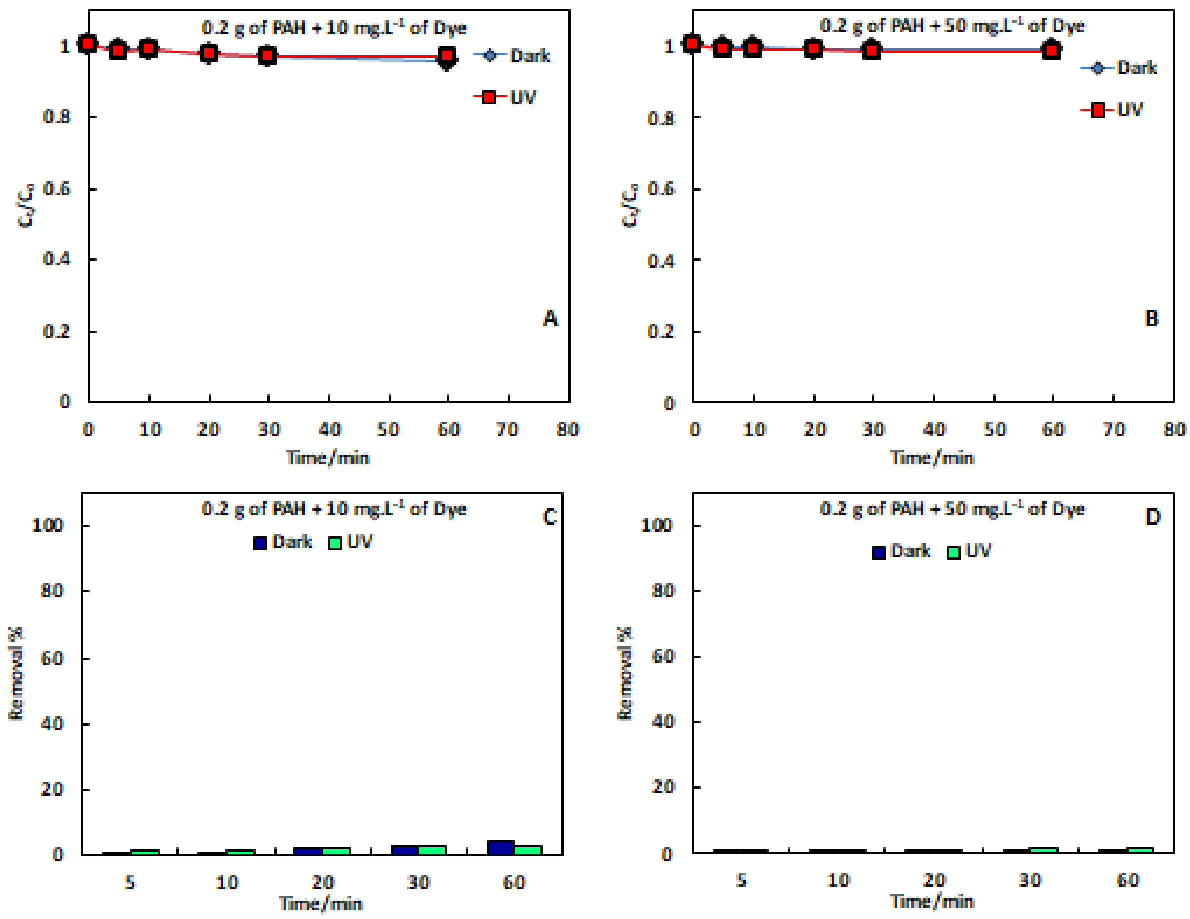

Figure 3.45 Comparison the effect of free PAH on the removal of 10 and 50 mg.L^{-1} FSS dyes after mixing for up to 1 h with 0.2 g of PAH at UV light and Dark.

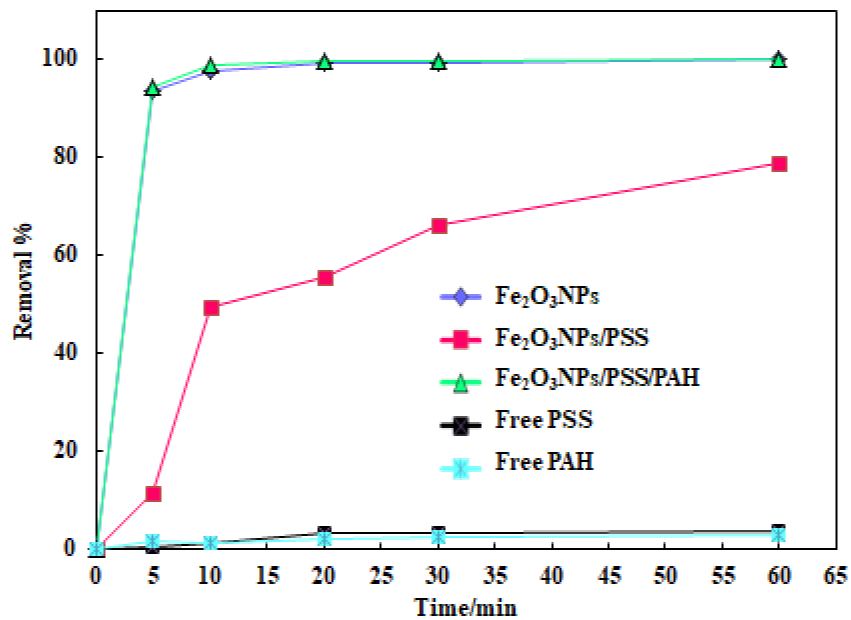

Figure 3.46 Comparison of the effect of free PSS, free PAH, free Fe_2O_3NPs, Fe_2O_3NPs/PSS, and Fe_2O_3NPs/PSS/PAH on the removal percentage and photodegradation efficiency of FSS dye in UV light for 1 h. 10 mg L^{-1} of FSS dye was mixed with the 0.2 g of nanoparticles synthesized after annealing of Fe_2O_3 at 200 °C.

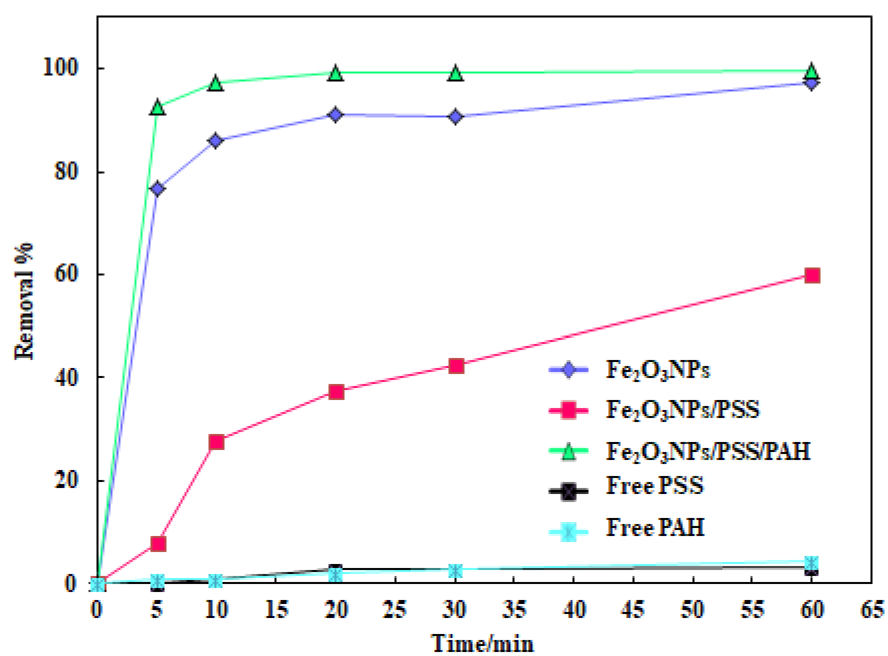

Figure 3.47 Comparison of the effect of free PSS, free PAH, free Fe_2O_3NPs, Fe_2O_3NPs/PSS, and Fe_2O_3NPs/PSS/PAH on the removal percentage and

photodegradation efficiency of FSS dye in dark for 1 h. 10 mg L^{-1} of FSS dye was mixed with the 0.2 g of nanoparticles synthesized after annealing of Fe_2O_3 at (**A**, **B**) 200 °C.

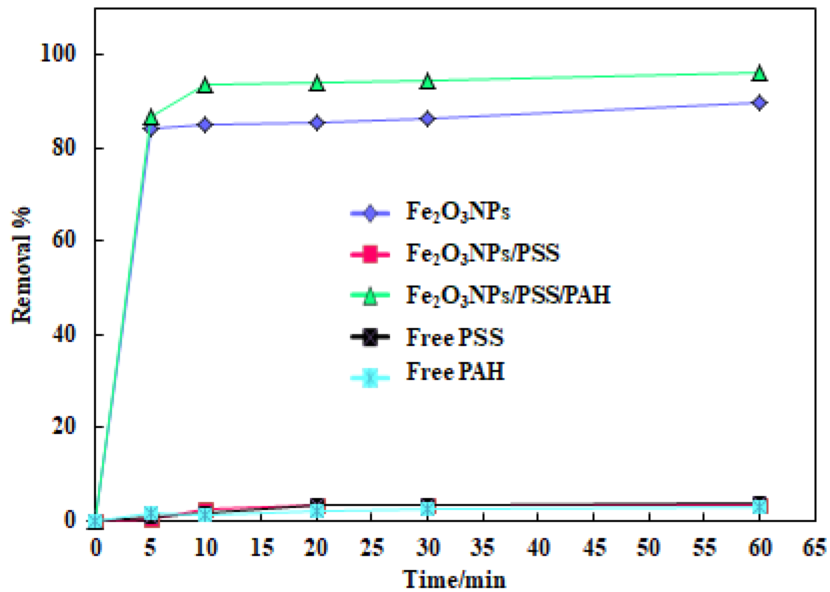

.

Figure 3.48 Comparison of the effect of free PSS, free PAH, free Fe_2O_3NPs, Fe_2O_3NPs/PSS, and Fe_2O_3NPs/PSS/PAH on the removal percentage and photodegradation efficiency of FSS dye in UV light for 1 h. 10 mg L^{-1} of FSS dye was mixed with the 0.2 g of nanoparticles synthesized after annealing of Fe_2O_3 at 500 °C.

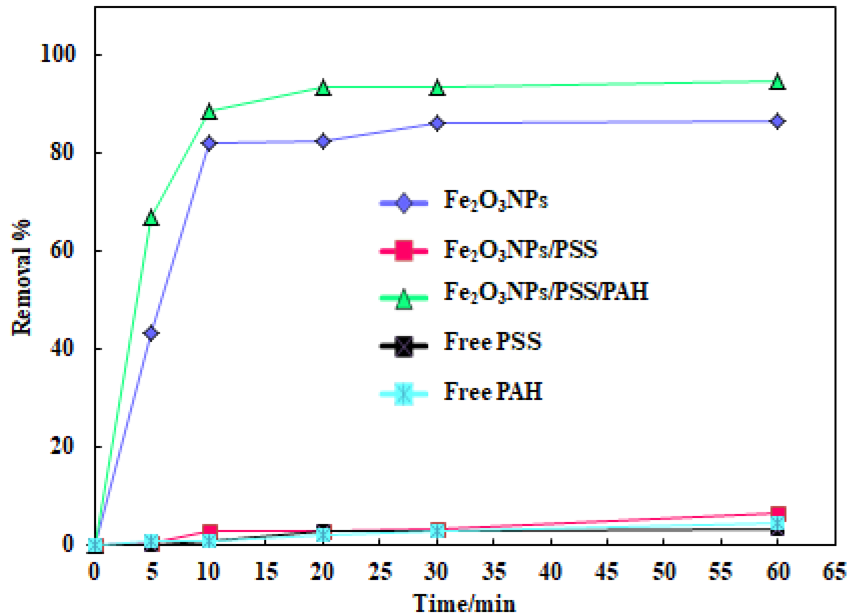

Figure 3.49 Comparison of the effect of free PSS, free PAH, free Fe_2O_3NPs, Fe_2O_3NPs/PSS, and Fe_2O_3NPs/PSS/PAH on the removal percentage and photodegradation efficiency of FSS dye in dark for 1 h. 10 mg L^{-1} of FSS dye was mixed with the 0.2 g of nanoparticles synthesized after annealing of Fe_2O_3 at 500 °C.

3.2.7 Separation of a Mixture of Dyes

Bare and surface modified Fe_2O_3NPs were employed to selectively separate different organic dyes because of their distinct and quick adsorption action towards FSS dye. The separation performance of unmodified and surface-modified Fe_2O_3NPs was tested using FSS/CV dye mixtures in an aqueous solution with various charge states. Free Fe_2O_3NPs and Fe_2O_3NPs/PSS/PAH are designed to eliminate anionic FSS dye from the mixed solution, whilst Fe_2O_3NPs/PSS may be able to remove cationic CV dye. Digital photos of the dye mixture of FSS and CV before and after adsorption with free Fe_2O_3NPs, Fe_2O_3NPs/PSS and Fe_2O_3NPs/PSS/PAH were taken, as shown in Figure 3.51(A) and Figure 3.52(A) and Figure 3.53(A).

The colors of the dye mixture were then compared to those of the two separate Figure 3.50 aqueous solutions of FSS/CV dyes. The color of the mixture of yellow FSS and blue-violet CV dyes changed to brown after being mixed as shown in Figure 3.50. The dye mixture solution's color changed from brown to blue-violet after 1 h of adsorption, fitting the color of the pure CV aqueous solution Figure 3.51(A) and Figure 3.53(A). Nearly all of the FSS dye was absorbed by the Fe_2O_3NPs and Fe_2O_3NPs/PSS/PAH Figure 3.51(B) and Figure 3.53(B). On the other hand, the Fe_2O_3NPs/PSS effectively absorbed all of the CV dyes Figure 3.52, changing the color of the dye combination solution from brown to yellow Figure 3.52, which matched the color of the pure FSS aqueous solution. The concentrations of FSS and CV in the mixture solution were determined using UV-Vis spectra before and after 1 h of adsorption with unmodified and surface-modified Fe_2O_3NPs, as shown in Figure 3.51(A) and Figure 3.52(A) and Figure 3.53(A). According to UV-Vis spectra measured after 1 h, Fe_2O_3NPs and Fe_2O_3NPs/PSS/PAH absorbed between 85 and 98 % of the FSS, whereas only a mere 10% of the CV.

This demonstrates that the dye mixture can be successfully separated using Fe_2O_3NPs and Fe_2O_3NPs/PSS/PAH by selectively adsorbing FSS from the dye mixture. These results can be explained by the reduced adsorption Fe_2O_3NPs and Fe_2O_3NPs/PSS/PAH to the CV dye because of electrostatic repulsion and the better particle-dye adsorption due to electrostatic interaction when cationic Fe_2O_3NPs and Fe_2O_3NPs/PSS/PAH are combined with anionic FSS dye.

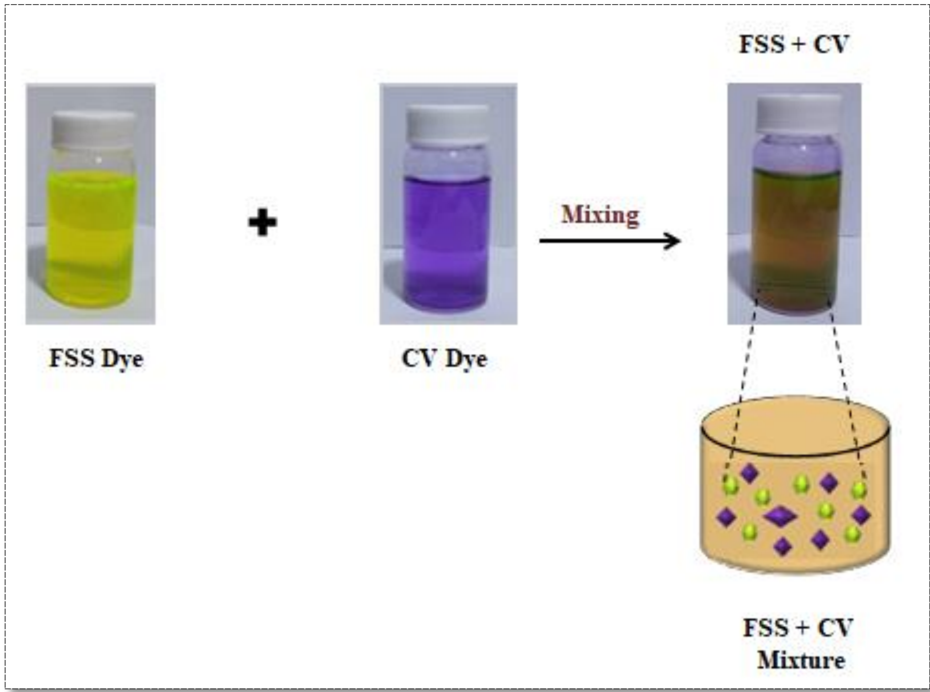

Figure 3.50 Schematic diagram showing the Photo of FSS/CV mixture solutions.

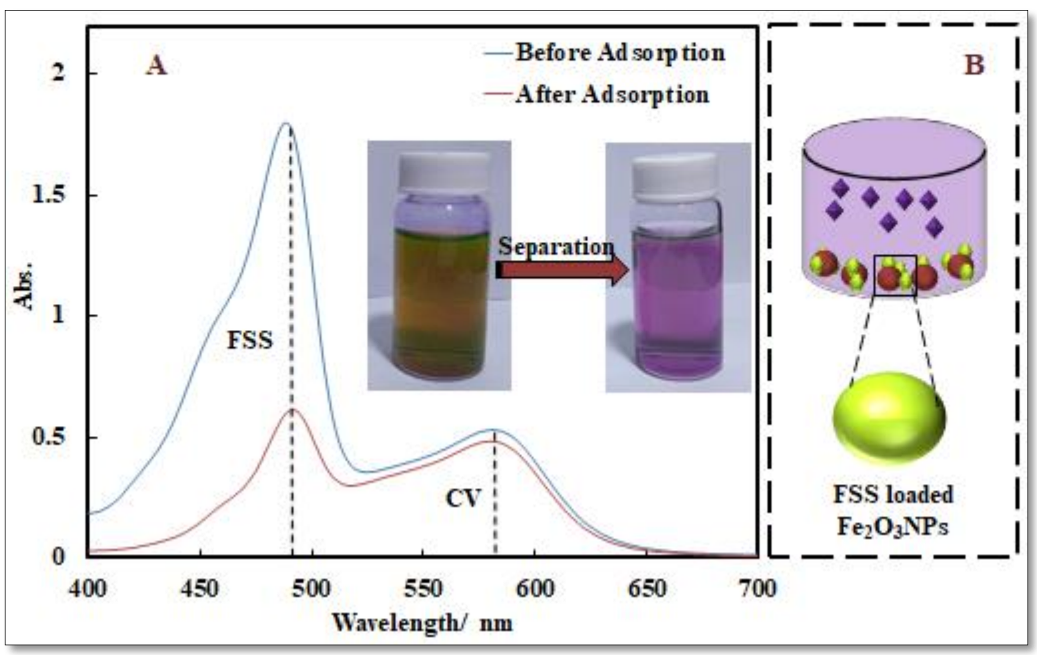

Figure 3.51 Schematic diagram showing the selective removal and adsorption of Fe_2O_3NPs with FSS/CV dye. UV–Vis spectra of FSS/CV mixture solutions before and

after adsorption on the **A** bare Fe_2O_3NPs. Photos inside Fig. **A** show the FSS/CV mixture solutions before adsorption and after adsorption. **B** FSS dye loaded Fe_2O_3NPs.

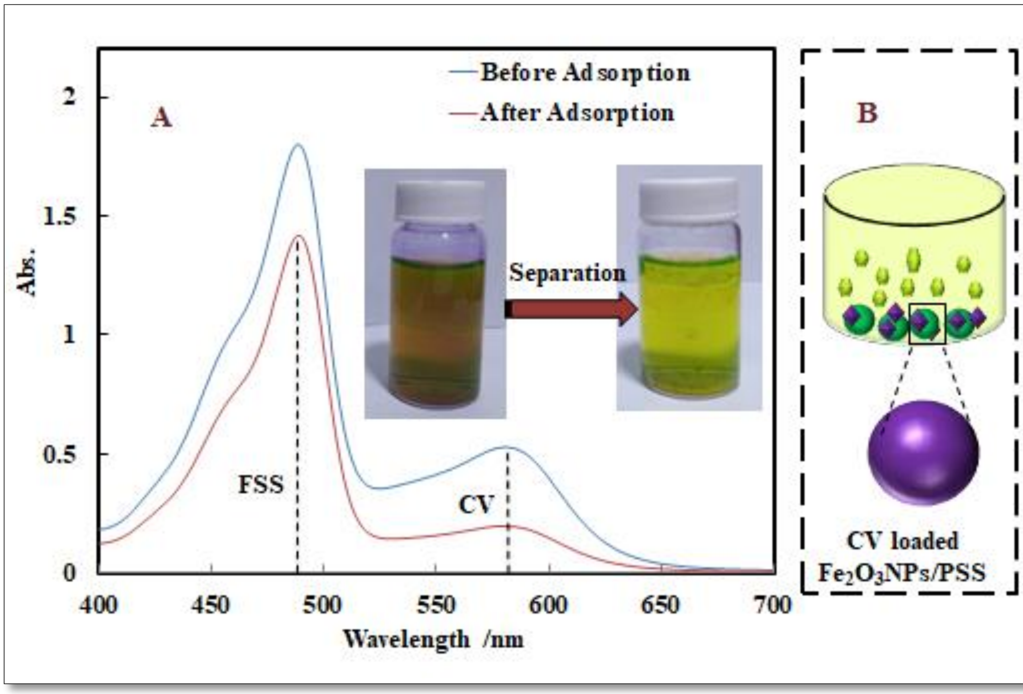

Figure 3.52 Schematic diagram showing the selective removal and adsorption of Fe_2O_3NPs/PSS with FSS/CV dye. UV–Vis spectra of FSS/CV mixture solutions before and after adsorption on the **A** Fe_2O_3NPs/PSS. Photos inside Fig **A** show the FSS/CV mixture solutions before adsorption and after adsorption. **B** CV dye loaded Fe_2O_3NPs/PSS.

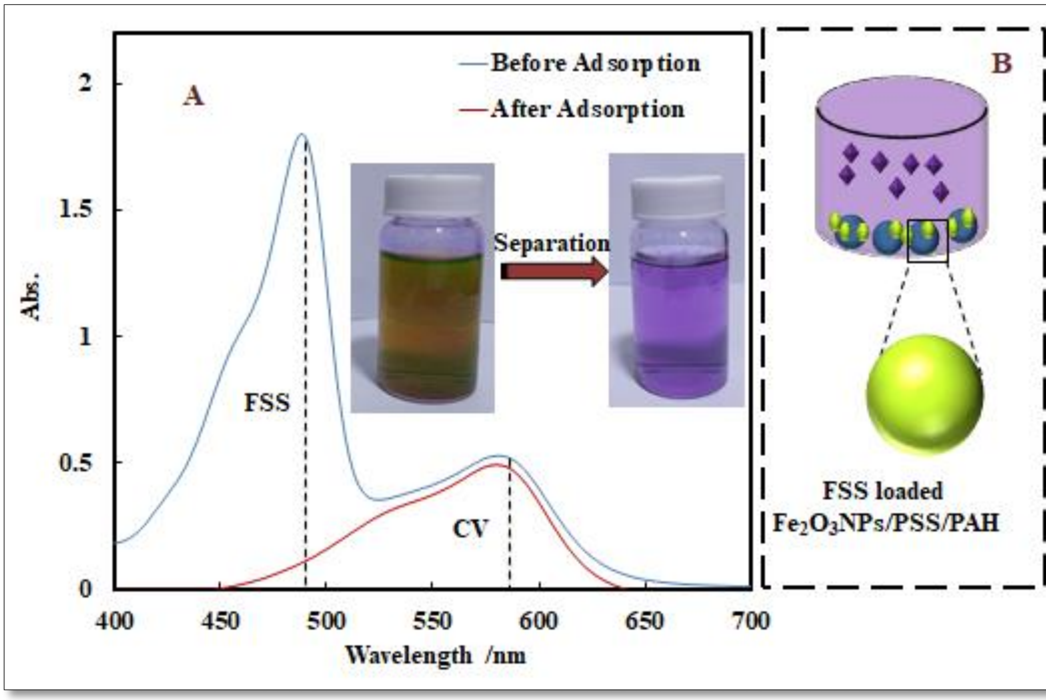

Figure 3.53 Schematic diagram showing the selective removal and adsorption of Fe_2O_3NPs/PSS/PAH with FSS/CV dye. UV–Vis spectra of FSS/CV mixture solutions before and after adsorption on the **A** bare Fe_2O_3NPs/PSS/PAH. Photos inside Fig **A** show the FSS/CV mixture solutions before adsorption and after adsorption. **B** FSS dye loaded Fe_2O_3NPs/PSS/PAH.

3.2.8 Regeneration and Reuse of used Bare and Surface Modified Fe_2O_3NPs

In practical applications, an adsorbent's ability to be reused sustainably is important. As a result, the reuse and regeneration of the utilized Fe_2O_3NPs, Fe_2O_3NPs/PSS and Fe_2O_3NPs/PSS/PAH were also assessed for 5 cycle's adsorption/desorption and the results are displayed in Figure 3.54. The desorption of FSS dye was achieved by putting the loaded FSS-nanoparticles for 3 hours in 0.01 N NaOH, followed by washing five times with deionized water as shown in Figure 3.55(**A-F)**. The electrostatic attraction between the Fe_2O_3NPs and Fe_2O_3NPs/PSS/PAH and the anionic FSS dye was decreased as expected as a result of deprotonating. Fe_2O_3NPs and Fe_2O_3NPs/PSS/PAH show a high removal efficiency after five cycles of adsorption-desorption. As the number of reuse cycles increased, the FSS dye removal effectiveness declined; nonetheless, both the unmodified and surface-modified Fe_2O_3NPs lost approximately 5% of their initial efficiency over the course of five cycles. Consequently, the decline in removal effectiveness may be brought on by the changing of the surface properties of the unmodified and surface-modified Fe_2O_3NPs throughout the adsorption-desorption processes [29]. These results demonstrate that both the uncoated and surface-coated Fe_2O_3NPs are highly recyclable, making them an economical material with promising water treatment applications.

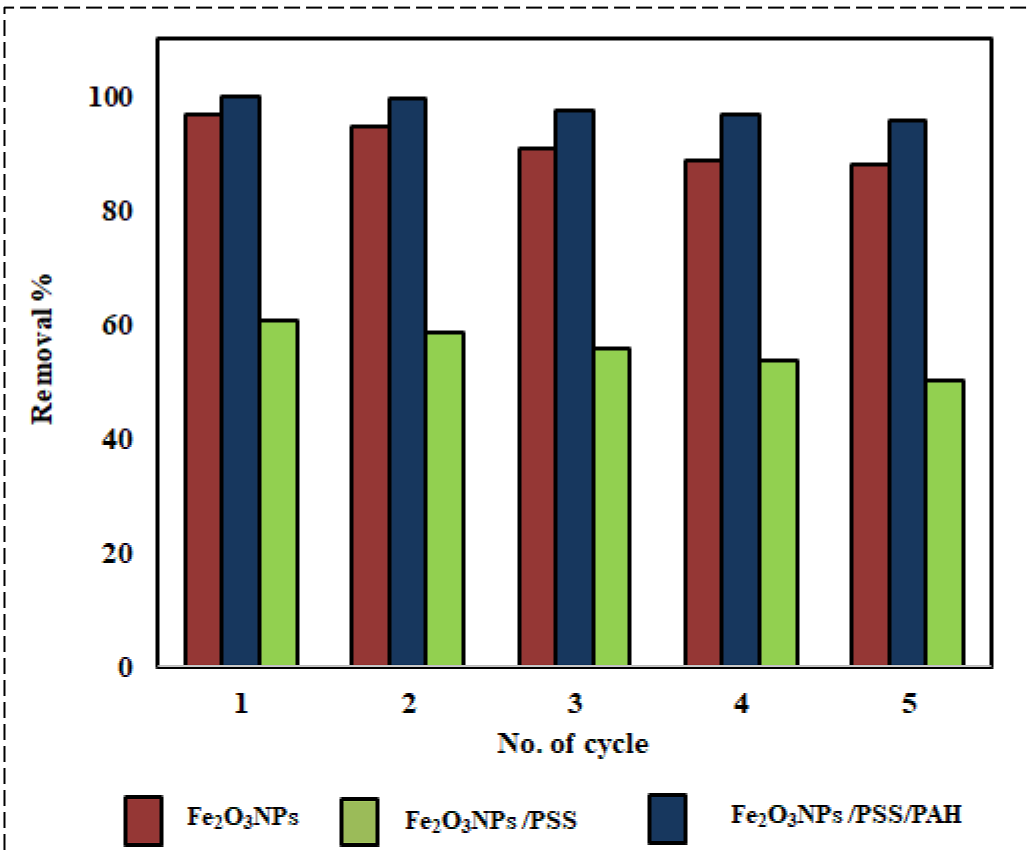

Figure 3.54 Reusability of bare and surface modified Fe_2O_3NPs for the removal of FSS dye.

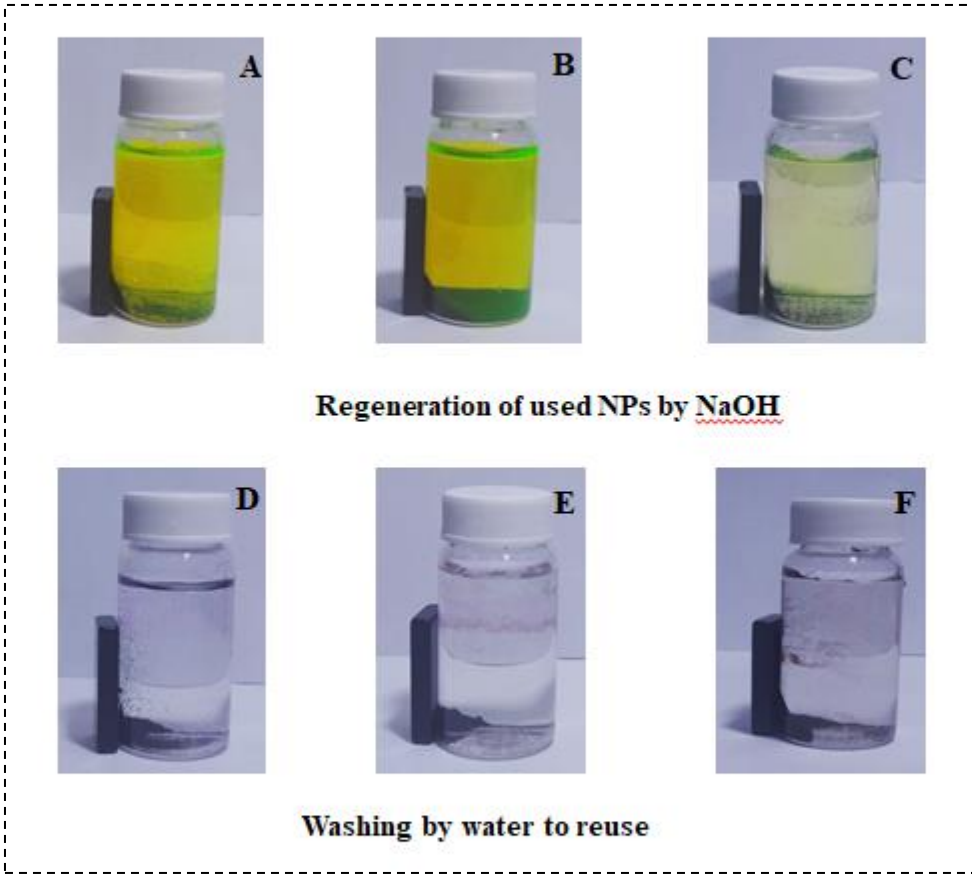

Figure 3.55 Regeneration of used **A** Fe_2O_3NPs **B** Fe_2O_3NPs/PSS/PAH and **C** Fe_2O_3NPs/PSS by NaOH. Washing of **D** Fe_2O_3NPs **E** Fe_2O_3NPs/PSS/PAH and **F** Fe_2O_3NPs/PSS by water to reuse.

3.3 Antimould Activity

3.3. Assessment of the Antimould Activity of Uncoated Fe_2O_3NPs and Surface Functionalized Fe_2O_3NPs towards *Trichoderma* fungus

In this study, a control sample of the fungus *Trichoderma* was grown for comparison with the tested formula that was created and defined in order to assess and determine the antimould action of the Fe_2O_3NPs antimould solutions Figure 3.56 and Figure 3.57. PDA was used as a culture medium in Petri dishes to grow the *Trichoderma* fungus. A 5 mm paper disc was immersed in the selected *Trichoderma* fungal suspension before being placed on the PDA-gel plate. The growth diameter of the *Trichoderma* fungus colony (mm) was measured as a function of time (days) to determine the *Trichoderma* fungus growth rate. The results show that the *Trichoderma* fungus in the control sample spreads more quickly than it does in Petri dishes treated with antimould formulations including 500 and 1000 mg L^{-1} Fe_2O_3NPs, as shown in Figure 3.56 and Figure 3.57. It was found that the *Trichoderma* samples treated with the 1000 mg L^{-1} Fe_2O_3NPs-based antimould preparations did not grow at all, and the sample diameter remained at 5 mm, whereas untreated *Trichoderma* samples grew until they approached 60 mm in diameter after day seven.

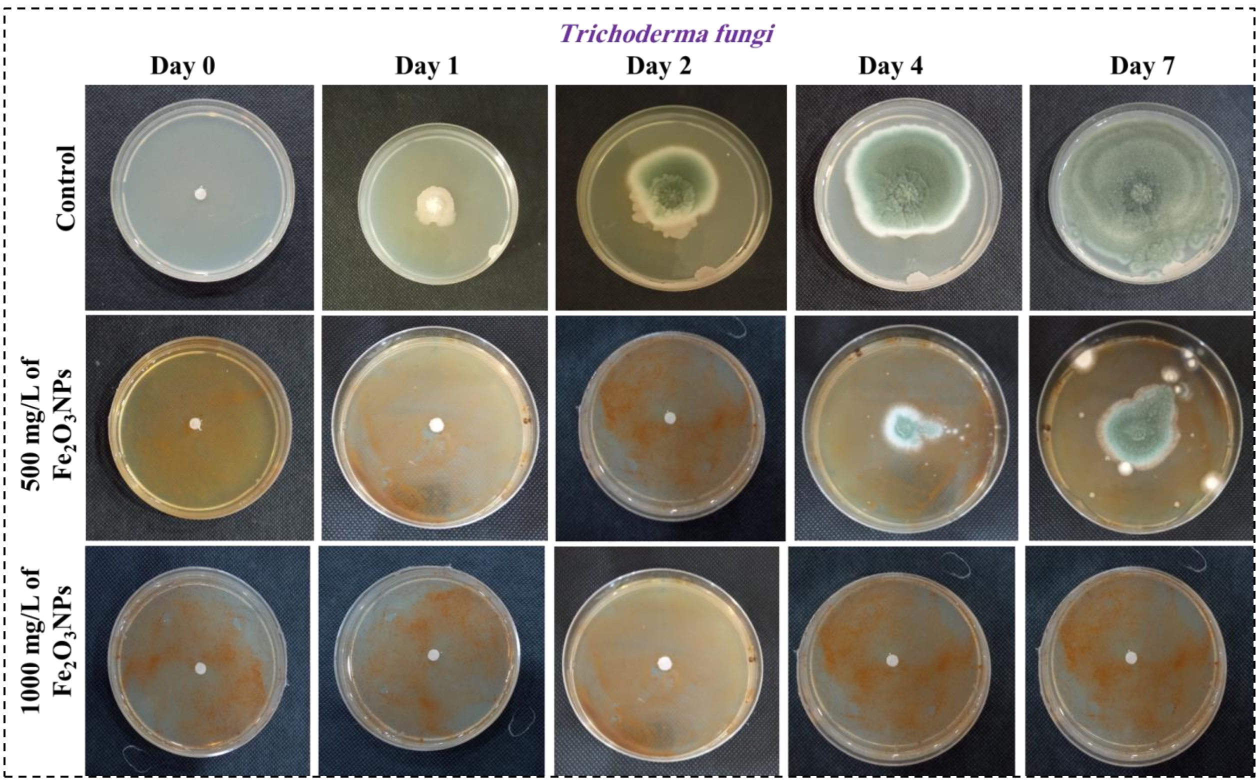

Figure 3.56 Digital photographs of the PDA–gel plates containing *Trichoderma* seeded in the center and with bare Fe_2O_3NPs as an antimould agent at testing concentration of 500 and 1000 mg L^{-1}, respectively, applied on the top of the PDA medium, and monitored over a period of seven days, in an incubator.

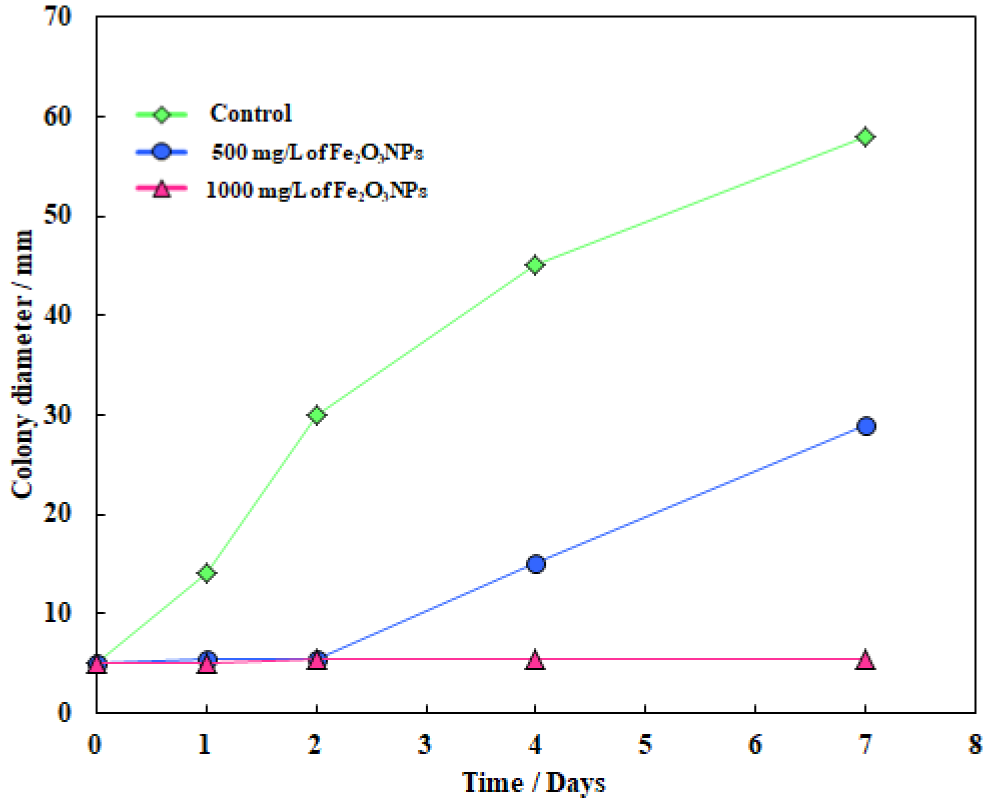

Figure 3.57 Growth diameter of a circular spot of *Trichoderma* seeded on paper disc is displayed as a function of time, comparing the antimould influence of the Fe_2O_3NPs. The solid lines are guides to the eye.

At concentrations of 500 and 1000 mg L^{-1}, it was discovered that bare Fe_2O_3NPs on their own significantly inhibited *Trichoderma* growth and exhibited antifungal activity against the fungus. After day four, the *Trichoderma* colony grew to a diameter of 28 mm after treatment with Fe_2O_3NPs at concentrations of 500 mg L^{-1}. When compared to the control, it was discovered that *Trichoderma* with 500 mg L^{-1} Fe_2O_3NPs grew significantly slower. The data in Figure 3.56 and Figure 3.57 at 500 mg L^{-1} Fe_2O_3NPs display that the growth spot vs. time did not alter meaningfully from days 0 to two. When *Trichoderma* was exposed to 1000 mg L^{-1} NPs, the bare Fe_2O_3NPs were proven to be an efficient antifungal agent. The data shows that the growth rate of *Trichoderma* decreased with the increase of the antifungal-agent concentration. This result can be attributed to the positive surface charge of the bare Fe_2O_3NPs, which are cationic particles at neutral pH see Figure 3.9 and Figure 3.10, and their powerful electrostatic attraction to the anionic surface of the *Trichoderma* hyphae.

The antifungal action of the Fe_2O_3NPs surface-functionalized with PSS and PAH was also evaluated against *Trichoderma* at 500 and 1000 mg L^{-1} concentration of the antifungal agent. Figure 3.58 and Figure 3.59 display the results of the antifungal examination of *Trichoderma* where the control samples of untreated *Trichoderma* were compared with the ones treated with Fe_2O_3NPs/PSS and Fe_2O_3NPs/PSS/PAH. Figure 3.58 and Figure 3.59 display that, without an antifungal agent, the *Trichoderma* has a growth diameter of 60 mm after seven days, while in the presence of the antifungal agent Fe_2O_3NPs/PSS; the *Trichoderma* growth was less than the control sample, with the growth diameter around 37 mm Figure 3.59. It is worth noting that Fe_2O_3NPs/PSS is an anionic nanoparticle Figure 3.11 and Figure 3.12; at neutral pH, it has a negative surface charge and lacks electrostatic attachment to the negatively charged *Trichoderma* walls. Nevertheless, after two days they display a similar antifungal impact to the bare Fe_2O_3NPs, which are cationic particles. However, after 4 days, *Trichoderma's* colony diameters started to grow. After day 7, the *Trichoderma* colony typically increased from a diameter of 5 mm to 37 mm after treatment with Fe_2O_3NPs/PSS. One probable description might be that, at these concentrations (500 and 1000 mg L^{-1}), the medium is so saturated with these nanoparticles that the growth of the hyphae in the bulk of the medium could potentially lead to a close contact of their *Trichoderma* walls with the trapped nanoparticles, thus having an adverse impact on the *Trichoderma*.

The outline of a secondary functionalization of these anionic nanoparticles by conjugation of the PSS layer with the PAH layer gives cationic nanoparticles (Fe_2O_3NPs/PSS/PAH) as shown in Figure 3.13 and Figure 3.14. The antifungal assay of the surface of the Fe_2O_3NPs functionalized with PSS and PAH was also conducted with *Trichoderma*. The data in Figure 3.60 and Figure 3.61 indicate that the

Fe_2O_3NPs/PSS/PAH have an extremely strong antifungal effect on *Trichoderma*. The growth rate of the *Trichoderma* treated with 500 and 1000 mg L^{-1} of Fe_2O_3NPs/PSS/PAH decreased after day seven.

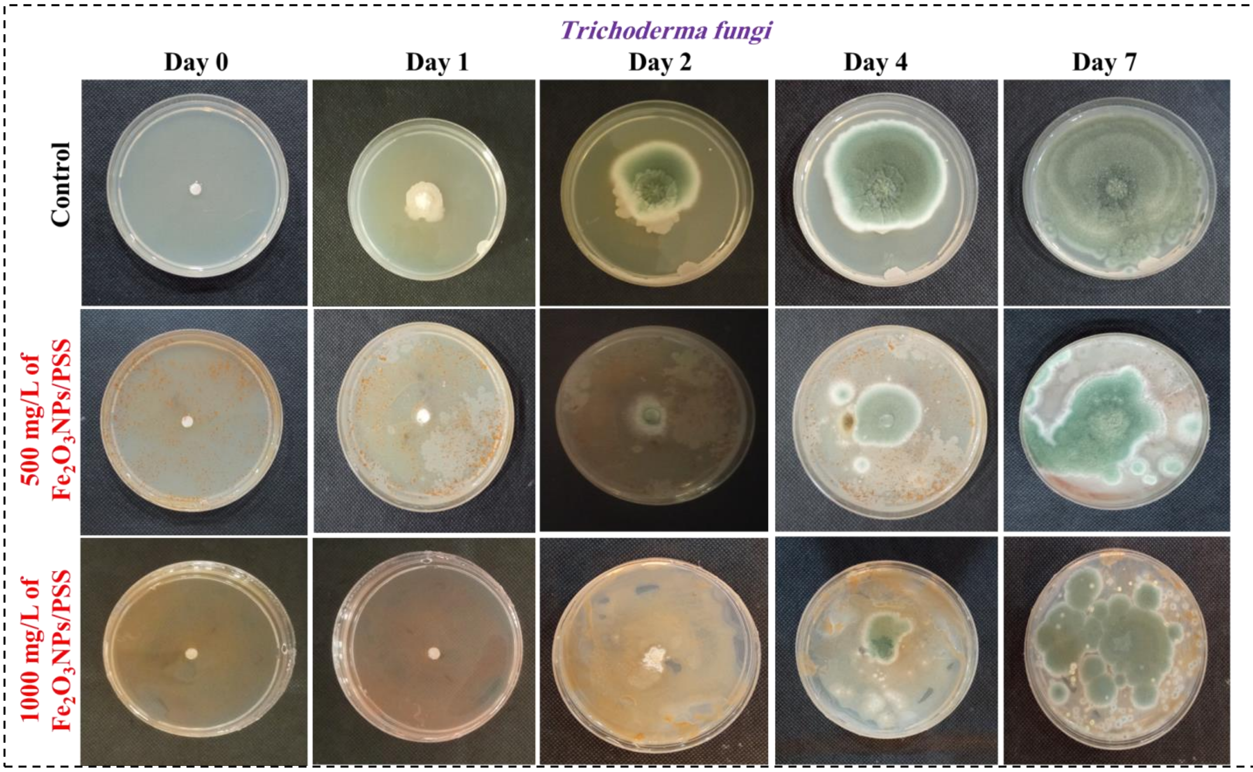

Figure 3.58 Digital images of Petri dishes that include *Trichoderma* growing for seven days with 500 and 1000 mg $L^{-1}$of Fe_2O_3NPs/PSS on top of the medium.

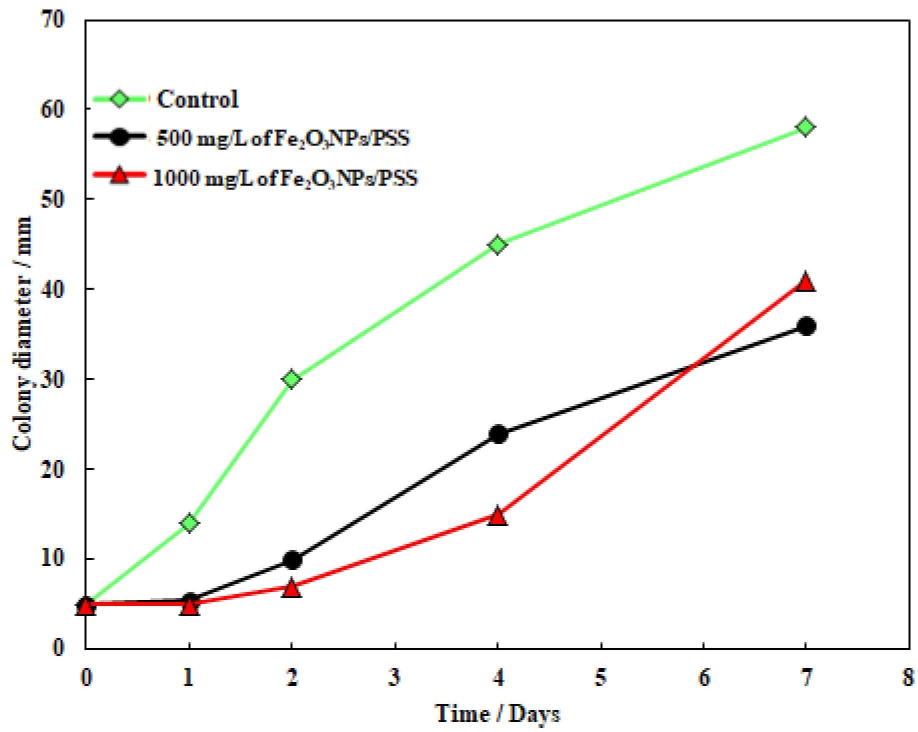

Figure 3.59 Growth diameter of a circular spot of *Trichoderma* seeded on paper disc is displayed as a function of time, comparing the antimould influence of the Fe_2O_3NPs/PSS. The solid lines are guides to the eye.

As it can clearly be seen, on day seven, the growth diameter was about 5 mm, compared with the control samples of a diameter of 60 mm. It was assume that PSS applied as an exterior layer on Fe_2O_3NPs greatly reduces their ability to adhere to the *Trichoderma*. The growth rate of the *Trichoderma* discovered that Fe_2O_3NPs/PSS were much less effective in killing the *Trichoderma* than the Fe_2O_3NPs/PSS/PAH or free Fe_2O_3NPs, which strongly attaché on the *Trichoderma* membrane due to electrostatic attraction [87]. It was observed that the PAH-coated Fe_2O_3NPs have even stronger antifungal action than the uncoated Fe_2O_3NPs on *Trichoderma*. Therefore, the antifungal action of the polyelectrolyte coated Fe_2O_3NPs appears to alternate with their surface charge.

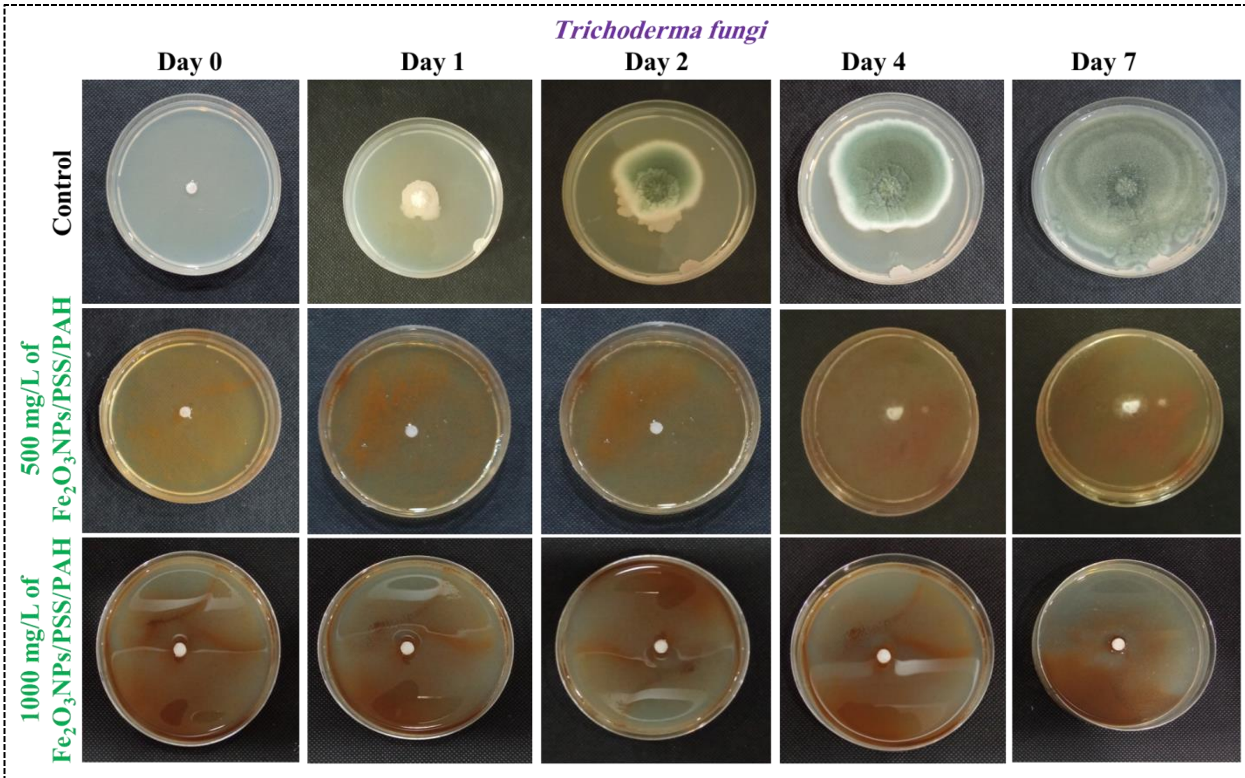

Figure 3.60 Digital images of Petri dishes that include *Trichoderma* growing for seven days with 500 and 1000 mg $L^{-1}$of Fe_2O_3NPs/PSS/PAH on top of the medium.

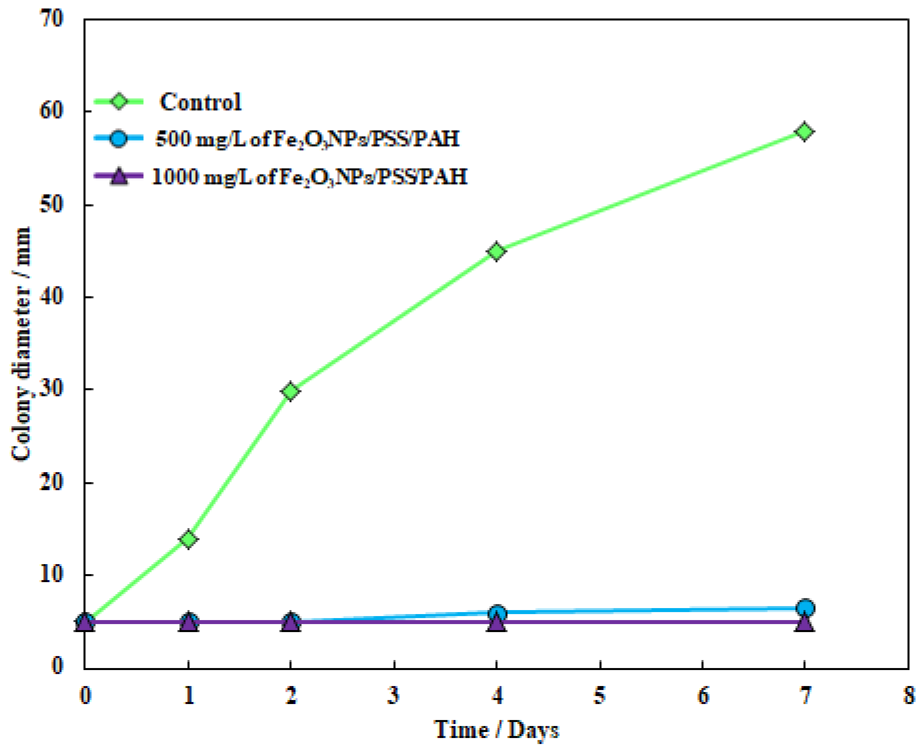

Figure 3.61 Growth diameter of a circular spot of *Trichoderma* seeded on paper disc is displayed as a function of time, comparing the antimould influence of the Fe_2O_3NPs/PSS/PAH. The solid lines are guides to the eye.

3.3.2 The Antifungal Activity of PSS and PAH towards *Trichoderma* fungus

The antifungal action of the free PSS and free PAH was also tested against *Trichoderma* at 1000 mg L^{-1} concentration of the polyelectrolyte. It was found that both free PSS and free PAH haven't antifungal activity against *Trichoderma* at a concentration of 1000 mg L^{-1} Figure 3.62 and Figure 3.63.

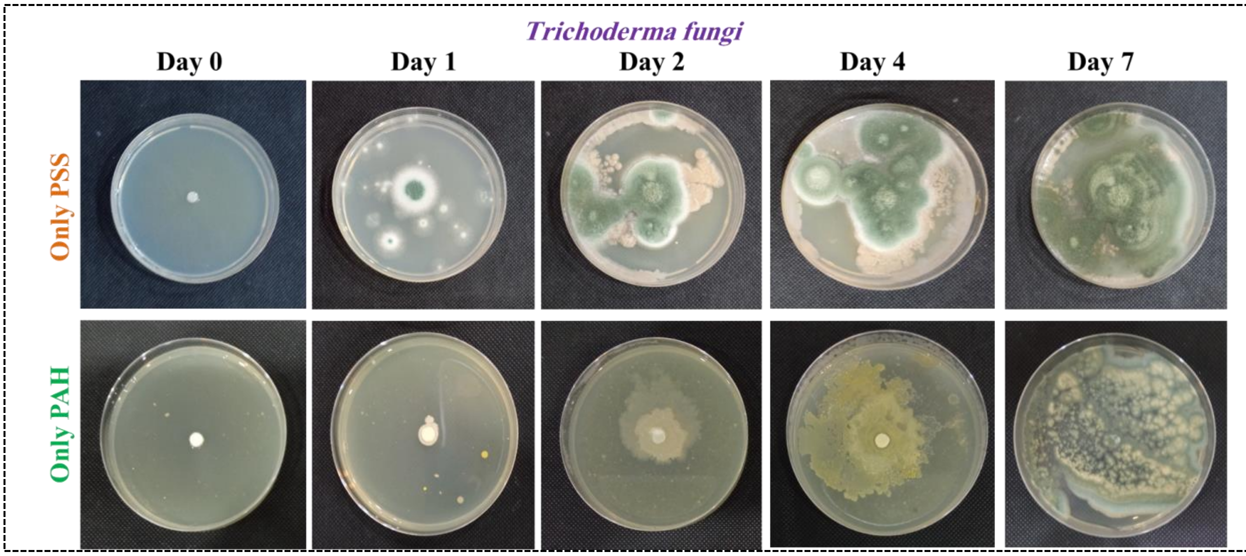

Figure 3.62 Digital images of Petri dishes that include *Trichoderma* growing for seven days with 1000 mg $L^{-1}$of PSS and PAH on top of the medium.

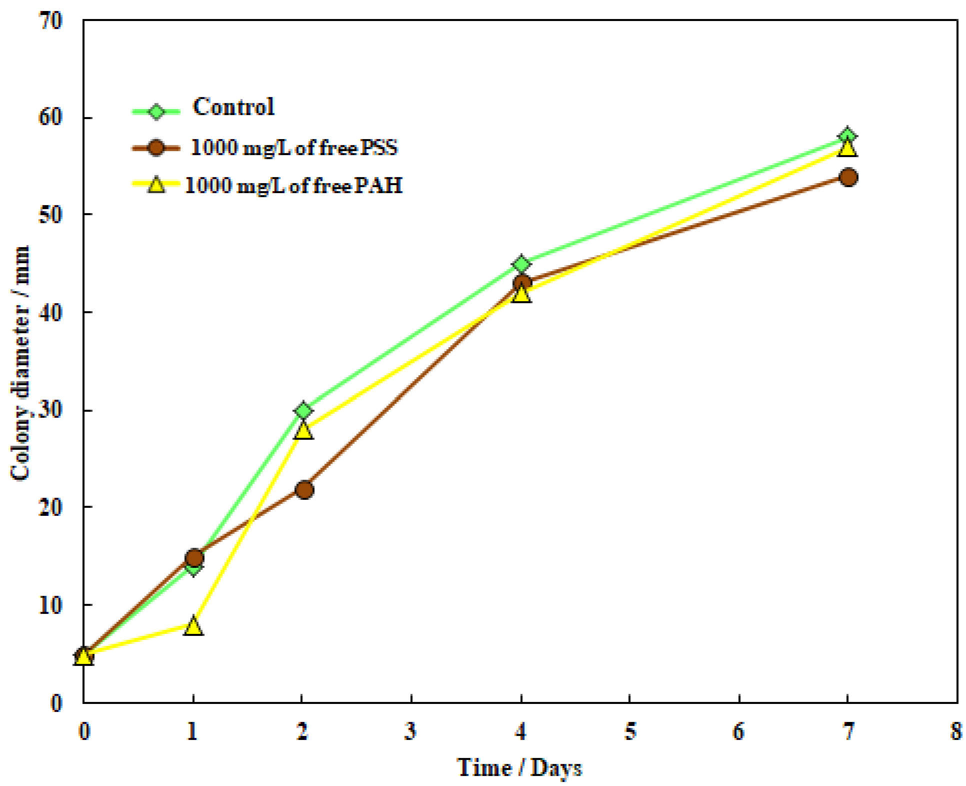

Figure 3.63 Growth diameter of a circular spot of *Trichoderma* seeded on paper disc is displayed as a function of time, comparing the antimould influence of the free polyelectrolyte. The solid lines are guides to the eye.

2.4 Conclusion.

1. In this study, the precipitation method was used to produce Fe_2O_3NPs at two calcination temperatures (200 and 500 °C). The data of the various techniques display that the increase of the calcination temperature leads to an increase of size of Fe_2O_3NPs.

2. The adsorption of FSS dye onto bare and surface modified Fe_2O_3NPs and its photocatalytic activity were then studied. The present work indicates that bare Fe_2O_3NPs had significant adsorption and photocatalytic activity against FSS dye and their impact increased upon increasing the Fe_2O_3NPs dose.

3. The results showed that the kinetic data worked well with the pseudo-second-order kinetic model. The Langmuir isotherm model was found to best fit the adsorption equilibrium results for FSS dye adsorption.

4. To evaluate the influence of the surface coating, a series of Fe_2O_3NPs coated with polyelectrolytes using the layer by-layer technique were synthesized and their adsorption and photocatalytic activity toward FSS dye was compared to that of the bare Fe_2O_3NPs.

5. It was discovered that the adsorption and photocatalytic activity of the surface-modified Fe_2O_3NPs alternates with the particle surface charge. The nanoparticles of anionic surface (Fe_2O_3NPs/PSS) had much lower adsorption and photocatalytic activity than the ones of cationic surfaces (Fe_2O_3NPs/PSS/PAH and bare Fe_2O_3NPs).

6. The results provide new insights about the influence of the Fe_2O_3NPs surface coatings with polyelectrolytes using the layer by-layer technique on their adsorption and photocatalytic action and could potentially lead to development of better adsorption and photocatalytic activity formulations.

7. It was also found that the anionic FSS dye has much higher adsorbed selectively on the Fe_2O_3NPs/PSS/PAH and free Fe_2O_3NPs adsorbent than the cationic ones.

8. The study also showed that bare and surface modified Fe_2O_3NPs presented high recyclability performance and thus they will be low-cost materials and have superior probability in the treatment of water.

9. The antifungal impacts of uncoated and surface-coated Fe_2O_3NPs were tested on *Trichoderma* fungus. It was revealed that, by surface coating PAH and PSS on Fe_2O_3NPs, one can yield formulations which are substantially more effective on *Trichoderma* fungus, compared to untreated sample (control sample) at the same conditions. The data presented that both uncoated and surface-coated Fe_2O_3NPs examined prevent the growth of *Trichoderma* fungus at 500 and 1000 mg L^{-1} particle concentrations.

Future work

Possible directions for future research are outline below. Those may include the following:

1. Synthesis of other nanoparticles such as CuONPs, ZnONPs and $Mg(OH)_2$NPs nanoparticles and characterise their properties. Also, examination of the adsorption and photocatalytic activity of these nanoparticles with dyes.

2. Synthesis and evaluation of the antibacterial, anti-algal and anti-yeast properties of surface modified iron oxide nanoparticles with PSS and PAH.

3. Study the action of bare and functionalized iron oxide nanoparticles towards human keratinocyte cell.

References

[1] S. Noreen , G. Mustafa , S. M. Ibrahim , S. Naz , M. Iqbal , M. Yaseen , T. Javed , and J. Nisar , “Iron oxide (Fe_2O_3) prepared via green route and adsorption efficiency evaluation for an anionic dye: Kinetics, isotherms and thermodynamics studies,” *J. Mater. Res. Technol.*, vol. 9, no. 3, pp. 4206–4217, 2020.

[2] A. Silambarasu, A. Manikandan, and K. Balakrishnan, “Room-temperature superparamagnetism and enhanced photocatalytic activity of magnetically reusable spinel $ZnFe_2O_4$ nanocatalysts,” *J. Supercond. Nov. Magn.*, vol. 30, no. 9, pp. 2631–2640, 2017.

[3] L. S. Al Banna, N. M. Salem, G. A. Jaleel, and A. M. Awwad, “Green synthesis of sulfur nanoparticles using Rosmarinus officinalis leaves extract and nematicidal activity against Meloidogyne javanica,” *Chem. Int.*, vol. 6, no. 3, pp. 137–143, 2020.

[4] A. F. Halbus, T. S. Horozov, and V. N. Paunov, “Colloid particle formulations for antimicrobial applications,” *Advances in Colloid and Interface Science*. vol. 249, no. 2017, pp. 134–148, 2017.

[5] A. F. Halbus, T. S. Horozov, and V. N. Paunov, “Controlling the antimicrobial action of surface modified magnesium hydroxide nanoparticles,” *Biomimetics*, vol. 4, no. 2, p. 41, 2019.

[6] F. F. Karam, F. H. Hussein, S. J. Baqir, A. F. Halbus, R. Dillert, and D. Bahnemann, “Photocatalytic degradation of anthracene in closed system reactor,” *Int. J. Photoenergy*, vol. 2014, no. 1, pp. 1–6, 2014.

[7] A. F. Halbus, T. S. Horozov, and V. N. Paunov, “Self-grafting copper oxide nanoparticles show a strong enhancement of their anti-algal and anti-yeast action,”

Nanoscale Adv., vol. 1, no. 6, pp. 2323–2336, 2019.

[8] J. R. Peller, S. P. Mezyk, and W. J. Cooper, "Bisphenol A reactions with hydroxyl radicals: diverse pathways determined between deionized water and tertiary treated wastewater solutions," *Res. Chem. Intermed.*, vol. 35, no. 1, pp. 21–34, 2009.

[9] M. Kamaraj, T. Kidane, K. U. Muluken, and J. Aravind, "Biofabrication of iron oxide nanoparticles as a potential photocatalyst for dye degradation with antimicrobial activity," *Int. J. Environ. Sci. Technol.*, vol. 16, no. 12, pp. 8305–8314, 2019,

[10] A. Alshehri, M. A. Malik, Z. Khan, S. A. Al-Thabaiti, and N. Hasan, "Biofabrication of Fe nanoparticles in aqueous extract of Hibiscus sabdariffa with enhanced photocatalytic activities," *RSC Adv.*, vol. 7, no. 40, pp. 25149–25159, 2017.

[11] X. Wang, S. Yuan, S. Chen, G. Chen, J. Zhang, and L. Zhang, "Synthesis of Ag_3PO_4–AgBr with a novel heterostructure, and its photocatalytic properties," *Res. Chem. Intermed.*, vol. 41, no. 8, pp. 5137–5147, 2015.

[12] T. S. Malarvizhi and T. Santhi, "Lignite fired fly ash modified by chemical treatment for adsorption of zinc from aqueous solution," *Res. Chem. Intermed.*, vol. 39, no. 6, pp. 2473–2494, 2013.

[13] T. Masciangioli and W. X. Zhang, "Environmental technologies at the nanoscale," *Environ. Sci. Technol.*, vol. 37, no. 5, 2003.

[14] J. K. Momin, C. Jayakumar, and J. B. Prajapati, "Potential of nanotechnology in functional foods," *Emirates J. Food Agric.*, vol. 25, no. 1, pp. 10–19, 2013.

[15] G. R. Vakili-Nezhaad and G. A. Mansoori, "An application of non-extensive statistical mechanics to nanosystems," *J. Comput. Theor. Nanosci.*, vol. 1, no. 2, pp.

227–229, 2004.

[16] N. I. Normi, A. S. Abdulhameed, A. H. Jawad, S. N. Surip, R. Razuan, and M. L. Ibrahim, "Hydrothermal-Assisted Grafting of Schiff base Chitosan by Salicylaldehyde for Adsorptive Removal of Acidic Dye: Statistical Modeling and Adsorption Mechanism," *J. Polym. Environ.*, pp. 1–13, 2022.

[17] S. P. Sahare and S. P. Zodape, "Removal of Cu (II) and Cd (II) Ions from Aqueous Solutions by Methionine Functionalized Cobalt-Magnesium Ferrite Chitosan Beads: Performance and Adsorption Mechanism," *J. Polym. Environ.*, pp. 1–19, 2022.

[18] S. M. Naserzade, M. Shahrousvand, J. Mohammadi-Rovshandeh, and H. Basati, "Preparation and Optimization of Photocatalytic Polyacrylic Acid/Guar Gum/TiO_2 Hydrogels for Absorption and Removing of Methylene Blue Under Visible and UV Irradiation," *J. Polym. Environ.*, pp. 1–18, 2022.

[19] H. Idrees, A. F. Halbus, Z. H. Athab, N. S. Saddam, S. H. Kahdum, and A. J. Atiyah, "Preparation and Investigation of some Physical Properties and Photocatalytic Activity of a co-Catalyst CoO-V_2O_5," in *Journal of Physics: Conference Series*, vol. 1999, no. 1, p. 1,2021.

[20] F. H. Hussein and A. F. Halbus, "Rapid Decolorization of cobalamin," *Int. J. PhotoenergyInternational J. Photoenergy*, vol. 2012, pp. 9, 2012.

[21] A. F. Halbus, Z. H. Athab, and F. H. Hussein, "Review on preparation and characterization of activated carbon from low cost waste materials," *Egypt. J. Chem* vol. 64, no. 12, pp. 7255–7268,., 2021.

[22]

S. Ajmal , I. Bibi , F. Majid , S. Ata , K. Kamran , K. Jilani , S. Nouren , Sh. Kamal

, A. Ali ,and M. Iqbal ., “Effect of Fe and Bi doping on $LaCoO_3$ structural, magnetic, electric and catalytic properties,” *J. Mater. Res. Technol.*, vol. 8, no. 5, pp. 4831–4842, 2019.

[23] H. N. Bhatti, J. Hayat, M. Iqbal, S. Noreen, and S. Nawaz, “Biocomposite application for the phosphate ions removal in aqueous medium,” *J. Mater. Res. Technol.*, vol. 7, no. 3, pp. 300–307, 2018.

[24]

A. Jamil , T.H. Bokhari , T. Javed , R. Mustafa , M. Sajid , S. Noreen , M. Zuber , A. Nazir , M. Iqbal ,and M. I. Jilani ., “Photocatalytic degradation of disperse dye Violet-26 using TiO_2 and ZnO nanomaterials and process variable optimization,” *J. Mater. Res. Technol.*, vol. 9, no. 1, pp. 1119–1128, 2020.

[25] A. M. Kamil, F. H. Abdalrazak, A. F. Halbus, and F. H. Hussein, “Adsorption of bismarck brown R dye onto multiwall carbon nanotubes,” *J Env. Anal Chem*, vol. 1, no. 104, p. 2, 2014.

[26] A. F. Halbus, A. J. Lafta, Z. H. ATHAB, and F. H. Hussein, “Adsorption of Reactive Yellow Dye 145 from Wastewater onto Iraqi Zahdy and Khestawy Date Palm Seeds Activated Carbons.,” *Asian J. Chem.*, vol. 26, pp. 167–172, 2014.

[27] M. Iqbal, M. Abbas, J. Nisar, A. Nazir, and A. Qamar, “Bioassays based on higher plants as excellent dosimeters for ecotoxicity monitoring: a review,” *Chem. Int.*, vol. 5, no. 1, pp. 1–80, 2019.

[28] A. F. Halbus, Z. H. Athab, and F. H. Hussein, “Adsorption of disperse blue dye on Iraqi date palm seeds activated carbon.,” *Int. J. Chem. Sci.*, vol. 11, no. 3, pp. 1219–1233, 2013.

[29] A. F. Halbus, Z. H. Athab, A. S. Abbas, A. K. Khaleel, S. M. Wahhoodee, and A. J.

Atiyah, “Adsorption, photodegradation, and selective removal of reactive red 2 dye onto cuprous oxide nanoparticles,” *Monatshefte für Chemie-Chemical Mon.*, vol. 153, no. 7, pp. 597–607, 2022.

[30] A. M. Alkherraz, A. K. Ali, and K. M. Elsherif, “Removal of Pb (II), Zn (II), Cu (II) and Cd (II) from aqueous solutions by adsorption onto olive branches activated carbon: equilibrium and thermodynamic studies,” *Chem. Int*, vol. 6, no. 1, pp. 11–20, 2020.

[31] S. Noreen, H. N. Bhatti, M. Iqbal, F. Hussain, and F. M. Sarim, “Chitosan, starch, polyaniline and polypyrrole biocomposite with sugarcane bagasse for the efficient removal of Acid Black dye,” *Int. J. Biol. Macromol.*, vol. 147, pp. 439–452, 2020.

[32] A. F. Halbus, J. M. Salman, A. J. Lafta, Z. H. Athab, F. M. Hasan, A. M. Kamil, and F. H. Hussein., “Equilibrium, isotherms and thermodynamic studies of congo red adsorption onto Ceratophyllum Demersum,” vol. 24, pp. 82–87, 2017.

[33] H. I. Ismael A. F. Halbus, Th. A.A.M. Alalwani, S. Baqir, Z. H. Athab, A. J. Atiyah, S. H. Kadhim, and E. T. Mohammad . “Fabrication of carbon nanotube (CNTs)/Co_3O_4-Ni_3O_4/Al_2O_3 nanocomposite catalyst and its application for photocatalytic removal of Celestine blue dye,” vol. 65, no. 6, pp. 99–110, 2019.

[34] L. M. Ahmed, A. F. Alkaim, A. F. Halbus, and F. H. Hussein, “Photocatalytic hydrogen production from aqueous methanol solution over metallized TiO_2,” *Int. J. ChemTech Res*, vol. 9, no. 10, pp. 90–98, 2016.

[35] M. A. Hassaan, A. El Nemr, and A. Hassaan, “Health and environmental impacts of dyes: mini review,” *Am. J. Environ. Sci. Eng.*, vol. 1, no. 3, pp. 64–67, 2017.

[36] F. H. Hussein, A. F. Halbus, F. H. Abdalrazak, and Z. H. Athab, “Adsorption o f cobalamin onto synthesized carbon nanotubes (CNT),” *J. Appl. e Chem.*, vol. 2, pp.

589–604, 2013.

[37] A. J. Lafta , A. F. HALBUS , Z. H. ATHAB , A. M. KAMIL , A. S. HUSSEIN , A. F. QHAT and F. H. HUSSEIN., “Effects of Activators on Adsorption Ability of Reactive Yellow-145 Dye on Activated Carbon from Iraqi Zahdi Date Palm Seeds.,” *Asian J. Chem.*, vol. 26, pp. 119–123, 2014.

[38] Z. H. Athab, A. F. Halbus, A. S. Abbas, J. M. Salman, and A. J. Atiyah, “Enhanced Macroporous Cationic Chitosan Hydrogel by Freezing and Thawing Method with Superadsorption Capacity for Anionic Dyes,” *J. Polym. Environ.*, pp. 1–17, 2022.

[39] F. H. Hussein, A. F. Halbus, H. A. K. Hassan, and W. A. K. Hussein, “Photocatalytic degradation of bismarck brown G using irradiated ZnO in aqueous solutions,” *E-Journal Chem.*, vol. 7, no. 2, pp. 540–544, 2010.

[40] F. H. Hussein, A. F. Halbus, A. J. Lafta, and Z. H. Athab, “Preparation and characterization of activated carbon from Iraqi Khestawy date palm,” *J. Chem.*, vol. 2015, pp. 1–11, 2015.

[41] K. Shameli *M. B. Ahmad, S. D. Jazayeri, S. Sedaghat, P.Shabanzadeh, H. Jahangirian, M. Mahdavi, and Y. Abdollahi.*, “Synthesis and characterization of polyethylene glycol mediated silver nanoparticles by the green method,” *Int. J. Mol. Sci.*, vol. 13, no. 6, pp. 6639–6650, 2012.

[42] P. Henry, A. F. Halbus, Z. H. Athab, and V. N. Paunov, “Enhanced antimould action of surface modified copper oxide nanoparticles with phenylboronic acid surface functionality,” *Biomimetics*, vol. 6, no. 1, pp. 1–16, 2021.

[43] A. F. Halbus and F. H. Hussein, “Photocatalytic Decolorization of Cobalamin in Aqueous Suspensions of TiO_2 and ZnO Under Solar Irradiation,” *Asian J. Chem.*, vol. 26, no. 12, p. 0, 2014.

[44] A. M. Kamil, F. H. Hussein, A. F. Halbus, and D. W. Bahnemann, "Preparation, characterization, and photocatalytic applications of MWCNTs/TiO_2 composite," *Int. J. Photoenergy*, vol. 2014, pp. 1–9, 2014.

[45] A. F. Halbus, T. S. Horozov, and V. N. Paunov, "Strongly enhanced antibacterial action of copper oxide nanoparticles with boronic acid surface functionality," *ACS Appl. Mater. Interfaces*, vol. 11, no. 13, pp. 12232–12243, 2019.

[46] Z. Izadiyan, M. Mohammed "Cytotoxicity assay of plant-mediated synthesized iron oxide nanoparticles using Juglans regia green husk extract," *Arab. J. Chem.*, vol. 13, no. 1, pp. 2011–2023, 2020.

[47] P. J. Weldick, A. Wang, A. F. Halbus, and V. N. Paunov, "Emerging nanotechnologies for targeting antimicrobial resistance," *Nanoscale*, vol. 14, no. 11, pp. 4018–4041, 2022.

[48] D. Grosso, G. J. de A.A. Soler-Ilia, E. L. Crepaldi, F. Cagnol, Ch. Sinturel, A. Bourgeois, A. Brunet-Bruneau, H. Amenitsch, P. A. Albouy, and C. Sanchez . "Highly Porous TiO_2 Anatase Optical Thin Films with Cubic Mesostructure Stabilized at 700 °C," *Chem. Mater.*, vol. 15, no. 24, pp. 4562–4570, 2003.

[49] W. Ahmed, A. Elhissi, and K. Subramani, "Introduction to nanotechnology," *Nanobiomaterials Clin. Dent.*, pp. 3–16, 2012.

[50] M. Farahmandjou and F. Soflaee, "Synthesis and characterization of α-Fe_2O_3 nanoparticles by simple co-precipitation method," *Phys. Chem. Res.*, vol. 3, no. 3, pp. 191–196, 2015.

[51] E. A. Campos, Denise V. B. S. Pinto, J. I. S. de Oliveira, E. da C. Mattos, R. de C. L. Dutra., "Synthesis , Characterization and Applications of Iron Oxide Nanoparticles – a Short Review," vol. 7, pp. 267–276, 2015.

[52] M. Zia, A. R. Phull, and J. S. Ali, “Synthesis, characterization, applications, and challenges of iron oxide nanoparticles,” pp. 49–67, 2016.

[53] A. Marinin, “Synthesis and characterization of superparamagnetic iron oxide nanoparticles coated with silica,” vol. 2012, pp. 50, 2012.

[54] M. Shanmugavadivu, S. Kuppusamy, and R. Ranjithkumar, “Synthesis of Pomegranate Peel Extract Mediated Silver Nanoparticles and its Antibacterial Activity,” pp. 1-8, 2014.

[55] D. R. Boverhof, Ch. M. Bramante , J. H. Butala , Sh. F. Clancy , M. Lafranconi , J. West , and St. C. Gordon ., “Comparative assessment of nanomaterial definitions and safety evaluation considerations,” *Regul. Toxicol. Pharmacol.*, vol. 73, no. 1, pp. 137–150, 2015.

[56] M. Ahmadi, H. Elmongy, T. Madrakian, and M. Abdel-Rehim, “Nanomaterials as sorbents for sample preparation in bioanalysis: A review,” *Anal. Chim. Acta*, vol. 958, pp. 1–21, 2017.

[57] M. Z. Sharif, W. H. Azmi, A. A. M. Redhwan, and N. M. M. Zawawi, “Preparation and stability of silicone dioxide dispersed in polyalkylene glycol based nanolubricants,” *MATEC Web Conf.*, vol. 90, 2016.

[58] J. K. Oh and J. M. Park, “Iron oxide-based superparamagnetic polymeric nanomaterials: design, preparation, and biomedical application,” *Prog. Polym. Sci.*, vol. 36, no. 1, pp. 168–189, 2011.

[59] S. Laurent, D. Forge, M. Port, Al. Roch, C. Robic, L. V. Elst, and R. N. Muller., “Magnetic iron oxide nanoparticles: synthesis, stabilization, vectorization, physicochemical characterizations, and biological applications,” *Chem. Rev.*, vol. 108, no. 6, pp. 2064–2110, 2008.

[60] A. Lu, E. emsp14L Salabas, and F. Schüth, "Magnetic nanoparticles: synthesis, protection, functionalization, and application," *Angew. Chemie Int. Ed.*, vol. 46, no. 8, pp. 1222–1244, 2007.

[61] Q. A. Pankhurst, J. Connolly, S. K. Jones, and Jjj. Dobson, "Applications of magnetic nanoparticles in biomedicine," *J. Phys. D. Appl. Phys.*, vol. 36, no. 13, p. R167, 2003.

[62] W. Wu, Q. He, and C. Jiang, "Magnetic iron oxide nanoparticles: Synthesis and surface functionalization strategies," *Nanoscale Res. Lett.*, vol. 3, no. 11, pp. 397–415, 2008.

[63] Y. Hu, S. Mignani, J.-P. Majoral, M. Shen, and X. Shi, "Construction of iron oxide nanoparticle-based hybrid platforms for tumor imaging and therapy," *Chem. Soc. Rev.*, vol. 47, no. 5, pp. 1874–1900, 2018.

[64] M. Jeon, M. V Halbert, Z. R. Stephen, and M. Zhang, "Iron oxide nanoparticles as T1 contrast agents for magnetic resonance imaging: fundamentals, challenges, applications, and prospectives," *Adv. Mater.*, vol. 33, no. 23, p. 1906539, 2021.

[65] J. Zhao, X. Li, and X. Wang, "Fabrication of hybrid nanostructures based on Fe_3O_4 nanoclusters as theranostic agents for magnetic resonance imaging and drug delivery," *Nanoscale Res. Lett.*, vol. 14, no. 1, pp. 1–12, 2019.

[66] S. Babay, T. Mhiri, and M. Toumi, "Synthesis, structural and spectroscopic characterizations of maghemite γ-Fe_2O_3 prepared by one-step coprecipitation route," *J. Mol. Struct.*, vol. 1085, pp. 286–293, 2015.

[67] M. Geppert, "Synthesis and Characterization of Iron Oxide Nanoparticles and Investigation of their Biocompatibility on Astrocyte Cultures," *Tesis*, pp. 12–175, 2012.

[68] R. Anderson, A. Biong, and D. A. Gómez-Gualdrón, “Adsorption Isotherm Predictions for Multiple Molecules in MOFs Using the Same Deep Learning Model,” *J. Chem. Theory Comput.*, vol. 16, no. 2, pp. 1271–1283, 2020.

[69] P. Xu, G. M. Zeng , D. L. Huang , Ch. L. Feng , Sh. Hu , M. H. Zhao , C. Lai , Z. Wei , Ch. Huang , G. X. Xie ,and Z. F. Liu ., “Use of iron oxide nanomaterials in wastewater treatment: A review,” *Sci. Total Environ.*, vol. 424, pp. 1–10, 2012.

[70] B. R. Cuenya, “Synthesis and catalytic properties of metal nanoparticles: Size, shape, support, composition, and oxidation state effects,” *Thin Solid Films*, vol. 518, no. 12, pp. 3127–3150, 2010.

[71] S. Wu, A. Sun , F. Zhai , J. Wang , W. Xu , Q. Zhang ,and A. A. Volinsky., “Fe_3O_4 magnetic nanoparticles synthesis from tailings by ultrasonic chemical co-precipitation,” *Mater. Lett.*, vol. 65, no. 12, pp. 1882–1884, 2011.

[72] K. B. Narayanan and N. Sakthivel, “Biological synthesis of metal nanoparticles by microbes,” *Adv. Colloid Interface Sci.*, vol. 156, no. 1–2, pp. 1–13, 2010.

[73] J. Estelrich, E. Escribano, J. Queralt, and M. A. Busquets, “Iron oxide nanoparticles for magnetically-guided and magnetically-responsive drug delivery,” *Int. J. Mol. Sci.*, vol. 16, no. 4, pp. 8070–8101, 2015.

[74] J. A. Lemire, J. J. Harrison, and R. J. Turner, “Antimicrobial activity of metals: Mechanisms, molecular targets and applications,” *Nat. Rev. Microbiol.*, vol. 11, no. 6, pp. 371–384, 2013.

[75] J. P. Fortin, C. Wilhelm, J. Servais, C. Ménager, J. C. Bacri, and F. Gazeau, “Size-sorted anionic iron oxide nanomagnets as colloidal mediators for magnetic hyperthermia,” *J. Am. Chem. Soc.*, vol. 129, no. 9, pp. 2628–2635, 2007.

[76] A. Y. L. Tang, C. K. Y. Lo, and C. wai Kan, "Textile dyes and human health: a systematic and citation network analysis review," *Color. Technol.*, vol. 134, no. 4, pp. 245–257, 2018.

[77] A. S. Teja, "Synthesis , properties , and applications of magnetic iron oxide nanoparticles," no. March, vol. 55, pp. 22–45, 2009.

[78] S. E. Der Biomedizin, "Superparamagnetic Iron Oxide Nanoparticles in Biomedicine : Applications and Developments in Diagnostics and Therapy," pp. 1149–1166, 2013.

[79] G. Schneider and G. Decher, "Functional core/shell nanoparticles via layer-by-layer assembly. Investigation of the experimental parameters for controlling particle aggregation and for enhancing dispersion stability," *Langmuir*, vol. 24, no. 5, pp. 1778–1789, 2008.

[80] B. Sun, Y. Zhang, K.-J. Gu, Q.-D. Shen, Y. Yang, and H. Song, "Layer-by-layer assembly of conjugated polyelectrolytes on magnetic nanoparticle surfaces," *Langmuir*, vol. 25, no. 10, pp. 5969–5973, 2009.

[81] A. P. R. Johnston, C. Cortez, A. S. Angelatos, and F. Caruso, "Layer-by-layer engineered capsules and their applications," *Curr. Opin. Colloid Interface Sci.*, vol. 11, no. 4, pp. 203–209, 2006.

[82] D. Rawtan and Y. K. Agrawal, "Emerging strategies and applications of layer-by-layer self-assembly," *Nanobiomedicine*, vol. 1, no. Godište 2014, pp. 1–8, 2014.

[83] H. Krass, G. Papastavrou, and D. G. Kurth, "Layer-by-layer self-assembly of a polyelectrolyte bearing metal ion coordination and electrostatic functionality," *Chem. Mater.*, vol. 15, no. 1, pp. 196–203, 2003.

[84] P. M. Visakh, "Polyelectrolyte: Thermodynamics and Rheology," *Polyelectrolytes*,

pp. 1–17, 2014.

[85] M. G. Carneiro-da-Cunha, M. A. Cerqueira, B. W. S. Souza, J. A. Teixeira, and A. A. Vicente, "Influence of concentration, ionic strength and pH on zeta potential and mean hydrodynamic diameter of edible polysaccharide solutions envisaged for multinanolayered films production," *Carbohydr. Polym.*, vol. 85, no. 3, pp. 522–528, 2011.

[86] E. Guzmán, J. A. Cavallo, R. Chulia-Jordan, C. Gomez, M. C. Strumia, F. Ortega, and R. G. Rubio., "pH-induced changes in the fabrication of multilayers of poly (acrylic acid) and chitosan: fabrication, properties, and tests as a drug storage and delivery system," *Langmuir*, vol. 27, no. 11, pp. 6836–6845, 2011.

[87] A. F. Halbus, T. S. Horozov, and V. N. Paunov, "Surface-Modi fi ed Zinc Oxide Nanoparticles for Antialgal and Antiyeast Applications," no. 2020, pp. 440–451, 2020.

[88] T. Mendoza-Dorantes, U. Pal, J. R. Vega-Acosta, and C. Marquez-Beltran, "Encapsulation and surface charge manipulation of organic and inorganic colloidal substrates by multilayered polyelectrolyte films," *Colloids Surfaces A Physicochem. Eng. Asp.*, vol. 434, pp. 253–259, 2013.

[89] C. Márquez-Beltrán, <u>L. Castañeda</u>, M. Enciso-Aguilar, G. Paredes-Quijada, H. Acuna-Campa, A. Maldonado-Arce, and Jean-Francois Argillier."Structure and mechanism formation of polyelectrolyte complex obtained from PSS/PAH system: effect of molar mixing ratio, base–acid conditions, and ionic strength," *Colloid Polym. Sci.*, vol. 291, no. 3, pp. 683–690, 2013.

[90] A. F. Palomec-Garfias, K. V. Jardim, M. H. Sousa, and C. Márquez-Beltrán, "Influence of polyelectrolyte chains on surface charge and magnetization of iron oxide nanostructures," *Colloids Surfaces A Physicochem. Eng. Asp.*, vol. 549, pp.

13–24, 2018.

[91] K. Ariga, J. P. Hill, and Q. Ji, “Layer-by-layer assembly as a versatile bottom-up nanofabrication technique for exploratory research and realistic application,” pp. 2319–2340, 2007.

[92] G. Decher, “Fuzzy nanoassemblies: Toward layered polymeric multicomposites,” *Science (80-.).*, vol. 277, no. 5330, pp. 1232–1237, 1997.

[93] L. G. Paterno and M. A. G. Soler, “Layer-by-Layer enabled nanomaterials for chemical sensing and energy conversion,” *Jom*, vol. 65, no. 6, pp. 709–719, 2013.

[94] M. A. G. Soler, L. G. Paterno, and P. C. Morais, “Layer-by-Layer Assembly of Magnetic Nanostructures,” *J. Nanofluids*, vol. 1, no. 2, pp. 101–119, 2013.

[95] M. A. G. Soler, “Layer-by-layer assembled iron oxide based polymeric nanocomposites,” *J. Magn. Magn. Mater.*, vol. 467, pp. 37–48, 2018.

[96] S. Nayak and L. Andrew Lyon, “Soft nanotechnology with soft nanoparticles,” *Angew. Chemie - Int. Ed.*, vol. 44, no. 47, pp. 7686–7708, 2005.

[97] Z. Yang, H. Peng, W. Wang, and T. Liu, “Crystallization behavior of poly(ε-caprolactone)/layered double hydroxide nanocomposites,” *J. Appl. Polym. Sci.*, vol. 116, no. 5, pp. 2658–2667, 2010.

[98] N. B. Wyatt and M. W. Liberatore, “The effect of counterion size and valency on the increase in viscosity in polyelectrolyte solutions,” *Soft Matter*, vol. 6, no. 14, pp. 3346–3352, 2010.

[99] E. Karadağ, Z. D. Kasim, S. Kundakcı, and Ö. B. Üzüm, “Acrylamide / Potassium 3-sulfopropyl Methacrylate / Sodium Alginate / Bentonite Hybrid Hydrogels : Synthesis , Characterization and Its Application in Lauths Violet Removal from

Aqueous Solutions," vol. 18, no. 1, pp. 9–21, 2017.

[100] G. Li, G. Zhang, R. Sun, and C. Wong, "Dually pH-responsive polyelectrolyte complex hydrogel composed of polyacrylic acid and poly (2- (dimthylamino) ethyl methacrylate)," *Polymer (Guildf).*, vol. 107, pp. 332–340, 2016.

[101] H. Zhang, K. Xu, H. Ai, D. Chen, L. Xv, and M. Chen, "Synthesis , Characterization and Solution Properties of Hydrophobically Modified Polyelectrolyte Poly (AA-co-TMSPMA)," pp. 1137–1148, 2008.

[102] H. Bai, H. Zhang, Y. He, J. Liu, B. Zhang, and J. Wang, "Enhanced proton conduction of chitosan membrane enabled by halloysite nanotubes bearing sulfonate polyelectrolyte brushes," *J. Memb. Sci.*, vol. 454, pp. 220–232, 2014.

[103] J. L. Freyer, S. D. Brucks, and L. M. Campos, "Fully Charged : Maximizing the Potential of Cationic Polyelectrolytes in Applications Ranging from Membranes to Gene Delivery through Rational Design," pp. 1–8, 2017.

[104] C. Demand, O. F. Papermaking, and P. Waters, "Dissolved and colloidal substances (dcs) and the charge demand of papermaking process waters and suspensions: a review," vol. 7, pp. 6109–6193, 2012.

[105] Y. Chen, Ju-Yun Chiang, Hung-Tao Chou, Chien-Yu Fu, Ying-Chieh Chen, Chi-Young Lee, Nyan-Hwa Tai and Hwan-You Chang., "Toxicity analysis of poly(sodium-4- styrenesulfonate) coated graphene on HMEC-1 cells under dynamic conditions mimicking blood flow†," pp. 51910–51918, 2017.

[106] J. M. C. Lourenço, P. A. Ribeiro, A. M. B. Do Rego, F. M. B. Fernandes, A. M. C. Moutinho, and M. Raposo, "Counterions in poly(allylamine hydrochloride) and poly(styrene sulfonate) layer-by-layer films," *Langmuir*, vol. 20, no. 19, pp. 8103–8109, 2004.

[107] M. Mahdavi, M. B Ahmad, M. J Haron, and F. Namvar, .“Textile dyes and human health: a systematic and citation network analysis review,” *Molecules*, vol. 18, no. 7, pp. 7533–7548, 2013.

[108] R. G. Saratale, G. D. Saratale, J. S. Chang, and S. P. Govindwar, “Bacterial decolorization and degradation of azo dyes: A review,” *J. Taiwan Inst. Chem. Eng.*, vol. 42, no. 1, pp. 138–157, 2011.

[109] K. J. Tahir and F. A. Tawil, “Study the optical properties of fluorescein sodium dye doped in polymer polyvinyl alcohol,” *J. Glob. Pharma Technol.*, vol. 10, no. 3, pp. 488–497, 2018.

[110] S. M. Shavakandi and S. Sharifi, “The determination of the conduction mechanism and optical band gap of fluorescein sodium salt Fahrettin Yakuphanoglua,_, Memet Sekercib , Ertan Evinc a Department of Physics, Faculty of Arts and Sciences, Firat University, 23119 Elazig, Turkey b Departmen,” *Opt. Quantum Electron.*, vol. 49, no. 1, 2017.

[111] F. A. Tawil. “Study of Linear and Nonlinear Optical Properties of Fluorescein Sodium Dye,” no. 2015, 2017.

[112] B. S. Girgis, “Porosity development in activated carbons obtained from date pits under chemical activation with phosphoric acid,” vol. 52, pp. 105–117, 2002, .

[113] Y. Guo and D. A. Rockstraw, “Physicochemical properties of carbons prepared from pecan shell by phosphoric acid activation,” *Bioresour. Technol.*, vol. 98, no. 8, pp. 1513–1521, 2007.

[114] D. Mustafi, H. Joela, and M. W. Makinen, “The effective position of the electronic point dipole of the nitroxyl group of spin labels determined by endor spectroscopy,” *J. Magn. Reson.*, vol. 91, no. 3, pp. 497–504, 1991.

[115] J. Hayashi, T. Horikawa, I. Takeda, K. Muroyama, and F. Nasir Ani, “Preparing activated carbon from various nutshells by chemical activation with K_2CO_3,” *Carbon N. Y.*, vol. 40, no. 13, pp. 2381–2386, 2002.

[116] B. Chattopadhyaya, G. Di. Cristo, C. Z Wu, and G. Knott., “GAD67-Mediated GABA Synthesis and Signaling Regulate Inhibitory Synaptic Innervation in the Visual Cortex,” *Neuron*, vol. 54, no. 6, pp. 889–903, 2007.

[117] M. Turmuzi, W. R. W. Daud, S. M. Tasirin, M. S. Takriff, and S. E. Iyuke, “Production of activated carbon from candlenut shell by CO_2 activation [11],” *Carbon N. Y.*, vol. 42, no. 2, pp. 453–455, 2004.

[118] M. Pera-Titus, V. García-Molina, M. A. Baños, J. Giménez, and S. Esplugas, “Degradation of chlorophenols by means of advanced oxidation processes: A general review,” *Appl. Catal. B Environ.*, vol. 47, no. 4, pp. 219–256, 2004.

[119] K. Rajeshwar, C. R. Chenthamarakshan, S. Goeringer, and M. Djukic, “Titania-based heterogeneous photocatalysis. Materials, mechanistic issues, and implications for environmental remediation,” *Pure Appl. Chem.*, vol. 73, no. 12, pp. 1849–1860, 2001.

[120] A. M. Kamil, F. H. Hussein, A. F. Halbus, and D. W. Bahnemann, “Applications of MWCNTs / TiO_2 Composite,” *Int. J. Photoenergy*, vol. 2014, pp. 1–8, 2014.

[121] B. Li, C. Lai, G. Zeng, D. Huang, L. Qin, M. Zhang, M. Cheng, X. Liu, H. Yi, Ch. Zhou, F Huang, Sh. Liu, and Y. Fu . “Black Phosphorus, a Rising Star 2D Nanomaterial in the Post-Graphene Era: Synthesis, Properties, Modifications, and Photocatalysis Applications,” *Small*, vol. 15, no. 8, pp. 1–30, 2019

[122] K. Omri and N. Alonizan, “Effects of ZnO/Mn Concentration on the Micro-structure and Optical Properties of ZnO/Mn–TiO2 Nano-composite for

Applications in Photo-Catalysis," *J. Inorg. Organomet. Polym. Mater.*, vol. 29, no. 1, pp. 203–212, 2019.

[123] D. W. Li and C. S. Yang, "Fungal contamination as a major contributor to sick building syndrome," *Adv. Appl. Microbiol.*, vol. 55, no. February 2004, pp. 31–112, 2004.

[124] J. Singh, "Toxic moulds and indoor air quality," *Indoor Built Environ.*, vol. 14, no. 3–4, pp. 229–234, 2005.

[125] A. Nevalainen, M. Täubel, and A. Hyvärinen, "Indoor fungi: Companions and contaminants," *Indoor Air*, vol. 25, no. 2, pp. 125–156, 2015.

[126] L. Raimond, A. F. Halbus, Z. H. Athab, and V. N. Paunov, "Antimould action of Ziram and IPBC loaded in functionalised nanogels against Aspergillus niger and Penicillium chrysogenum," *Mater. Adv.*, 2022.

[127] V. R. Mallemula, N. N. Sanghai, V. Himabindu, and A. K. Chakravarthy, "Synthesis and characterization of antibacterial 2-(pyridin-3-yl)-1H-benzo [d] imidazoles and 2-(pyridin-3-yl)-3H-imidazo [4, 5-b] pyridine derivatives," *Res. Chem. Intermed.*, vol. 41, no. 4, pp. 2125–2138, 2015.

[128] J. Al E. M. Morales , "Synthesis of hematite α-Fe_2O_3 nanopowders by the controlled precipitation method," *Phys. Chem. Res.*, vol. 3, no. 3, pp. 191–196, 2017.

[129] M. J. Al-awady, G. M. Greenway, and V. N. Paunov, "RSC Advances titania nanoparticles towards microalgae and yeast : role of the particle concentration , size and surface charge †," pp. 37044–37059, 2015.

[130] M. M. Simon, S. Greenaway, J. K. White, H. Fuchs, V. G-Durner, S. Wells, T. Sorg, K. Wong, E. Bedu, E. J. Cartwright, R. Dacquin, S. Djebali, J. Estabel, and J.

Graw., “A comparative phenotypic and genomic analysis of C57BL/6J and C57BL/6N mouse strains,” *Genome Biol.*, vol. 14, no. 7, pp. 1–22, 2013,.

[131] S. Mécanique, S. Physics, and M. J. Walock, “l ’ École Nationale Supérieure d ’ Arts et Métiers University of Alabama at Birmingham Nanocomposite coatings based on quaternary metal- nitrogen and nanocarbon systems,” 2012.

[132] S. Park, Y. C. Kang, J. Y. Park, E. A. Evans, R. D. Ramsier, and G. G. Chase., “Physical Characteristics of Titania Nanofibers Synthesized by Sol-Gel and Electrospinning Techniques,” vol. 6, pp. 50–56.

[133] W. Shang, M. Ujihara , W. Y. Chong , S. H. Voon , T. Imae , L. V. Kiew , H. B. Lee , K. Sh. Sim ,and L. Y. Chung ., “Colloids and Surfaces B : Biointerfaces Size-dependent effect of cystine / citric acid-capped confeito-like gold nanoparticles on cellular uptake and photothermal cancer therapy,” *Colloids Surfaces B Biointerfaces*, vol. 161, pp. 365–374, 2018.

[134] A. L. Pattrrson “The Scherrer Formula for X-Ray Particle Size Determination.” Rev. 56(10) 978–982, 1939.

[135] D. A. Panayotov and J. T. Yates, “Spectroscopic Detection of Hydrogen Atom Spillover from Au Nanoparticles Supported on TiO 2 : Use of Conduction Band Electrons,” pp. 2959–2964, 2007.

[136] K. Gérardin, L. V. Kiew and *J. Clean.* “AC SC,”. 2019.

[137] M. Scimeca, S. Bischetti, H. K. Lamsira, R. Bonfiglio, and E. Bonanno, “microanalysis : A powerful tool in biomedical research and diagnosis on m er EDX microanalysis apparatus al us e on er al,” vol. 62, 2018.

[138] T. J. A. Slater, A. Janssen, P. H. C. Camargo, M. G. Burke, N. J. Zaluzec, and S. J. Haigh, “Ultramicroscopy STEM-EDX tomography of bimetallic nanoparticles : A

methodological investigation," *Ultramicroscopy*, vol. 162, pp. 61–73, 2016.

[139] S. Bhattacharjee, "DLS and zeta potential - What they are and what they are not?," *J. Control. Release*, vol. 235, pp. 337–351, 2016.

[140] R. Xu, C. Wu, and H. Xu, "Particle size and zeta potential of carbon black in liquid media," *Carbon N. Y.*, vol. 45, no. 14, pp. 2806–2809, 2007.

[141] R. Marsalek, "Particle Size and Zeta Potential of ZnO," *APCBEE Procedia*, vol. 9, pp. 13–17, 2014.

[142] H. Liu, P. Li, B. Lu, Y. Wei, and Y. Sun, "Transformation of ferrihydrite in the presence or absence of trace Fe (II): the effect of preparation procedures of ferrihydrite," *J. Solid State Chem.*, vol. 182, no. 7, pp. 1767–1771, 2009.

[143] Z. Jing and S. Wu, "Synthesis and characterization of monodisperse hematite nanoparticles modified by surfactants via hydrothermal approach," *Mater. Lett.*, vol. 58, no. 27–28, pp. 3637–3640, 2004.

[144] E. Darezereshki, "One-step synthesis of hematite (α-Fe_2O_3) nano-particles by direct thermal-decomposition of maghemite," *Mater. Lett.*, vol. 65, no. 4, pp. 642–645, 2011.

[145] A. Lassoued, M. S. Lassoued, B. Dkhil, S. Ammar, and A. Gadri, "Retracted Article: Photocatalytic degradation of methylene blue dye by iron oxide (α-Fe_2O_3) nanoparticles under visible irradiation," *J. Mater. Sci. Mater. Electron.*, vol. 29, no. 10, pp. 8142–8152, 2018.

[146] E. Rápó and S. Tonk, "Factors affecting synthetic dye adsorption; desorption studies: a review of results from the last five years (2017–2021)," *Molecules*, vol. 26, no. 17, p. 5419, 2021.

[147] A. Yakar, A. Ünlü, T. Yeşilçayır, and İ. Bıyık, “Kinetics and thermodynamics of textile dye removal by adsorption onto iron oxide nanoparticles,” *Nanotechnol. Environ. Eng.*, vol. 5, no. 1, pp. 1–12, 2020.